Extracting Skull-Face Models from MRI datasets for use in Craniofacial Reconstruction

Miguel Salas Zúñiga

Department of Computer Science

University of Sheffield

A thesis submitted for the degree of

Doctor of Philosophy

March, 2010

Acknowledgments

This work is dedicated to:

All my family and especially to Esmeralda and my little Alan,
To my mother Margarita who taught me to be generous...
To my father Jorge who taught me to be strong...
To Roberto, Lucy, Carmen, Vale, Toñita, Ernie, Fer and Bony,
for all their support.

I want to express my especial thanks to:

My supervisor, Dr. Steve Maddock for his patience and support during all the stages of the PhD.

Dr. Martin Evison and Dr Iain Wilkinson for providing me with the MRI data for conducting this research,

Phillip and John Petty for all their help and support in the last stage of my PhD

The family Muela Meza, Phil Green and family,

The family Foulstone Ruby, Tim, Katie and Joshi for being my second family

Oscar and Monica for being there when I most needed

Joe and Pearl McNulty for their advise and friendship specially to Joe for his time and advise on some strong parts of my thesis

Joan Crookes and Bryan for all their support and friendship

Jorge and Arturo Arroyo, William and Jordi for being my third family

The member of the University of Sheffield Chess club, Mark, Jay and Mithun for all the good times we passed between Queens, Kings, Knights and Drinks.

To the present and past people in the graphics lab: Ahmed, Ahmad, Alan, Daniela, Manuel, Michael, Paul, Prya, Orn and Twin,

and to all the persons that are not in this list, but were there when needed...

THANKS

Abstract

This thesis addresses the problem of how to improve the computer-based methods for forensic craniofacial reconstruction. The aim of forensic craniofacial reconstruction techniques is to estimate the face of a person when only the skull remains are available for identification. From manual to computerised techniques, different solutions have been proposed for estimating the face from the skull in a reliable and consistent way. In both types of systems, an issue is that the results produced are not reproducible consistently and are difficult to evaluate. This issue arises mainly because the reconstruction methods are based on a limited type of anthropometric data about the skull and face relationship. In this thesis, a method to improve the craniofacial reconstruction process is developed by focusing on two aspects. First, a method is developed which uses MRI data to produce detailed data to analyse the skull and face relation. 3D skull and face models can be generated in a systematic way, offering the possibility to extend these sources as needed (i.e. it is possible to create data sources designed for specific populations). Second, a craniofacial reconstruction system is created that exploits the advantages of the detailed 3D skull and face models. As a result, the system can produce estimations of faces that can be assessed quantitatively, and produced in a systematic way.

Contents

List of Tables

List of Figures

Chapter 1

Introduction

In forensic facial reconstruction applications the analysis of the skull is the primary means of recognizing the identity of an individual when all other identification tests are not possible (e.g. DNA identification, dental records, x-rays, etc.) [36]. In traditional techniques, a cast of the skull is made and clay layers are added to reconstruct the soft tissue. This process is guided by a set of standard data tables recording tissue depth at particular landmark points on the face. The forensic artist places these landmarks on the cast of the skull using his knowledge of the skull-face relationship. Then, on the basis of his personal experience and expertise, he estimates the most appropriate facial shape. Computerized versions of the process are also possible and are used to add flexibility and speed to the process and in other cases are used to create face models algorithmically.

Craniofacial reconstruction methods work under the assumption that "skulls are as particular as the individual face they define" [109]. Anthropometric data provides the methods with information for estimating the facial shape given a skull structure and a set of attributes of the individual in question. Figure 1.1 shows a schematic example of anthropometric landmarks in which the relation between the skull and face is known. This relation has been studied and applied for several years as the base for creating craniofacial reconstructions. The forehead, the margins of the eyes, the cheekbones, the bridge of the nose and the area above the lips and the chin are defined directly from the shape of the skull contours. However, other parts of the face such as the shape of the eyes, the nose and the lips cannot be determined directly from the skull [36].

The human head structure has several properties that can provide the craniofacial reconstruction process with additional information to support the process. For instance, in situations when the skull is incomplete, the aspect of symmetry is important to establish the proportions of missing parts. If the skull is badly damaged or fragmented, and depending on the extent of bone loss or damage, a reconstruction is achieved by assuming a certain degree of symmetry in the skull. While very few skulls are truly symmetrical, as previously expressed, the asymmetry has to be extreme before it begins to affect the outward appearance of the face significantly, and therefore "any slight error in restoring the missing portions of a skull can normally be accommodated" [73, 69].

The main issues in current craniofacial methods are, in the case of traditional methods, that the process is time consuming, requires specialized knowledge and also artistic and sculptural skills to produce the reconstructed face. The results are not easily reproducible and cannot be assessed quantitatively. In the case of computerized approaches that mimic the manual approaches there are similar limitations. In other cases, when computational approaches are used for estimating the face algorithmically, there is a lack of anthropometric data to generate the facial models.

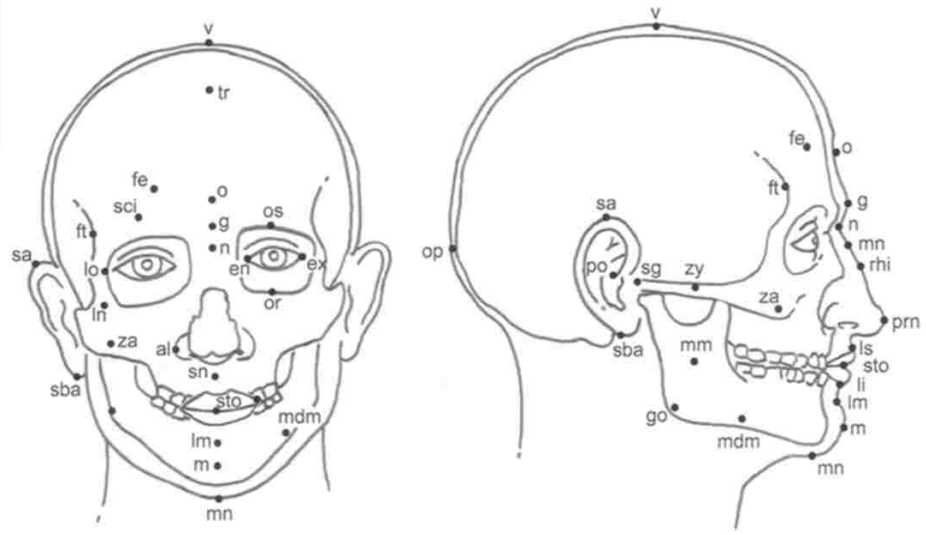

Figure 1.1: Relation between skull and face landmarks as used by forensic artists (reproduced with permission of C.Wilkinson [109]).

Both traditional and computerized approaches rely on the data provided by anthropometric tables. This data contains a limited number of landmark points, usually around 30 points. Secondly, the main sources of data have been gathered from measuring cadavers of a specific population (e.g. adult Caucasians). The limited data existing on the skull-face relationship is currently an issue for creating computerized craniofacial reconstruction systems that can produce objective, reproducible and consistent facial reconstructions that can be quantitatively assessed. The tissue depth data sets most commonly used have traditionally been compiled from measurements taken by inserting a needle into various points on cadavers. The initial measurements were mainly carried out on Caucasians [49] (as cited in [73]), Japanese [96] (as cited in [99]), Australians of European descent [34], and Malaysians [60]. These have increased the sources of information from which measurements can be applied. There is still a need to generate cohesive information about the relation between the skull and the facial soft tissues [29].

Much of the success of a craniofacial reconstruction system relies on the characteristics of the anthropometric sources available (size of the sample, number of landmark points, ethnic diversity of the individuals sampled, and method of acquisition). One indirect way to improve the performance of current methods can be achieved by improving the quality, size and diversity of the data available. This aspect is of special importance in computerized systems in which the process of craniofacial reconstruction is automated. In recent years, there has been a growth in data sets of facial tissue depths obtained using medical imaging and incorporating various population sets. Practitioners have begun investigating individual facial features using modern medical imaging techniques.

The aim of this thesis is to investigate a new approach to computerise facial reconstructions that relies on the skull-face relationship extracted from MRI datasets. This research work addresses two essential aspects present in craniofacial reconstruction methods. The first aspect is improving the current methods for the skull-face data generation process. This is achieved by developing a computational method to generate, in a safe manner, accurate and extensive data to analyze the skull and face geometry. The method was

developed to build 3D geometric models of the head in which the 3-dimensional structure of the skull and face can be studied. These models are extracted from a dataset of MRI volumes and used in a craniofacial reconstruction system to estimate the faces of unknown skulls. The second aspect addresses the main issues in creating 3D models of the face from the skull. Issues such objectivity, consistency, repeatability, and evaluation of the results can be solved by incorporating 3D skull-face models into the craniofacial reconstruction system.

1.1 Main contributions of this thesis

The main research contributions of this thesis are:

- A technique is presented that uses MRI data sets to produce anthropometric data of the head in a fast, safe, flexible and extensible way. In this context, the term safe refers to the acquisition technology used for generating data. With MRI technologies it is possible to scan live people in a safe way, without any side effect involved. This property makes it possible to create designed datasets containing samples of subjects from different races, sexes, ages and body complexions, which will allow the analysis of specific features that are of interest in a population. MRI technology is a faster acquisition method compared with manual measured data and less subject to errors. The term extensible refers to the fact that most of the current data sources about tissue depths of the head are restricted to a small number of points in the skull and face. MRI technology provides high contrast images from the different soft tissues of the head. By analysing the information contained in a MRI volume, it is possible to study the relation of the shapes of the skull and face in more regions of the head. With the detailed models of the skull and face produced, it will be possible to create statistical models, that are used for modelling the tissue depth distribution in the head.
  To produce the anthropometric data of the head, two segmentation methods for segmenting objects in images and volumetric data were created. First, a 2-dimensional method was developed which incorporates shape knowledge into a gradient vector flow active contour. This 2D formulation was published as a conference paper [82] (and also as a technical report [81]). Second, a 3-dimensional method using a 3D deformable model was produced in which the gradient vector flow formulation and the shape term were extended to 3D space. The results of the 3D formulation were published as a technical report [83]. These methods incorporate prior knowledge about the shape of the skull. Even though they could be used as general segmentation methods for image and volume data, they were designed to deal with the problem of skull segmentation in MRI data.

- A unique database of 3D skull-face models for studying and analysing the skull and face relation has been constructed. The University of Sheffield dataset of MRI volumes[1] was processed with the skull-face extraction process created in this work and, as a result, 60 detailed 3D models of the skull and face were generated for use in a craniofacial reconstruction system.

[1] The dataset was obtained thanks to the collaboration with Dr. Martin Evison from the Forensic Pathology Department and Dr. Iain Wilkinson from the Academic Unit of Radiology from the University of Sheffield.

- A craniofacial reconstruction system for generating 3D facial estimations is presented. The system has the capability to use different criteria in the reconstruction process, according to the features known of the individual to reconstruct. For example, the user can use models of the database with similar age and body build index to the subject of the unknown skull. Based on a deformable template approach, the system can produce facial models based on the anthropometric data contained in the database of head models described above. The system created has the capability of generating reproducible and consistent results that can be evaluated. These results have been presented at a workshop [84].

1.2 Structure of the dissertation

Chapter 2 presents an overview of the main techniques used for creating craniofacial reconstructions (CFR). It covers the data used and the main protocols for creating CFRs in traditional and computerized versions of the 3D method. It gives an overview of the area of 3D computerized craniofacial reconstructions and states the main problems found in the current approaches that need to be addressed.

Chapter 3 describes the main issues in creating a database of 3D head models based on MRI data. A description of the datasets used is presented and the method to extract face models from MRI data is described. An overview of the previous work in the area of skull extraction is presented and contrasted with the approach presented in this thesis.

Chapter 4 presents the underlying ideas of the method developed in the thesis to extract the skull from MRI data. A 2D technique to segment the skull based on contour extraction is presented. The chapter describes the Bayesian approach adopted to formulate the equations for incorporating prior knowledge of the skull in the segmentation process. The segmentation technique used is based on gradient vector flow active contours. The representation metrics and invariance of a shape descriptor for the skull are discussed, and the results of a set of experiments to test the ideas are presented.

Chapter 5 extends the ideas presented in chapter 4 into 3D space. A novel 3D extraction method to segment the skull in MRI data is presented. The main aspects to be adapted from the 2D Bayesian formulation introduced in chapter 4 are presented. A description of the models produced by this technique in the context of the creation of a database of skull-face models is included.

Chapter 6 describes a computer based craniofacial reconstruction system incorporating the 3D skull-face models generated from the techniques presented in chapter 5.

Chapter 7 presents a series of experiments that were designed to test the CFR system. The database of head models was used for evaluating different combinations of features in the reconstruction process.

Chapter 8 presents conclusions and discusses potential future work.

Chapter 2

Craniofacial Reconstructions

Forensic facial reconstruction[1] is employed as a strategy to identify an unknown individual when all other means of identifications cannot be applied (e.g. finger-prints, X-rays, odontology, DNA identification) [36]. In forensic settings, the aim of the process is to obtain a resemblance to the individual rather than to achieve an exact likeness of the deceased. By publishing images of the reconstruction, someone might recognise the resemblance and this will then generate the links that help to identify the individual in question.

Historically, different techniques have been employed in the process of facial reconstruction, from 2D drawings from the skull, to superimpositions of skull sketches on photographs of missing people [73]. In 3D methods, there are also different strategies to conduct a reconstruction. Some of them are based on employing sculptural techniques in which a 3D face estimation model is generated manually on a physical or digital model of the skull. There are other schemes using a set of images produced from a 3D model and their alignment to possible photographs or sketches in order to compare the correspondence between facial features [109]. The most relevant method to this thesis is the 3-dimensional computer modelling approach. However, in order to have a comprehensive understanding of facial reconstruction, a brief overview of other related approaches is presented.

This chapter presents an overview of two main branches in the area of craniofacial reconstructions based on 3D modelling: traditional manual techniques and computer assisted techniques. Section 2.1 presents the manual method to conduct craniofacial reconstructions and the main limitations of the approach. In section 2.2 the computerised method for craniofacial reconstruction is presented. Section 2.3 discusses the main issues to address in craniofacial reconstruction techniques.

2.1 Manual Craniofacial Reconstruction

Currently, facial reconstruction techniques are used in areas such as forensic medicine and archaeology. The technique is traditionally carried out by modelling the face using clay on a hand-made cast of the skull. The cast, which is made to avoid damage to the original skull, is used as the underlying structure from which the facial anatomy is built up to create a face. Appendix A shows a brief description of the anatomy of the head. In most cases, a forensic artist adds clay to the model guided by standard tables of data recording tissue depth at particular landmark points on the face. The artist places these landmarks

[1] In the rest of the document, we will be using the term craniofacial reconstruction and facial reconstruction interchangeably.

on the skull model using her knowledge of the skull-face landmark relation (see figure 1.1). Then, on the basis of personal expertise, she estimates the most appropriate facial shape (figure 2.1). An example of a tissue depth table is shown in table 2.1.

Philips and Smuts (1996)
CT scans
Mixed Race South Africans

	Male (16)		Female (16)	
Facial points	Mean	SD	Mean	SD
Forehead	5.36	1.44	4.88	1.02
Glabella	5.47	0.68	5.64	1.42
Nasion	4.00	2.42	4.68	2.35
Midnasal Rhinion	2.88	1.08	2.78	0.91
Subnasale Midphiltrum	12.25	2.97	10.13	2.48
Upper lip	13.16	2.51	13.63	3.70
Lower lip	10.43	1.69	12.45	2.31
Labiomental	12.02	2.07	11.70	1.66
Mental	8.94	2.42	9.57	2.36
Menton	6.61	1.71	6.47	1.57
Lateral forehead	4.51	1.40	4.78	1.74
Supraorbital	5.46	1.31	5.79	1.89

Table 2.1: An example of an anthropometric table as used by forensic experts to estimate the tissue thickness at specific landmark positions [109]. The measurements are given in mm.

The facial reconstruction results are highly dependent on the data used to model the skull-face relation. The limited information available is an issue in the process that is usually compensated by human expertise. At the present time, there is an interest in creating more objective and reproducible techniques to reduce the subjectivism introduced by the human factor [109, 36].

There are three basic schools of thought within clay reconstruction [105, 73]:

- The Russian method, developed by Gerasimov. This attempts to construct the facial anatomy on the surface of the skull by incorporating muscular structures to impose restrictions on the facial shape. This is a morphological approach.

- The American method. This employs the thickness average of soft tissue at some specific points located on prominent parts of the skull. This is a morphometric method because is purely based on distances (i.e. tissue depths).

- The Manchester method. This is a combination of the Russian and the American methods. It uses the soft-tissue thickness and considers the subtle details of the structure of the face anatomy to create the reconstruction

Even though this a commonly accepted classification, some authors argue that facial approximation methods are found to vary along a "combination" technique continuum, with all methods relying on soft-tissue depth information and anatomical knowledge to some degree [91]. For more details about the craniofacial reconstruction methods and

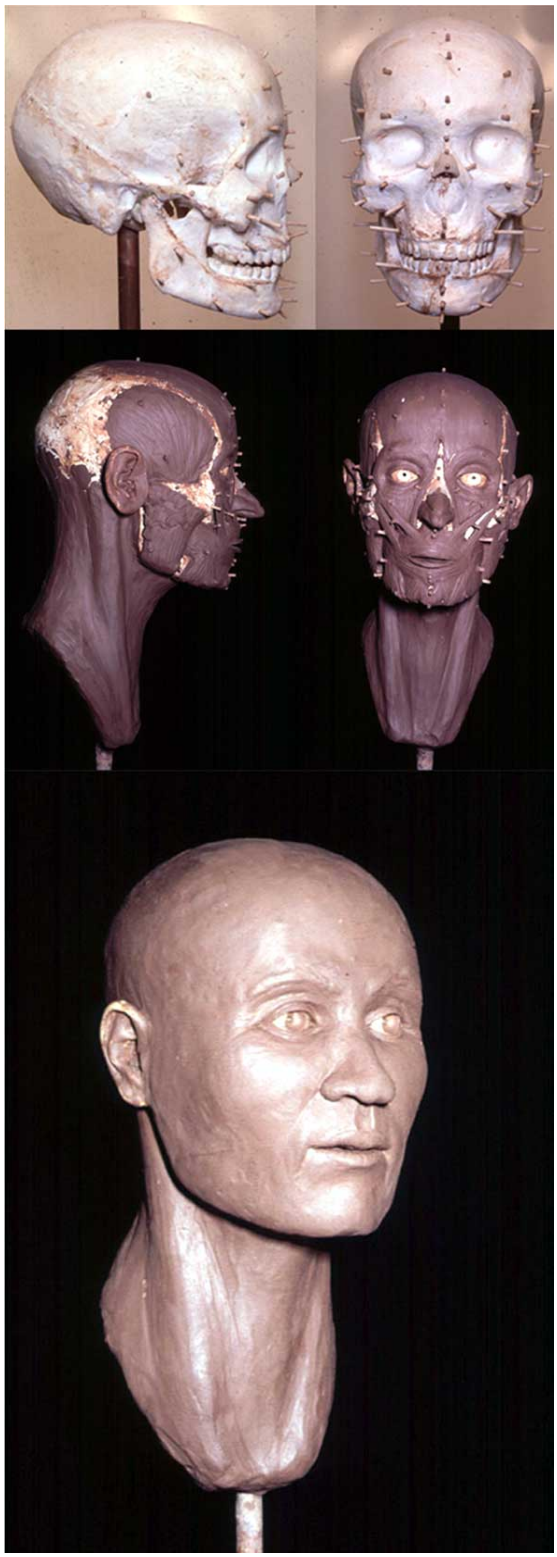

Figure 2.1: Traditional Facial Reconstruction Technique (reproduced with permission of C.Wilkinson [65]).

their evolution the reader can review the works of Wilkinson [109], Verze [105] and Evison [99].

Traditional clay facial reconstructions have two main limitations: they are time-consuming and they are not easily reproducible. The process of building an appropriate cast of the skull and the process of marking tissue depths and building of the muscles and skin surface can take several days to accomplish, depending on the final level of detail required [29]. Also the methods and results often vary from practitioner to practitioner. The speed and repeatability of traditional clay techniques could be improved using computerised techniques. The current dependence on sculpting skills and the subjectivity of the artist to compensate limited data sources can be reduced. Another limitation is the evaluation of the reconstructions, with no formal method to assess the quality of the reconstructions. These limitations are the principal motivations in researching methods for extending these traditional approaches to incorporate computerised techniques.

2.2 Computerised Craniofacial Reconstruction

There are several classifications of facial reconstruction methods using computational techniques. A first general classification based on how the computer is used in the craniofacial reconstruction task defines two types of systems:

- Computer assisted facial reconstructions. These are techniques that use the computer mainly to provide a more flexible, alternative medium to mimic the manual reconstruction process.
- Computer based facial reconstructions. These are techniques that use computer algorithms to produce new methods for creating facial reconstructions.

Both approaches offer advantages over manual methods. A computer assisted method provides flexibility to incorporate modifications in the final model, and reduces the dependence on artistic talent and 3D sculptural skills [28]. An example of this approach is presented in Davy et. al. [30, 29] where the use of computer tools to create more reliable, faster and accurate reconstructions is discussed. An inter-observer study was designed to investigate the repeatability of the method, in which three reconstructions were performed on the same skull at set time intervals. The tests suggest that the method is at some degree repeatable. Multiple reconstructions of the face were very similar to one another, especially in the areas of the face for which definitive scientific reconstruction guidelines exist. Despite the advantages of Davy's method, it does not resolve many of the issues that are problematic for craniofacial reconstruction area such as the interpretation of the landmarks and the subjective factor used to model the complexity anatomy of the human head.

Apart from the current limitations of computer technology, the databases for tissue depth information and facial features are still under research [93, 94, 102, 109]. Deeper investigations of the bone and soft tissue relationships are needed [29]. An in-vivo study using MRI could potentially help to improve the data available for landmark tissue depths and facial features, or even introduce novel ways of determining soft tissue prediction from bone.

The goal of computer based facial reconstruction methods is to reduce the subjectivity introduced by human factors by using statistical information to predict the facial shape. The main advantage of these techniques is their potential to provide more objective and

replicable results that can be evaluated quantitatively. However, the principal drawback of these methods is the lack of adequate and ethnically diverse sources of information to model the skin-face relationship. This data is essential for creating computer algorithms to automate the process. Moreover, given the importance of this element to the success of computer-based systems, the study and creation of large amounts of data to create such sources of information is currently a research topic [29].

In a similar way to the classification of traditional craniofacial reconstruction systems presented in section 2.1, Subsol proposes a similar classification for the computerised craniofacial techniques [95]:

- Morphometric methods. For these methods the face model produced depends only on the tissue depth information at certain points on the skull and face.
- Morphology methods. Additional knowledge of the underlying anatomical components of the face, such as muscles and the fat, is modelled in order to define the shape of the facial surface.
- Registration-based methods. Digital head models (usually created from CT and MRIs) provide a way of modelling the skull-face relationship used for the reconstruction process.

An overview of the most relevant work in the area of computer based craniofacial reconstruction systems will be presented in the following sections.

2.2.1 The Morphometrics Approach

In this approach the user chooses some sites on the skull surface where he defines the thickness of the facial tissue. A facial surface is then adjusted to interpolate these tissue landmarks. There are several alternatives to conduct this interpolation such as the use of specific types of surfaces, which satisfy geometric restrictions on the continuity and the smoothness of the resulting surface. Another alternative is the use of pre-defined face templates where the shape of the surface at the intra-landmark level is predefined. The problem is reduced to finding a deformation for matching points in the predefined facial template corresponding to the points defined with the landmarks located on the skull to be reconstructed.

Archer fits a generic hierarchical B-Spline surface model to the face landmarks [6]. The surface is automatically placed in order to smoothly and evenly interpolate the landmark points. Figure 2.2 shows the stages of this approach. Multiple facial base shapes can be generated by the B-spline using traditional tissue depths from anthropometric tables, with the appropriate tissue depths for different race, age, sex and body fat content. In the work of Andersson and Valfridsson [5], the vertices of an arbitrary reference mesh are projected onto the Computer Tomography (CT) volumetric data of the unknown skull. Landmark points are interpolated and the rest of the surface is adjusted using information from neighbouring landmarks.

Such morphometric methods require a lot of manual assistance in setting up the interpolation function, and even though some heuristics have been suggested to deal with the lack of anthropometric information in some regions of the face (such as the use of landmark neighbour information and explicit geometric restrictions), it is evident that the sparseness of anthropometric data is a strong limitation for determining the correct facial shape. A possible solution to the sparse data problem is to use a facial template

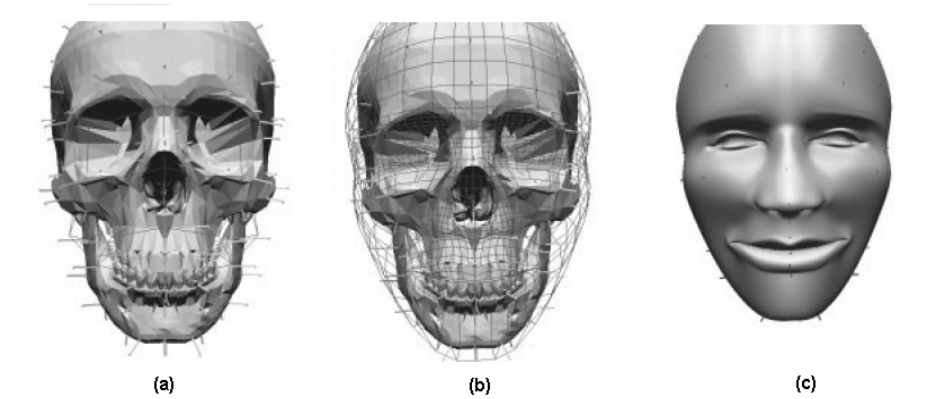

Figure 2.2: (a) A polygonal model of the skull is created and landmarks are placed at some specific places. (b) A polygonal mesh is fitted to interpolate the points indicated by the landmarks. (c) The final smooth surface (taken from [6]).

surface model created from real data. In this way, by having a complete surface with the inter-landmark relation solved, the problem is reduced to finding a deformation for the template matching the points marked on the unknown skull defining the facial thicknesses. Vanezis et. al. [104, 103] proposes a deformation technique used to adjust a facial template chosen from a database of scanned faces and deformed to match the position of a set of landmarks placed on the unknown skull surface. They use a database of 5000 faces collected by using a laser scanning system. Figure 2.3 illustrates this process. Nelson and Michael [68] introduce a volumetric deformation technique. Feature points are first placed at known anatomical points around the given skull through the use of a volume-based correspondence algorithm. These points are used to select a reference head from a set of candidate models using the reference model with closest matching skull for deformation. Nelson and Michael state that the problem of tissue depth collection is a key limitation for producing reliable results in craniofacial reconstruction systems.

Petrick et. al. presents a hierarchical volume deformation technique to determine the final surface approximation [71]. The data for creating a reference model is taken from a CT volume. This data provides an initial volumetric reference model with a skull and its face. Landmark points are placed on the reference model and then used to produce new reconstructions by matching the points of the reference skull with the landmarks of the unknown skull. The reconstruction is generated by selecting a reference model with similar attributes such as sex, age, body-build.

The main problem with these approaches is the difficulty in determining a class of transformations to precisely and consistently deform the reference face models using only the sparse anthropometric data [95]. These transformations must possess a compromise between flexibility and complexity to model the high variability present in the human face.

2.2.2 The Morphology Approach

This approach considers anatomical details in the reconstruction process. The user sets up the morphology of the face, by including muscles and sometimes fat, before ending the reconstruction by putting on the skin layer.

The work of Davy [30] represents a recent example of this type of system. In her work,

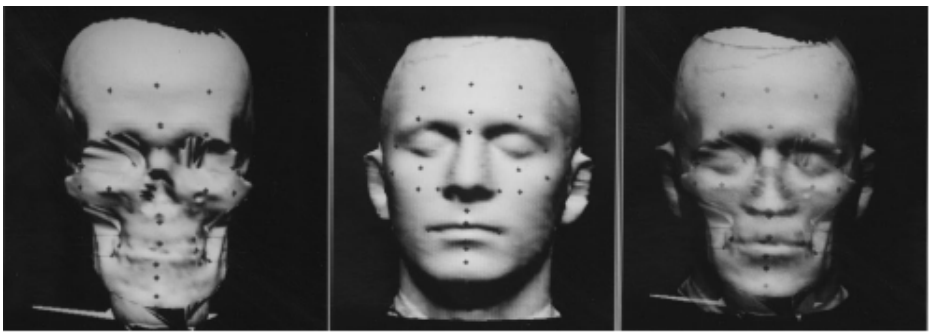

Figure 2.3: (a) Digitised image of skull with landmarks marked. (b) Male facial template with landmarks marked. (c) Superimposition view of the skull with the reconstructed face with landmarks aligned (taken from [104]).

a Non Uniform Rational B-Spline (NURBS) is used to model the soft tissue structure of the human head, skin and muscles. The muscles are modelled using elliptical cross sections lofted into surfaces that were correlated with established diagrams of craniofacial muscles. These are used together with tissue depth landmarks to indicate the depth of the soft tissue over the surface of the unknown skull. Although this work is an alternative to speed up the process of reconstruction, it is based on the same sources of information as in traditional methods.

In the work of Kolja [51] a precise reference anatomical model of the head is fitted on the unknown skull using correspondences between face and skull landmarks. The model can be animated in a physics-based manner by using the muscle structure defined over the model. The basis for finding the deformation between the reference model and the unknown skull model is the definition of a set of facial feature points related to the skull. A multilayer polygonal model simulating the different layers of soft-tissue, muscles and bone is modelled and adapted to fit a model of a human skull.

The morphology approach to model the human face has also found applications in other areas of medicine. Koch used this approach to plan facial surgery [48]. He employs a non-linear, globally continuous finite element model of the facial surface that is based on triangular polynomial shape functions. In the deformable model literature, a triangular polynomial shape function is a surface approximation method used to model the deformation of a continuous surface by means of its triangular mesh approximation. The shape of the surface is controlled by a set of parameters defined at each element of the mesh (associated to the vertices and edges of each triangle) and a polynomial function [17]. Additionally, with some of these models it is also possible modelling other complex changes in the constructed model such as age changes.

2.2.3 The Registration Based Approach

For this type of approach it is necessary to create a reference head model made up of a skull and face pair. The reference skull is then registered with the model of the unknown skull in order to compute a 3D deformation. This deformation can be applied to the reference face in order to estimate the unknown face.

Michael and Chen [64] use a template of a reference head model H_r with an associated

skull model S_r which is deformed using a function designated as volume distortion V. In this process, the deformed reference skull is approximated and matched to the unknown skull S_u. Additionally, it is assumed that the deformed reference model $\hat{H}_u = V(H_r)$ will produce a good similarity model near to the unknown head model. In Jones work [45] the unknown skull is digitised using a CT scanner. A reference head is chosen that has the same sex, race and age characteristics as the unknown skull. A correspondence is created between the two heads consisting on a set of anatomic landmarks matched automatically between the reference and the unknown skull. The correspondence is determined by means of a 2-dimensional cross correlation between a pair of images. Figure 2.4 shows all the stages of this process. The figure shows a pair of skull images (middle), one showing a reference skull with a set of pre-defined marked points (right) and the other showing the unknown skull with the predicted matching points (left). Using this correspondence the soft tissue from the reference head is mapped onto the unknown skull giving an approximation to the unknown face.

Similarly in the work of Tu [98], a skull and a face surface are extracted from a CT head scan. By manually establishing point correspondences between the CT reference skull and the unknown skull, the CT reference face can be morphed to coincide with the unknown skull. By morphing each head scan in the CT database, a collection of estimates of the subject's face is generated. These estimates can be considered as samples of a face space. Given these estimates, a principal component analysis is applied to determine the main modes of variation found in the deformation process.

In the work of Arridge et. al. [7] and Quatrehomme et. al. [74] a method is presented where a facial reference model is warped in order to create the facial reconstruction. The facial reference is selected from a set containing models of individuals of different race, age and sex. This model is adjusted to fit a set of landmarks (previously placed by hand) on the digitised model of the unknown skull. The previoius techniques produce statistically valid models if the unknown skull belongs to one of the races, and corresponds in age and sex to one of these included in the database.

As pointed out by Subsol [95] the registration approach is one of the most promising because these methods "don't require any anthropological measurements or complex anatomical knowledge and can be based on the whole surface data of the skull and face".

2.3 Summary and discussion

Although all the methods described above provide alternatives for improving facial reconstructions in some aspects, the accuracy of the faces produced by these methods rely on the amount and quality of the anthropometric data available. A computer algorithm can only produce results as good as the information that has been input. In most of the cases, the data used contains limited information about the skull-face relationship in either (or both) of two aspects: the number of landmark points and the number of individuals sampled. For instance, in the morphology and morphometric methods, the small number of anthropometric landmarks available to establish the skull-face relation has to be compensated with human expertise. This affects the capability to create repeatable and less subjective reconstructions. In other cases, such as in the registration-based techniques, the access to a limited number of samples of individuals from specific populations can produce a biased result.

Even though the skull is the most important factor defining the shape of the face, there are other factors such as the age, gender and body-build which also impact on facial

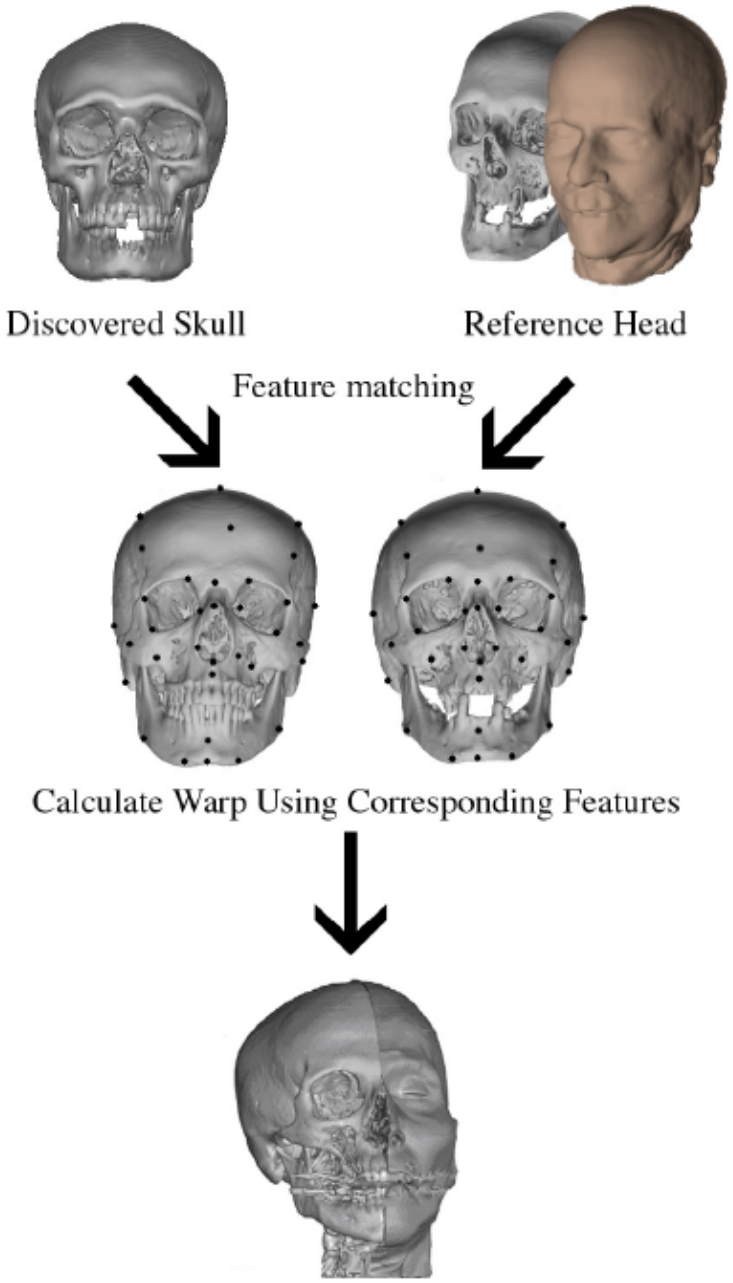

Figure 2.4: Schematic diagram of the reconstruction process taken (reproduced with permission of Mark W. Jones [45]).

appearance. Any craniofacial reconstruction system aimed to create more objective and reproducible results requires large amounts of quality data covering this diversity. More extensive and accurate data should lead to more predictable and consistent results.

Most of the existing sources of information have limitations in several aspects:

- Origin of the data. The aim of CFR techniques is to produce estimations of faces resembling live individuals. Sometimes the data available was collected from cadavers. This data presents measurement variations due to post-mortem changes and distortions of the human body.
- Acquisition methods. Most of the data were generated using manual methods, e.g. needle insertion techniques, CT scan images measured by hand, ultrasound manual measurements.
- Limited information. Data is collected at sparse data points on the face. Standard tables contain 30 points on average.
- Problems in defining a standard interpretation for the rules for identifying some landmarks.
- Data diversity. Collected datasets are particular to a specific type of population (e.g. Caucasian adult corpses). Sometimes this data is used to reconstruct faces of individuals from different populations.
- Limited number of individuals sampled.
- Sampling period. Authors such as Stephan [91] argue that population alimentation habits have changed in recent years producing a variation in the tissue depths of new generations.

For morphometric approaches to craniofacial reconstructions, the results which have been achieved rely on the quality of these traditional sources of information. For morphology approaches, the information about anatomical elements (such as facial muscles) is combined with standard anthropometric data to produce face estimations. This new variable involved in the analysis, the anatomy of the muscles of the head, is known to a limited extent. Some craniofacial muscles have no attachment to the skull but rather originate and insert into the soft tissue alone. Stephan et. al. argue that errors in predicting soft tissue features that have little or no association with the skull are probably large [92, 90]. The complexity of modelling the muscles of the face can complicate even more the design of systems with some degree of repeatability.

In the case of registration-based methods, most of the described work makes use of CT technologies to create the template models. Although it is relatively easy to extract the skull and face models from these volumes, using CT can be considered a drawback. It is difficult to generate a satisfying reference database, because most cranial CT scans of living individuals are only taken in a limited field of view to reduce X-ray exposure [62]. Even with a low-dose CT scanning protocol, "it is not wise -and in some countries not allowed- to acquire CT data from healthy volunteers" [62].

A further problem is accurately identifying and locating meaningful anatomic landmarks in the skull and face in a consistent way. Even with more and more extensive sources of information, a method is required which can match comparable features between different skulls in an automated way. The success of template-based approaches relies on an accurate and consistent matching process.

In this thesis, we will propose a computer based craniofacial reconstruction technique. This technique is a registration technique based on a template-deformation approach. The main difference with respect to other computer based techniques is the type of data used for generating the facial reconstructions. The skull-face models will be generated from MRI datasets. Previous attempts have been done for generating anthropometric data of the head from MRI without success, due to the problem of skull extraction. This dissertation proposes a technique to overcome this problem. The following chapters cover the techniques needed to generate these anatomical models.

Chapter 3

Building 3D Head Models from MRI Data

Although there are several factors influencing the performance of a computer based facial reconstruction system one of the key aspects is related to the quality and quantity of the skull-face information sources. Currently, these sources are limited in size (number of individuals measured), number of measures taken for each subject, diversity of the subjects sampled (i.e. persons of a specific ethnic group, age, etc.)

In this dissertation, we create a method to generate this skull-face information through 3-dimensional models extracted from MRI data. In these detailed models of the skull and face, it is possible to study the dependence between these two elements at a high level of precision.

This chapter is divided into three main parts. In section 3.1 a description of the MRI datasets used in this work is presented. Section 3.2 describes the method used to extract the skin layer. In section 3.3 some of the main issues of the skull extraction process are presented together with an overview of the previous work on skull segmentation. Chapter 4 and 5 then present the two segmentation techniques developed in this research. In chapter 4, a technique based on extracting contours of each image of a MRI dataset is formulated. The contours are restricted by a shape term and then joinined into a 3D model. Chapter 5 presents a 3-dimensional technique based on a template deformation approach. This extends the ideas developed in chapter 4.

3.1 MRI dataset

MRI technology can produce detailed pictures of organs, soft tissues, bones and other internal body structures. Single MRI images taken at equally spaced parallel planes called slices are stacked to create a volume. Figure 3.1 shows an example of the MRI head volume of the Visible Human Project [4, 89].

One of the central hypotheses of this research is that MRI data is a potential source of information to analyse the relation between the skull and face at a high level of detail. Due to the differences between image features of the skull and face, the information of these elements is obtained using different methods. The intensity properties of the skin pixels in MRI, such as high contrast and homogeneity, make the area of the skin easy to extract. In contrast, skull pixels cannot be easily classified due to the low response of the bone tissue to the magnetic field induced by a MRI scanner. However, MRI technologies offer a non-invasive secure scanning alternative for acquiring anatomical information of

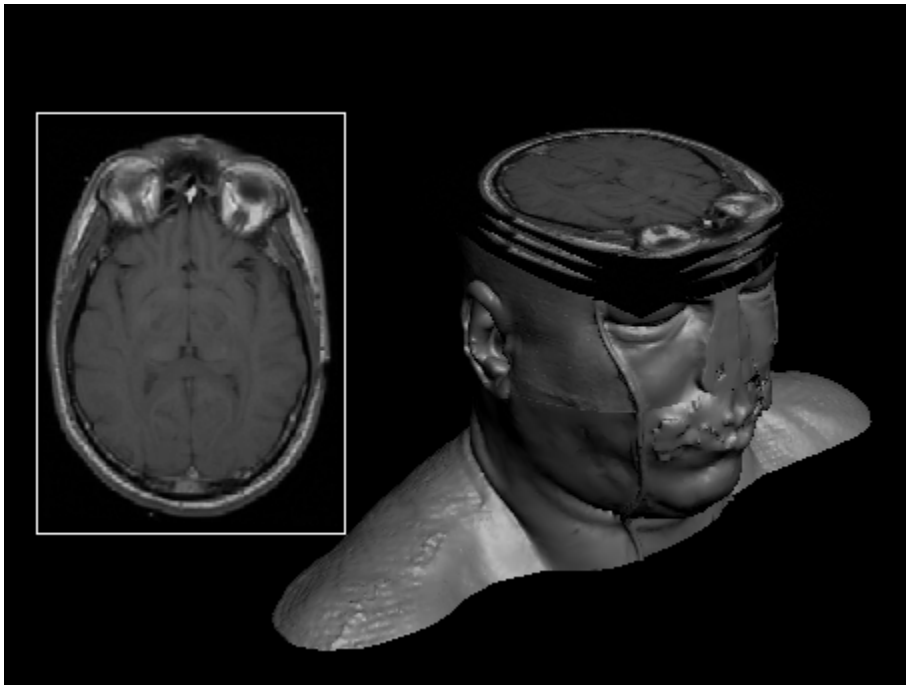

Figure 3.1: The magnetic resonance male dataset from the VHP project [4, 89]. Left: a typical MRI scan image. Right: the structure of the volume.

the skull and face.

Two datasets have been used for conducting experiments: The visible human project (VHP) dataset and the University of Sheffield (UOS) dataset. The VHP dataset was used for testing the 2D skull segmentation techniques presented in chapter 4.The UOS dataset was used for testing the 3-dimensional approach described in chapter 5. Also, it was used for creating the database of skull-face models used in the craniofacial reconstruction experiments of chapter 6.

3.1.1 The Visible Human Project Dataset

This dataset was obtained from the Visual Human Project from the National Library of Medicine, U.S.A.[1]. The dataset was designed to serve as a common reference for the study of the human anatomy as a set of public-domain data for testing medical imaging algorithms and model for the construction of image libraries [4].

The male dataset used consists of axial MRI images of the head and neck taken at 4 mm intervals and longitudinal sections of the remainder of the body also at 4 mm intervals. The resolution of the MRI images is 256 pixels by 256 pixels. Each pixel has 12 bits of grey tone. The CT data consists of axial CT scans of the entire body taken at 1 mm intervals at a resolution of 512 pixels by 512 pixels where each pixel is made up of 12 bits of grey tone. The axial anatomical images are 2048 pixels by 1216 pixels where each pixel is defined by 24 bits of colour. Each image consisting of about 7.5 megabytes of data. The anatomical cross-sections are also at 1 mm intervals and coincide with the CT axial

[1] Visible Human Project web page: http://www.nlm.nih.gov/research/visible/visible_human.html (last accessed March 2010)

images. There are 1871 cross-sections for each mode, CT and anatomy, obtained from the male cadaver.

A geometric model of the skull of the same individual was obtained from the large geometric models archive database available from the Georgia Institute of Technology[2]. The model is shown in figure 3.3. The entire dataset consists of 4,715,110 triangles and their normal vectors stored in a "ply" format file representing the bone structure of the VHP male. This data was extracted using marching cubes from CT slices, and was then simplified using the polygon decimation algorithm. Figure 3.2 show an example of the different modalities of the dataset. In the case of the MRI images there are available in t1 and t2 modalities[3].

MRI produces cross-sectional images of the body. It uses a strong magnetic field and radio waves to produce detailed computerized images of the inside of the body. MRI scans of the head have been widely studied and commonly used to examine the brain. This technology provides high soft tissue contrast in a non-invasive manner.

3.1.2 The University of Sheffield dataset

This dataset was obtained thanks to the collaboration with Dr. Martin Evison[4] from the Forensic Pathology Department and Dr. Iain Wilkinson from the Academic Unit of Radiology from the University of Sheffield. In February 2004, the University of Sheffield organised a project which was funded by the Royal Society of London. The purpose of the study was to help recreate facial appearance from the skull by computer. MRI scans of 60 subjects were taken from their head and neck, and recorded the following biographical information: age, sex, ancestral affiliation (ethnicity). Additionally, information of whether the individuals relatives were also volunteering was also recorded.

The MRI scan and biographic information is maintained in secure databases by the University of Sheffield. The University keeps the MRI scans and biographical information database so it can continue to be used by researchers interested in craniofacial anatomy. This may include scientists and doctors interested in neuroscience, craniofacial surgery, development of the face or archaeological facial reconstruction, for example. It will not be used for any purpose other than scientific and technical research. A copy of the information sheet and consent forms used for the project is included in appendix G.

The dataset consists of MRI scan volumes of 60 individual heads. An example of the images is shown in figure 3.4. Each set contains 200 gray-scaled sagittal images with a resolution of 256 x 256 pixels. The format of each image is 16 bit per pixel raw data with information of approximately the aorta level and up.

[2] Large geometric models archive, U.S.A., Georgia Institute of Technology, web page: http://www.cc.gatech.edu/projects/large_models/
(last accessed: March 2010)

[3] From a medical perspective, it means that MRI can provide multiple channels to observe the same anatomy. Different tissues appear differently in both images. White matter appears in a light grey in T1 and a dark grey in T2. Grey matter appears grey in both images. The Cerebro-Spinal Fluid (CSF) appears black in T1 and white in T2. The background of the image (air) appears black in both images. For further details the reader can consult [2, 3].

[4] now at the university of Toronto: martin.evison@utoronto.ca

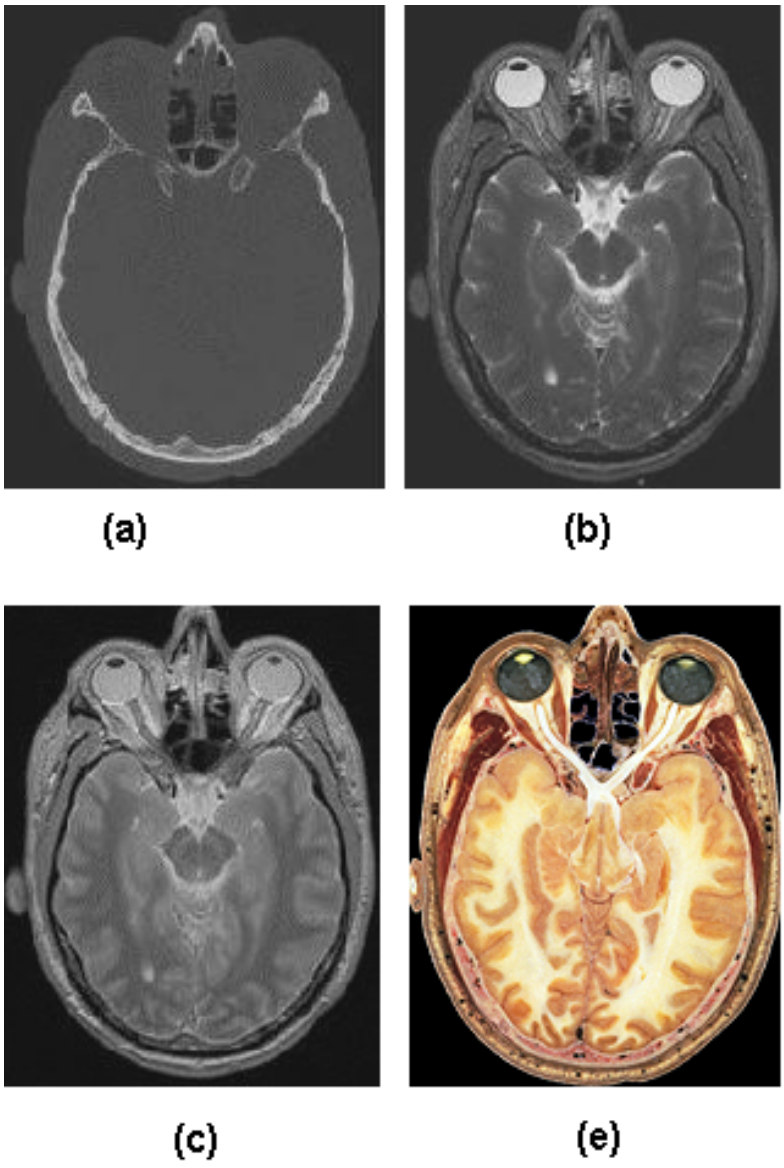

Figure 3.2: Samples of image modalities in the VHP dataset. (a) CT image (b) MRI slice type t1 (c)MRI slice type t2 (c) Color picture. ([89, 4])

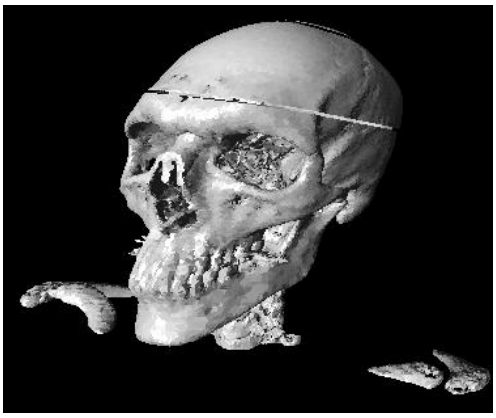

Figure 3.3: The 3D geometric skull model of the VHP male.

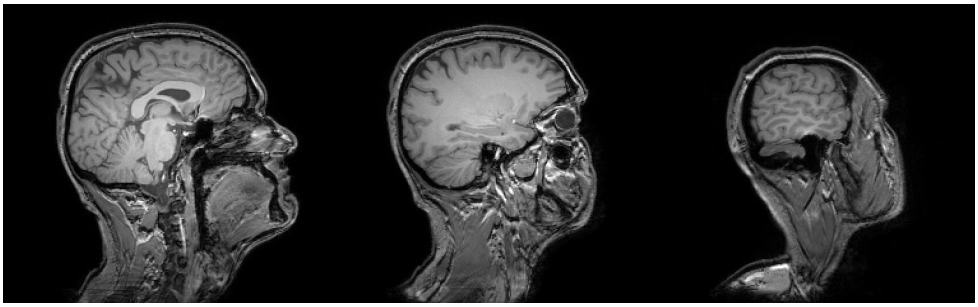

Figure 3.4: Three images at different levels of subject 22 of the UOS dataset.

3.2 Skin layer extraction from MRI data

The main stages of the skin layer extraction are shown in figure 3.5. To extract the face, it is necessary to remove the background information of the volume and select the border area of the head. An isosurfacing technique is used to acomplish this objective. Regions of the volume with intensities above a given threshold are selected by means of an intensity value (called iso-value). This selection creates a sub-volume region containing the area of the head. Depending on the border regions found in the volume, the isosurfacing module generates a set of 3D surfaces (a multi-layer model of the head). This multilayer model contains information of the internal and external structure of the head. The extraction layer module takes this set of surfaces and selects the most external surface of the set, i.e. the surface of the face.

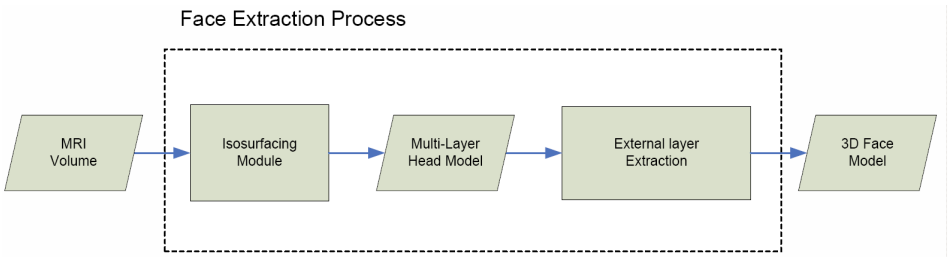

Figure 3.5: Components of the face extraction process

Considering an analysis based on volume elements and applying it to the MRI data, each volume element has to be examined to determine if that element belongs to the region of interest (in this case, any region of the head). The facial surface is obtained by using a technique of surface reconstruction in volumetric data. This technique is explained in the following sub-section.

3.2.1 Surface Reconstruction Using Volumetric Data

The Marching Cubes algorithm [58] is considered to be the standard approach to the problem of extracting iso-surfaces from a volumetric dataset [18]. The iso-value defines a threshold value used for selecting pixels with intensity values within the range of the intensity values of the surface of interest. For this reason this technique can be classified as a low level technique. It is a very practical and simple algorithm, although it has some important shortcomings: topological inconsistency, algorithm computational efficiency and excessive output data fragmentation [66].

The success in the application of iso-surfacing techniques is guaranteed when the images are already segmented and it is only needed to retrieve the 3D structure of the object or, the interest regions in each image can be separated by intensity, texture, colour, or velocity of the regions (in the case of sequences of images taken at different times). As the pixel intensities of the skin meet these requirements (intensities above a threshold value), the geometry of the face can be retrieved directly by this kind of technique.

The Marching Cubes algorithm [58] forms cubes between two adjacent planar data scans. The space defined by a volume is divided into 3D cubes. By analysing the information of single cube units it is possible to establish how an iso-surface intersects the current cube. The process is repeated for each cube in the volume and after processing the whole

data, a surface approximation is obtained for the given iso-value. A threshold iso-value is used to distinguish between relevant and irrelevant information. Using a look up table (where all the possible cases of intersections of the surface with a current cube are stored) optimises the process.

If we classify each corner of the cube as either being below or above the isovalue, there are 256 possible configurations of corner classifications. Two of these are trivial (i.e. where all points are inside or outside the cube does not contribute to the isosurface). For all other configurations we need to determine where, along each cube edge, the isosurface crosses, and use these edge intersection points to create one or more triangular patches for the isosurface. Figure 3.6 shows the lookup table used for selecting the possibilities of surface intersection with a cube. Each number represent the corners of the marching cube numbered from 0 to 7. Red dots represent points of the cube that are above the iso-value and blue points represent points below the iso-value. If symmetry is taken into account, there are really only 14 unique configurations in the remaining 254 possibilities. When there is only one corner less than the isovalue, this forms a single triangle which intersects the edges which meet at this corner, with the patch normal facing away from the corner.

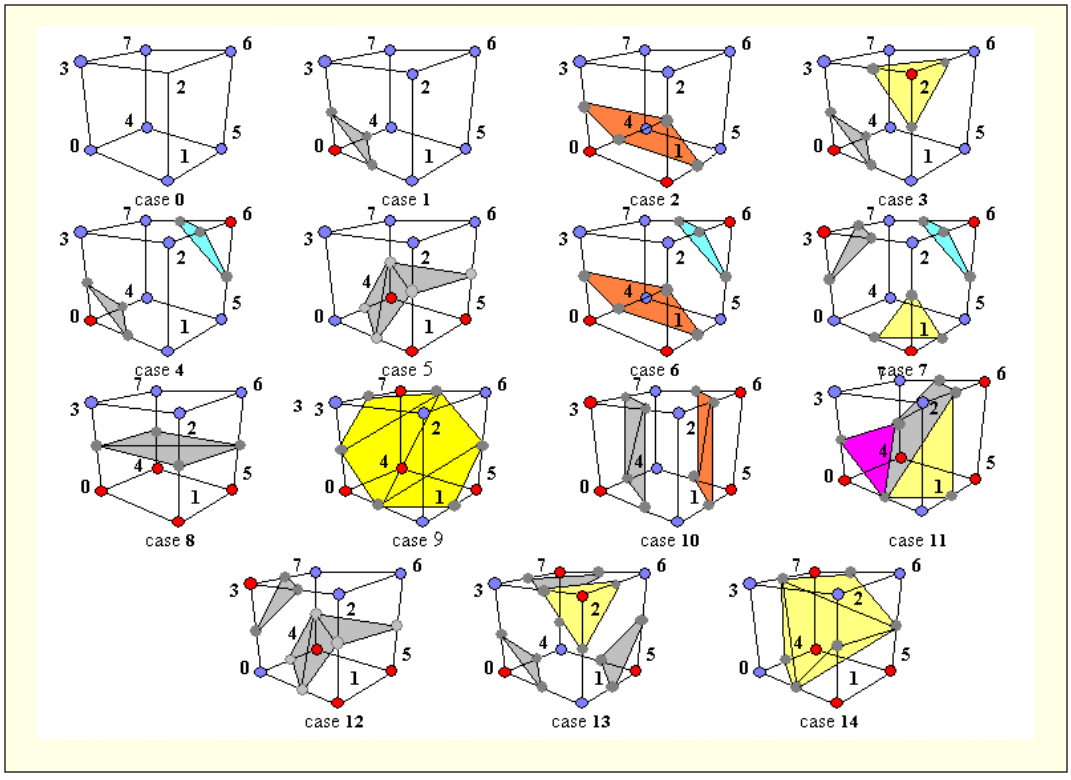

Figure 3.6: The lookup table used to extract the iso-surfaces.

Figure 3.7 shows two datasets created using implicit functions of the form $v = f(x, y, z)$ with the resulting volumetric dataset segmented using the marching cubes algorithm.

The skin surface is separable in terms of its intensity pixel values, and acceptable results are obtained using the marching cubes algorithm. Figure 3.8 shows the result of applying marching cubes to the subject 22 of the UOS dataset.

To segment the skull, the situation is more complicated because of the variation in

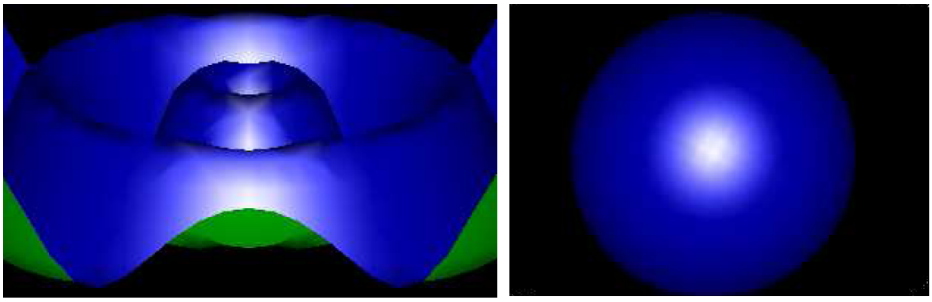

Figure 3.7: Examples for illustrating the potential of Marching Cubes Algorithm to approximate continuous smooth functions: (a) 2-dimensional version of the Sinc function an (b) a sphere. The approximation results obtained when processing real data are determined by the resolution of the sampling step. In our case the sampling step in the MRI used is 1.2 mm approx in each direction.

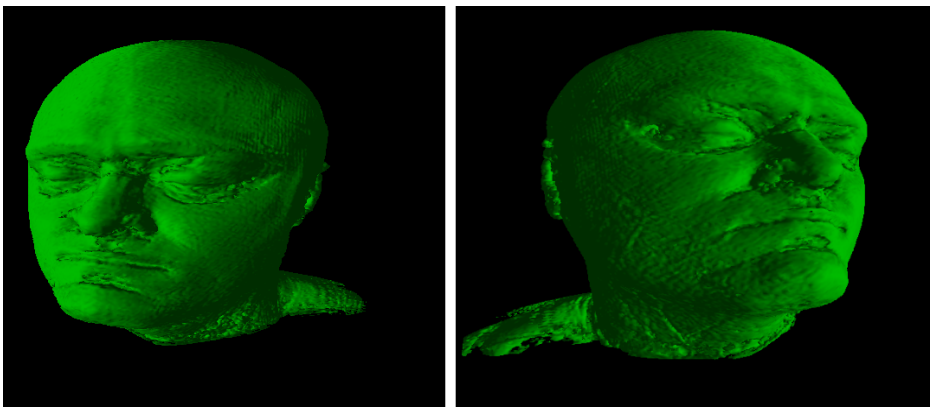

Figure 3.8: The result of the Marching Cubes algorithm applied to the subject 22 of the UOS dataset.

pixel intensities of bony areas in MRI. The next section describes the main problems found in skull segmentation together with an overview of the previous work related to the problem of skull segmentation in MRI data.

3.3 Skull extraction

For several years, the classification of the tissues of the human head in medical imaging has been a topic of interest in areas such as forensic anthropology in order to have a better understanding of the relationship between the skull and face morphology [52, 103, 54]. However the use of MRI technology has been limited due to the problems of how to consistently identify and group bone pixels in these images. Figures 3.9 and 3.10 show some examples of the skull topology at a given slice of the head (in which skull regions are characterised, in a high percentage, by dark pixel areas) and some of problems present in identifying these areas.

There are several issues to solve for segmenting the skull in MRI. The chemical bone

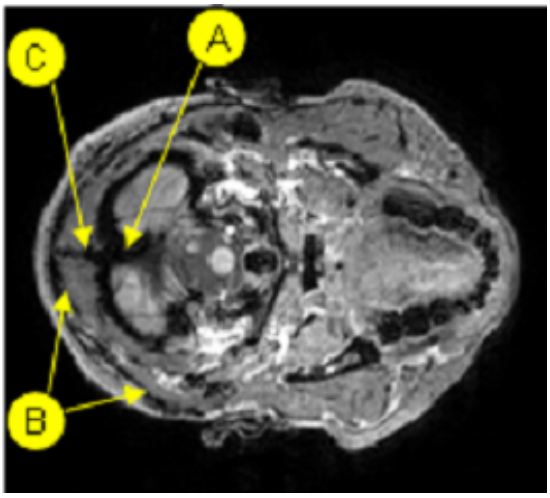

Figure 3.9: MRI scan, showing 3 different problematic areas of the skull. (A) Skull Mixed with other tissue and air. (B) Not bone areas with similar intensities. (C) Area where it is difficult to identify the border of the skull region.

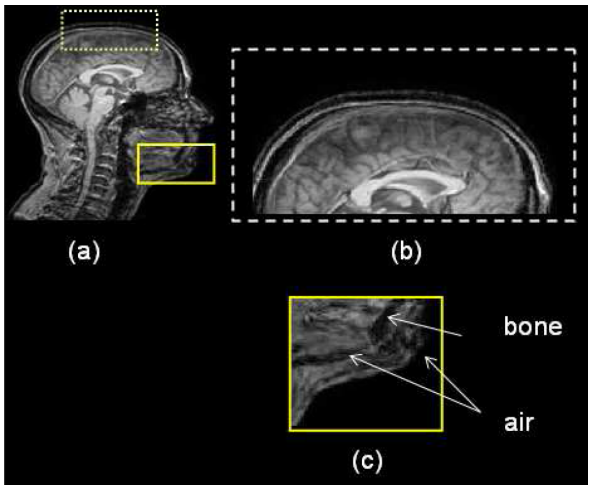

Figure 3.10: Image showing two areas where the borders of the skull are difficult to determine. The original MRI slice is shown in (a). The area at the top of the skull (b) the bone layer is thin with respect to the sampling resolution of MRI scanner. In the area shown in (c), it is difficult to set a border between the skull and the air and other tissues.

composition which causes a weak response to magnetic stimulus making skull areas appear mixed with air and other low intensity tissues. Another problem is the heterogeneous pixel intensity in bone areas. The high variability in pixel intensities makes it difficult to consistently group skull elements. The skull topology is another factor that makes the segmentation process difficult. It is difficult to predict the changes in the skull structure between consecutive images in the volume. The sampling rate of the scanning device sometimes is too low and that causes problems to detect thin skull areas (i.e. some skull areas seem to be disconnected when they are not).

Even though the borders of the skull are difficult to determine only from pixel intensities in MRI, from a visual inspection of the images it is evident that there exist some well defined areas of the skull that can be taken into account to guide a segmentation algorithm. Identifying these areas, and complementing that information with anatomical information about what constitutes a skull shape, makes it is possible to create good approximations of the borders of the bony areas. The idea of using an approximate template with shape constraints is a key aspect of the technique proposed in this research.

3.3.1 Previous work

In the area of image segmentation, previous work has tried to extract the skull from MRI by considering intensity homogeneity properties of bone regions. Salas and Succar [80], Jere [43] and Dogdas [33] propose methods for extracting the skull based on spatial processing of the volume using mathematical morphology operators.

These algorithms discard non bone areas by removing background voxels and classifying other separable types of tissues such as the scalp and the brain. The result is a set of voxels representing possible skull regions. These regions are then processed with mathematical morphology operators in order to regularise regions of connected components. Closing holes and removing weak edges and noise of certain image regions, mathematical morphology algorithms are used to extract the image components describing skull areas under the assumption that certain shape regularity in these regions is present. However, the conditions assumed in the techniques related to the regularity of skull regions can only be guaranteed in the upper part of the skull (cranium). For this reason, these algorithms produce acceptable results only in that area.

In contrast, the algorithm proposed in this thesis produces models of the entire skull volume, accounting for the most probable configuration of the skull regions provided by volume features. The approach proposed in this work takes into account probable skull components of the MRI volume in a holistic formulation, even if these components are not connected with each other. Additionally, each of the skull models produced in this research shares a common structure (i.e. the same triangular mesh structure) which facilitates locating important features and conducting statistical analysis of the models.

Whilst probabilistic approaches for classifying tissue types have also been applied successfully to segment body organs in medical images [23, 106, 24, 13], their application for the problem of skull segmentation in MRIs has failed to produce acceptable results in the frontal area of the skull [33]. These approaches assume that voxels possess specific homogeneous attributes allowing their classification in terms of intensity, colour, texture or movement. With models of parameterised distributions for each type of tissue, they try to solve the partial volume problem in order to produce adequate classifications. Examples of these approaches are the works of Leemput et. al. [55, 56], Laindlaw [53] and Heinoen [41].

However, these separability assumptions of tissue types are difficult to meet when

presented with skull regions in MRI. The air and the skull voxels have practically no difference in intensity, colour or texture attributes. The only difference between these two types of tissue is the spatial position of each voxel with respect to the global spatial structure of the head. Figure 3.11 illustrates this with a 2D example (a 2D example is used for simplicity). Also, there exist regions of the skull with high variations in their intensity values, especially in those areas of the skull with high concentrations of fat. In contrast, to the intensity properties of most bony regions, fat produces voxels with very high intensity levels becoming indistinguishable[5] from other types of tissue such as the skin or brain. In summary, in the case of the skull the homogeneous intensity property assumption cannot be guaranteed.

The technique proposed in this thesis is designed to deal with this type of problem. The algorithm proposed takes into account the spatial position of candidate skull voxels with respect to the structure of the probable skull they are describing, integrating relevant voxels in a single structure. During the segmentation process, some of the candidate skull voxels may or may not belong to the skull. To decide what voxels are considered, the algorithm proposed has a mechanism for compensating for missing parts of the skull but also removing outliers and noise according to a statistical model.

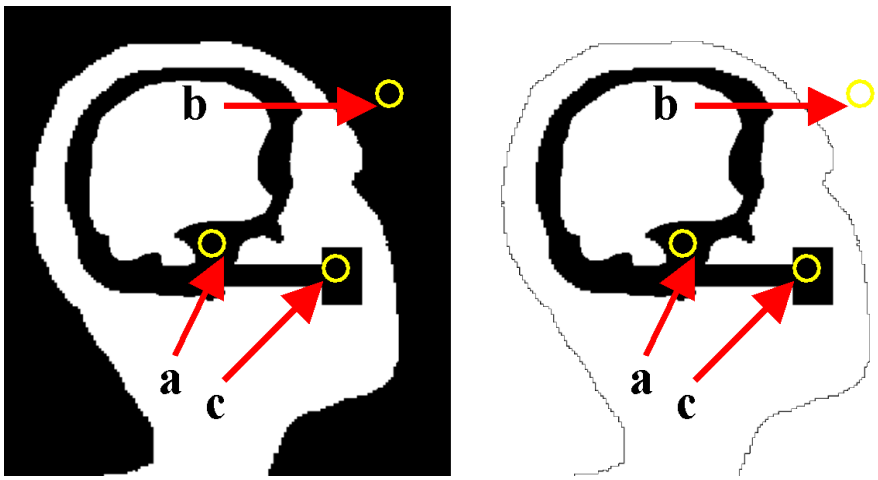

Figure 3.11: Binary images showing two examples where traditional techniques of tissue classification fail to detect skull areas. (Left) The picture elements in area (a) have exactly the same intensity, colour and texture as picture elements in regions (b) and (c). (Right). Even removing the background regions, it is not possible to differentiate between skull and non skull picture elements from regions (a) and (c).

Deformable methods guided purely by voxel intensities are another type of technique that have been used for MRI skull segmentation. The works of Rifai [77, 76], Mang [62], and Ghadimi [39] are examples of these techniques. These techniques rely on separability and regularity assumptions of the materials to segment, assumptions previously discussed that are difficult to guarantee in the case of skull regions in MRI data. The main problem with these techniques is that when considering only intensity information to guide the deformable model, there is the possibility of being attracted to incorrect boundaries. Also, the results are highly sensitive to the initialisation of the deformable model. These

[5] considering pixel intensity values

problems are overcome in our approach by a pre-registration step at the initialisation stage. At each step of the algorithm, by combining the information provided by the image features, a gradient vector flow (GVF) field, and the shape term statistically derived it is possible to guide the segmentation process towards a statistically valid result.

The method proposed by Shan [85] for segmenting the skull combines CT and MRI in a registration approach. A set of skull models generated from CT segmentations is used for segmenting skull data in MRI modalities. Similar work is presented by Vandermeulen [100] to create craniofacial reconstructions involving head models obtained from CT scans. The main drawback of these techniques is that they require a number of CT scans in order to produce the initial skull models. CT scans produce a high radiation dose that can be harmful to healthy people. In this research we are interested in the study the skull-face relation obtained from live people rather than from cadavers to avoid the effect of tissue depth changes due to dehydration. Another disadvantage is that the segmentation produced is simply a collection of isolated voxels that in a second stage have to be integrated to create a skull model.

In contrast, the technique proposed in this thesis only requires MRI to extract the skull which makes this technique suitable to collect more data of live people, since MRI is an acquisition technique that is not harmful, and provides very detailed information of several tissue types present in the head. Additionally, as mentioned before, the results of the research presented in this thesis are complete skull models, which can be considered as a high level representation. These representations provide flexible models with several advantages for referring to specific anatomical parts of the skull in an explicit way.

An approach similar to the work presented in this thesis is presented by Luthi et. al. [59]. In that work, a deformable model of a skull is used to segment the skull in a pre-processed MRI head volume. The skull and the deformable model are registered using a landmark based approach. To maintain the shape of the deformable model a shape term is used. This shape term is defined with the principal component analysis (PCA) coefficients of a statistical model of skull shapes. The deformable model mesh is deformed under the shape restrictions at each step of an iterative algorithm. To impose more control on the shape, the deformable model is defined at different level of details and used for processing several times the head volume. The statistical skull model requires several skull samples to be constructed. In contrast, our technique proposed, uses a deformable model with the same level of detail during all the process. The registration method used in our work, is a 3D curve approach in prominent areas of the skull. The covariance regularisation step incorporated in our approach, makes the shape term calculation more robust and requires less skull models to train (only one model is needed as a minimum).

In this thesis, two techniques using a common approach have been developed to deal with the skull segmentation problem. They will be presented in chapters 4 and 5. In chapter 4, a 2D skull segmentation technique using an active contour including shape information is formulated. Based on the 2D approach, chapter 5 presents an extension to produce a 3D technique in which a defermable model controlled by a shape term is used to extract the skull from the head volume.

Chapter 4

Skull Segmentation in MRI Datasets Based on Contour Extraction

In this chapter, a method to generate 3D models of the skull from 2D MRI images is presented. As described in chapter 3, the skull and face models produced in this research will be used to create a database of head models to study the skull-face relationship. The possibility of producing these models provides, in contrast to traditional anthropometric tables, dense correspondence models in which any region of the face can be analysed in terms of a corresponding surface at the skull. The method presented is based on a contour extraction approach. A set of contours are extracted from each MRI image and joined to reconstruct the 3D model.

Section 4.1 gives an overview of the stages that have to be covered for defining the solution for the skull segmentation problem. Section 4.2 presents the active contour formulation. Section 4.3 describes the theory of gradient vector flow (GVF) snakes. Section 4.4 presents the shape modelling aspects that need to be addressed for implementing our approach. A set of experiments were conducted to test the segmentation algorithm created and the results are presented in section 4.5. Section 4.6 discusses the results.

4.1 Overview of the approach

In our approach, the skull surface is extracted by segmenting a set of images of an MRI volume. At each slice, the borders of the skull region are modelled as single contours or, when the skull topology is more complex, as a combination of several partial skull contours. The extracted contours are then assembled to create a 3D skull model. The segmentation process is made up of two components. The first component is an active contour [46, 63] directed by image features which 'blindly' tries to enclose skull areas. The second component is a shape term [27] which adds statistical knowledge of the likely shape to find. The two components are combined to make an active contour evolve towards a minimum within the static potential field calculated from the gradient information in the image.

To test our approach, we use the magnetic resonance 3D dataset of the male head from the Visible Human Project [4, 89]. Figure 3.1 illustrates the multiple slice structure of this dataset. A Computer Tomography (CT) volume of the same person is also available. Figure 4.1 shows an example of two modalities for the eye socket region, which is one

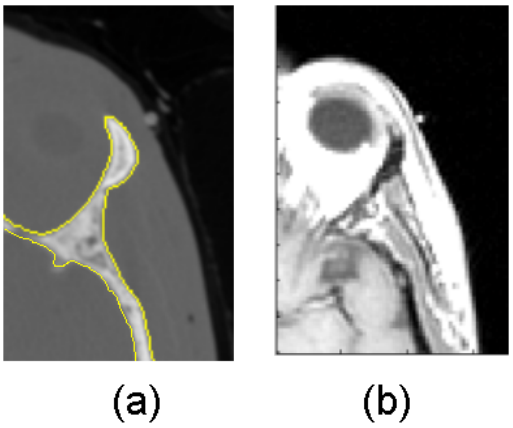

Figure 4.1: Region of the head to segment in two image modalities. (a) CT image scan used as the reference to evaluate the MRI segmentation. (b) MRI scan to segment.

of the most complicated regions for skull segmentation in MRI datasets due to the high variability of pixel intensities of the bone components [41]. To assess the performance of our proposed algorithm, the results of the MR segmentation will be compared with the results of segmenting the same bone area in a CT image, which is relatively straightforward to segment.

Segmenting the skull in a CT image is relatively easy because bone areas are well defined in this scan modality. However, its use is limited because of the involved radiation dose [101]. In contrast, MRI is a safer option for scanning live individuals. Nevertheless, in this modality the chemical composition of the bone presents low response to magnetic stimulus. This property causes bone areas to be partially defined in some portions of the image, and mixed with distinct tissues and air in others, which makes the skull segmentation difficult.

For implementing the shape feature restrictions, there are several aspects to take into account. They are summarised in table 4.1. A deformable model is a geometrical object that can be defined in multiple ways (e.g. as an implicit mathematical function, as a parametric function, etc.) Hence, it is necessary to select an appropriate representation to handle the inherent features related to a skull shape. The shape feature representation models the common shape features defining a skull shape.

A second aspect is the shape learning process. Several samples of skulls are required so that a computational algorithm can "learn" a skull shape. The parameters accounting for the major differences between models of skull contours are translation, rotation and scale. To deal with this invariance, the training shapes have to be aligned in order to be referenced to a common coordinate system.

With a set of skull contour shapes gathered (that will be called the training set), it is possible to create a probabilistic model describing the common features of the contours. The probabilistic model will be used to assign probability values to the elements of the training set, but also, when a new element is given, it will assign a probability value to the new element. This value will be used for measuring similarity properties between the new elements with respect to the family of trained shapes.

The set of features, defining possible skull borders, are used to define a force for

Problem	Method used
Defining the Segmentation Approach image features + shape restrictions	Bayesian approach including shape information
Defining image feature restrictions and evolution conditions	Energy minimisation and Active Contours
Defining shape restrictions representation, metrics and evolution	Shape representation, metrics alignment and invariance
Defining the shape space	Gaussian model to represent shapes, covariance regularisation
Including invariance in the representation	Invariance formulation

Table 4.1: Main issues to solve in the skull segmentation process

attracting the vertices of the active contour[1] towards the borders of skull regions. At the same time the shape term acts by maintaining the structure of the active contour within the limits of a trained skull shape. It is also necessary to define a metric to assess how different the snake is with respect to a valid shape configuration at a given state. A measure must be defined to calculate how far the deformable model is from the family of shapes defined by the training set. A problem is presented when few data are used for creating the training set. Usually, a minimum number of samples is required to model the shape variability. To overcome this problem, we use a method to adapt the covariance matrix of the distribution to allow these situations. These aspects will be covered in the following sections.

4.2 Active Contours

Active contours (or snakes) are widely used for boundary detection in the field of image segmentation and computer vision [1, 42]. The classical approach is based on deforming an initial contour C_o towards the boundary of the object to be detected, making this contour converge to an optimal final state (i.e. a curve at the contour of the desired object) from an arbitrary initial state (i.e. shape and position). The deformation is obtained by minimizing a functional designed so that its minimum is obtained at the boundary of the object [16]. The functional consists of two main components. One component controls the smoothness of the curve and the other attracts the curve toward the image features. These two components are known as the internal and external forces, respectively [97, 46].

Two types of active contour models are common in the literature: parametric active contours [46] and geometric contours [15, 61]. In our work we use an extension to a parametric active contour, defined as a parametric curve moving toward desired features (edges) under the influence of potential forces. A potential force is a 2-dimensional function that assigns a magnitude and a direction of influence to all the pixels in the image domain. In our work, this function is derived from the image gradient and accounts for the influence

[1] We will be using the terms active contour and snake interchangeably to denote a 2D deformable model.

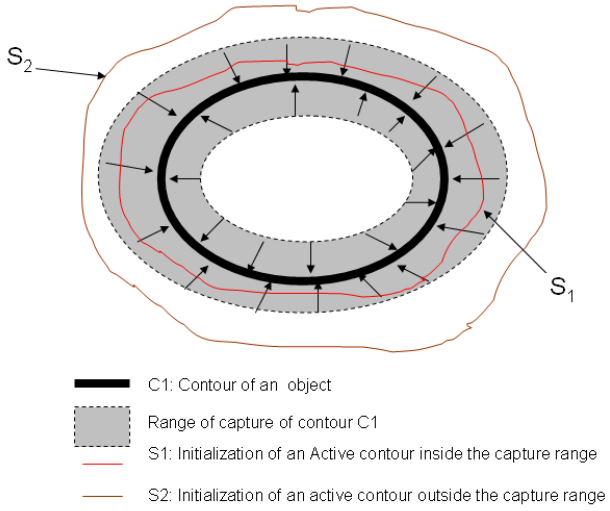

Figure 4.2: Capture range of an elliptic object. The capture range is the area around a feature where a force field is defined to attract a deformable contour. In this example the contour S_1 is under the influence of the border of the ellipse C_1 while S_2 is not. In this case, the contour S_2 will not be deformed.

of the image data on the snake.

In general, the problems which must be overcome with the application of active contours are:

- Initialization: The range of capture of traditional potential forces is small. The range of capture is the area around an image feature where a force potential is defined to attract the active contour (see figure 4.2).
- Concave regions: Difficulties can occur when progressing the curve into concave boundary regions.
- Occlusion Problems: Sometimes it is necessary to deal with missing information in the image.

A traditional formulation for a snake is a parametric curve $X(t) = [x(t), y(t)], t \in [0, 1]$ that moves through the spatial domain Ω of an image in order to minimize the E_{image} functional defined as [16]:

$$E_{image} = \int_0^1 (\frac{1}{2}(\alpha \left|X'(t)\right|^2 + \beta \left|X''(t)\right|^2 + E_{ext}(X(t)))dt \tag{4.1}$$

where $X'(t)$ and $X''(t)$ stand for the first and second derivative of the curve X with respect to t, and α and β are weighting parameters that control the active contour tension and rigidity [46]. The external energy E_{ext} is obtained from the image and reaches its lower values at interest features such as boundaries. The next section introduces the particular kind of active contour we use.

4.3 Gradient vector flow active contours

Gradient vector flow (GVF) active contours are curves under the influence of a potential force called gradient vector flow [113]. The gradient vector flow is an external force computed as a diffusion of the gradient vectors of the image. This force is used to attract the snake towards the edges in the image. The evolution of a GVF snake can be formulated by solving equation (4.1). This solution can be obtained by minimizing the following Euler equation:

$$\alpha X''(t) + \beta X''''(t) - E_{ext} = 0 \tag{4.2}$$

which is equivalent to the following system of forces:

$$F_{int} + F_{ext} = 0 \tag{4.3}$$

with $F_{int} = \alpha X''(t) + \beta X''''(t)$ and $F_{ext} = -E_{ext}$

The term F_{int} accounts for the geometric restrictions of the snake itself (tension and rigidity) and the second term F_{ext} accounts for the evolution towards image features. The external forces F_{ext} can be divided into two classes: static and dynamic [112]. Static forces are computed from the image data and do not change as the snake progresses. Dynamic forces are those that change as the snake deforms. We use a static GVF force, which is a type of static external force independent of the time and the position of the snake.

To find a solution to equation (4.2) the snake is made dynamic by treating X as a function of time θ as well as the spline parameter t. i.e. $X(t, \theta)$. Then a partial derivative of X with respect to θ is set equal to the left side of equation (4.2) as follows:

$$X_\theta(t, \theta) = \alpha X''(t, \theta) + \beta X''''(t, \theta) - E_{ext} \tag{4.4}$$

When the solution $X(t, \theta)$ stabilizes, the term $X_\theta(t, \theta)$ gradually disappears and we achieve a solution for equation (4.2).

To complete the definition of a GVF active contour it is necessary to define the potential force influencing the curve evolution. This potential force is called the gradient vector flow and it is defined over an edge map of the image. This concept will be introduced in the next subsections.

4.3.1 Edge Maps and GVF field formulation

To define potential external forces acting on the active contour, two traditional formulations are widely used:

$$E^1_{ext}(x, y) = -|\nabla I(x, y)|^2 \tag{4.5}$$

$$E^2_{ext}(x, y) = -|\nabla (G_\sigma(x, y) * I(x, y))|^2 \tag{4.6}$$

Here, $G_\sigma(x, y)$ is a two dimensional Gaussian function with standard deviation σ and ∇ is the gradient. $I(x, y)$ represents the image intensity at a point (x, y). In equation (4.6), the standard deviation is frequently used to control the capture range of the image features (in this case edges). Setting higher values for σ is used to increase the capture range of the gradient forces, but it tends to blur and distort the edges [113].

An edge map can be defined as a 2-dimensional function f as follows:

$$f(x, y) = -E^i_{ext}(x, y) \tag{4.7}$$

for $i = 1, 2$ (equations (4.5) and (4.6)).

In our work, we use E^1_{ext} as the external potential for all the calculations. Using this definition of an edge map the term ∇f represents a field with vectors pointing toward the edges. The gradient vector flow is defined as a potential force with a vector field $\mathbf{v}(x, y) = (u(x, y), v(x, y))$ that minimizes the energy functional:

$$\varepsilon = \int\int \mu(u_x^2 + u_y^2 + v_x^2 + v_y^2) + |\nabla f|^2 \, |\mathbf{v} - \nabla f|^2 \, dxdy \tag{4.8}$$

where μ is a regularization parameter controlling the compromise between the first and second terms of the integral. This definition of ε guarantees that when ∇f is near to zero (uniform regions), the second term will vanish and the field will be dominated by the squares of the partial derivatives of u and v, and it will vary in a very smooth way. If ∇f has a high value, then the functional will be dominated by the second term and minimized when $\nabla f \approx \mathbf{v}$. In other words, this functional will have the effect of keeping $\mathbf{v}$ nearly equal to the gradient of the edge maps when ∇f is the most important component and varying in a smooth way in regular regions.

Using calculus of variations it is known [113] that the GVF field can be found by solving the following Euler equations:

$$\mu\nabla^2 u - (u - f_x)(f_x^2 + f_y^2) = 0 \tag{4.9a}$$
$$\mu\nabla^2 v - (v - f_y)(f_x^2 + f_y^2) = 0 \tag{4.9b}$$

where ∇^2 is the Laplacian operator. Equations (4.9a) and (4.9b) are known as the generalized diffusion equations. Note that in homogeneous regions, the second term of both equations is zero (because the gradient of $f(x, y)$ is zero). These equations can be solved by treating u and v as functions of time θ solving:

$$u_\theta(x, y, \theta) = \mu\nabla^2 u(x, y, \theta) - (u(x, y, \theta) - f_x(x, y)) \cdot (f_x(x, y)^2 + f_y(x, y)^2) \tag{4.10}$$
$$v_\theta(x, y, \theta) = \mu\nabla^2 v(x, y, \theta) - (v(x, y, \theta) - f_y(x, y)) \cdot (f_x(x, y)^2 + f_y(x, y)^2) \tag{4.11}$$

A stable finite difference implementation for solving the steady-state of these equations is given in detail in [112]. The calculated field $\mathbf{v}$, after the minimization process, replaces the potential force E_{ext} in equation (4.4). Figure 4.3(a) shows a CT image of an area around the right eye socket and in 4.3(b) its potential forces derived from the edges of the object (image features).

4.4 Including shape knowledge in the segmentation process

In our work, an additional term is included in the GVF snake formulation in order to incorporate knowledge about the shape to segment in a statistical way. The shape term is an adaptation of the one proposed by Cremers et al. [26, 27]. The novel aspect of our 2D implementation consists of combining image information and previously acquired shape information in a variational framework.

For a contour $C = X(t)$ we will consider the following extended energy :

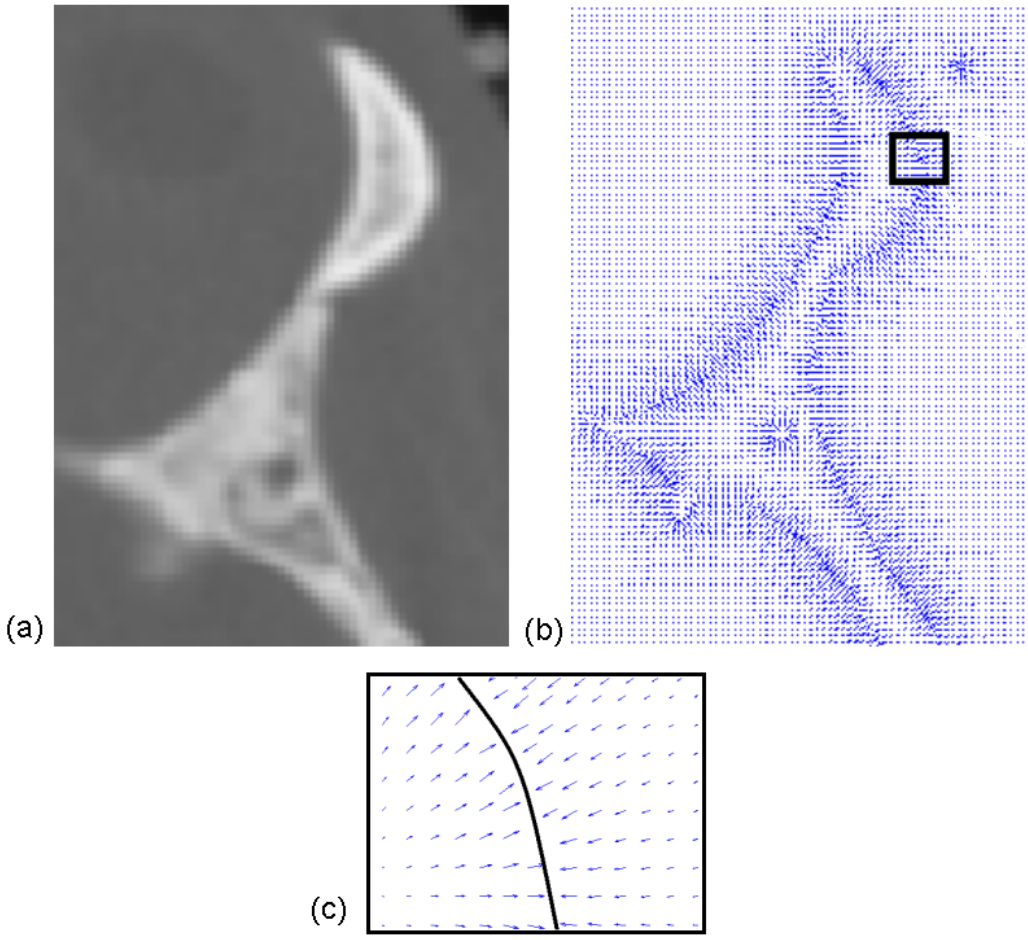

Figure 4.3: A portion of the skull around the right eye socket. (a) Original gray level CT image. (b) GVF field of the image and the rectangular marked area enlarged (c). The black line in (c) represents a portion of the object boundary and the blue arrows the direction of the GVF potential forces.

$$E = E_{image} + \gamma E_{shape}(C) \tag{4.12}$$

where the term E_{image} is the energy contribution of a GVF active contour (see equation 4.1), E_{shape} benefits contours with similar shapes to the one acquired in a shape training process, and γ is a factor to regulate the amount of influence of the shape term. Minimising the energy in equation 4.12 is equivalent to maximising the Bayesian inference term $P(M/f)$ defined by:

$$P(M/f) = \frac{P(f/M)P(M)}{P(f)} \tag{4.13}$$

The term $P(M/f)$ optimises the probability of a configuration for the deformable model M given the observed volume features f (i.e. obtaining the model M that is the most probable according to the information in the image). In general, the term $P(M)$ defined in deformable model approaches usually models the fact that large surfaces are less probable [25]:

$$P(M) \propto \exp(-\alpha \mid M \mid) \tag{4.14}$$

where $\mid M \mid$ is a measure of the area of the model M. In our work this measure will be a more elaborate shape dissimilarity measure:

$$P(M \mid \{M_i\})$$

which is constructed from a set of training models $\{M_i\}_{i=1..m}$.

The training process consists of collecting a set of similar shaped objects. We will adopt the concept of shape defined by Dryden [35], who defines the shape of an object as all the geometric features of the object that are unchanged when it is translated, rescaled and rotated in an arbitrary coordinate system. In this work, the set of geometric features corresponds to a set of points placed along the object contour. The labelling of the control points can be done manually or automatically and the main objective is to create a reference set of control points to model the statistical shape variation.

The effect of combining E_{image} and E_{shape} is twofold. First, it augments the capture range of potential field forces (which leads to less sensitivity to initialization). Second, it improves the capacity of the snake to deal with occlusion problems.

The following subsections describe the derivation of the E_{shape} term of equation (4.12) which accounts for pre-established shape information.

4.4.1 Incorporating statistical shape information

In our work, the active contour C is represented with a quadratic B-spline curve given by [37]:

$$C : [0,1] \rightarrow \Omega, \quad C(t) = \sum_{i=1}^{n} p_i B_i(t) \tag{4.15}$$

where t is the parameter of the spline, p_i is the set of control points, and $B_i(t)$ are the quadratic periodic B-spline basis functions [37, 11].

A 2D object shape s is represented by a set of n pairs of control points $\{(x_i, y_i)\}_{i=1...n}$ defining the curve. The shape s can be referred to as a unidimensional vector with the following structure:

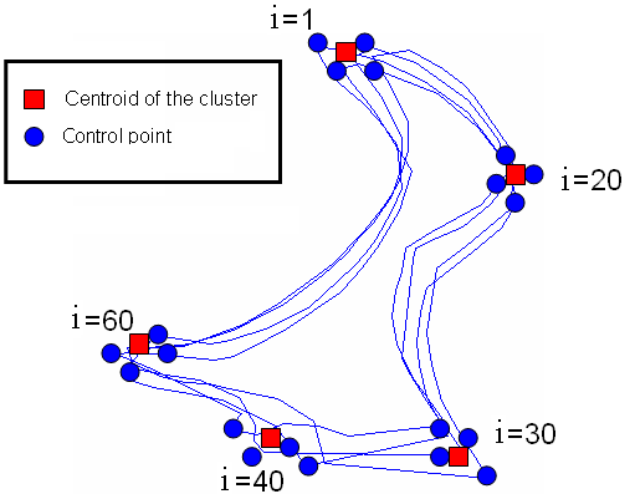

Figure 4.4: The figure shows control points i=1,20,30,40,60 of four training shapes and their related centroids. Each of the shapes is defined by 80 sampled points. The lines in blue show each training shape after alignment.

$$s = (x_1, y_1, ..., x_n, y_n)^T \tag{4.16}$$

The main idea behind the shape formulation is the assumption that each trained shape will have the same number of related control points n and that the spatial position of each control point i can be modelled with a Gaussian distribution. Figure 4.4 shows an example of this configuration for a four-shape training set. From this configuration we can obtain some parameters for the family of shapes as the mean shape μ and the covariance Σ of the set.

The covariance matrix Σ defines a probability measure for the shape space. If the covariance matrix is full rank, its inverse Σ^{-1} exists and the Gaussian probability distribution of the shape s is:

$$\rho(s) \propto \exp(-\frac{1}{2}(s-\mu)^T\Sigma^{-1}(s-\mu)) \tag{4.17}$$

Here, $\propto$ denotes direct proportionality between the left and right expressions and μ is the average shape of the training set. The requirement for Σ to be full rank is only accomplished by having at least $2n$ different training shapes. In practical terms, this can be a strong limitation. To solve this problem, a technique of covariance regularization must be applied in order deal with a number of training shapes less than $2n$.

4.4.2 The Gaussian Model For Representing Shapes

In this work, it is assumed that the training shapes are aligned as defined in the previous subsection and distributed according to a multivariate Gaussian distribution. A statistcal shape model based on principal component analysis (PCA) is proposed to model the shape variability of a given configuration with respect to a set of trained shapes. Here, the model proposed by Cremers [26].

Let $\chi = \{s_i \in \mathbb{R}^{2n}\}_{i=1..m}$ be a set of training shapes, aligned as presented in the previous section with mean vector $\bar{s}$. The sample covariance matrix is given by:

$$\Sigma = \frac{1}{m-1}\sum_{i=1}^{m}(s_i - \bar{s})(s_i - \bar{s})^T \tag{4.18}$$

PCA can be applied to this covariance matrix in order to obtain the main sources of variation in the training set. PCA is an orthogonal linear transformation that transform the data to a new coordinate system such that the greatest variance by any projection of the data comes to lie in the first coordinate (first component), the second greatest variance on the second coordinate and so on. PCA is the optimum transform for the given data in least square terms [44].

The matrix Σ can be diagonalised and a set of $\lambda_1 ... \lambda_r$ eigenvalues can be obtained. The modes of largest variation, given by the vectors e_i, correspond to the largest eigenvalues λ_i. A compact lower-dimensional shape model can be obtained by linear comination of these eigenmodes added to the mean shape:

$$s(\alpha_1 ... \alpha_r) = \bar{s} + \sum_{i=1}^{r} \alpha_i \sqrt{\lambda} e_i$$

where $r < m$. The factor $\sqrt{\lambda}$ has been introduced for normalisation and corresponds to the standard deviation in the direction of the vector e_i.

In general if the number of sampled elements is smaller than the dimension of the underlying vector space ($2n$), the covariance matrix Σ will not have a full rank and the probability density will not be supported in the full $2n$ dimensional space. This situation represents a problem for evaluating the term E_{shape} in equation 4.12 for shape configurations out of the space defined by the training set (as the probability distribution is undefined). To solve this problem, a technique of covariance regularisation is applied. The following section presents a solution to this problem.

4.4.3 Regularizing the covariance

In general, regularizing a covariance matrix is not a trivial process. We follow the approach from [26] to propose an approximation to the solution. The covariance matrix can be expressed as a decomposition into eigenvalues and eigenvectors in the following way: $\Sigma = VDV^T$ where D is the diagonal matrix of non-zero eigenvalues $\sigma_1 \geq ... \geq \sigma_r > 0$, V is the matrix of corresponding eigenvectors and V^T is the transpose of V. The covariance matrix is regularized by replacing all the zero eigenvalues by a constant $\sigma_\perp > 0$. Thus, the new regularized covariance $\Sigma_\perp$ is obtained by means of:

$$\Sigma_\perp = VD_\perp V^T \tag{4.19}$$

$$\text{with } D_\perp = D + \sigma_\perp(I - e_v e_v^T) \tag{4.20}$$

where e_v is an orthonormal basis of the matrix V of eigenvectors, and I is the identity matrix. For this work, as suggested in [26], $\sigma_\perp$ is given by:

$$\sigma_\perp = \frac{\sigma_r}{2} \tag{4.21}$$

This expression guarantees that every possible variation in the shape space will have a corresponding value of probability $\rho(s)$ covered by the new covariance matrix. Better yet,

equation (4.17) will be differentiable on the full space, associating a finite non-zero value with any shape s. Equation (4.17) can be rewritten as:

$$\begin{aligned} \rho(s) &\propto \exp(-\frac{1}{2}(s-\mu)^T\Sigma^{-1}(s-\mu)) \approx \\ \rho(s) &= k\exp(-\frac{1}{2}(s-\mu)^T\Sigma^{-1}(s-\mu)) \end{aligned} \tag{4.22}$$

for an arbitrary proportionality constant k. Applying the logarithm function to both sides of equation (4.22) and using the product rule for logarithms gives:

$$\log(\rho(s)) = \log(k) - \frac{1}{2}(s-\mu)^T\Sigma^{-1}(s-\mu) \tag{4.23}$$

Rearranging, equation (4.23) can be expressed in terms of a function of the shape s :

$$E_{shape}(s) = \log(\rho(s)) + const = -\frac{1}{2}(s-\mu)^T\Sigma_{\perp}^{-1}(s-\mu) \tag{4.24}$$

with $const = -log(k)$.With this algebraic development it is shown that the Gaussian probability in equation (4.17) corresponds to the quadratic energy in equation (4.24) [27].

4.4.4 Metrics of the shape

Given two contours C_s and $C_{\hat{s}}$ a Taylor expansion will be considerated to approximate the following distance metric:

$$\parallel C_s - C_{\hat{s}} \parallel^2 \approx \min_{\pi} \int_0^1 (C_s - C_{\hat{s}}(\pi))^2 ds \tag{4.25}$$

which accounts for all continuous and monotonic reparametisations. We use an approximation using Mahalanobis distance by a simpler Euclidean distance d between the control points of the polygons:

$$d(C_s, C_{\hat{s}}) \approx (s-\hat{s})^T(s-\hat{s}) \tag{4.26}$$

4.4.5 Properties of the Shape Space Spanned

In general, the number of samples needed to obtain reliable statistics increases rapidly with the dimension of the input data[10, 9]. Each of the training shapes can be seen as a vector embedded in a $2n$-dimensional space (where n is the number of points of each skull model trained). The space spanned by that set of shapes has three main properties. First, it is possible to focus in the low-dimensional subspace defined by the training data. The complexity is reduced to deal with the examples acquired in the training set while maintaining a mechanism to globally capture the shape parameters. Second it is possible to assign probabilities to data even in orthogonal directions to the subspace spanned by the training data. This second property allows us to adapt the probability distribution defined by the training set to make predictions of possible probability measures for objects not belonging to the training set but with similar shape features. Third, as long as the number of samples increases, it is expected to have more reliable estimates of the mean and covariance matrix.

4.4.6 Incorporating Invariance to the Shape

The minimization of the shape functional E_{shape} of the aligned and centered shape $\hat{s}$ is obtained by deriving the shape term 4.24 with respect to the shape s using the chain rule:

$$\frac{dE_{shape}(\hat{s})}{ds} = \frac{dE_{shape}(\hat{s})}{d\hat{s}} \cdot \frac{d\hat{s}}{ds} = \frac{dE_{shape}(\hat{s})}{d\hat{s}} \cdot \frac{d\hat{s}}{ds_c} \cdot \frac{ds_c}{ds} \tag{4.27}$$

Each component is solved separately. From equation (4.24) and applying the product rule of a derivative:

$$\frac{dE_{shape}(\hat{s})}{d\hat{s}} = (\Sigma_{\perp}^{-1}(s-\mu))^T \tag{4.28}$$

This term represents the gradient of the original shape energy E_{shape} evaluated for the aligned shape $\hat{s}$. The centered shape term s_c is defined as a function of the shape s and obtained in the following way :

$$s_c = (I_{2n} - \frac{1}{n}T) \cdot s \tag{4.29}$$

where n is the number of control points, I_{2n} denotes the identity matrix of size $2n$, and T is a $2n \times 2n$ matrix given by:

$$T = \begin{pmatrix} 1 & 0 & 1 & 0 & \dots \\ 0 & 1 & 0 & 1 & \dots \\ 1 & 0 & 1 & 0 & \dots \\ \vdots & \vdots & \vdots & \vdots & \ddots \end{pmatrix} \tag{4.30}$$

To obtain an aligned shape $\hat{s}$ as a function of the centered shape s_c the following expression has to be evaluated:

$$\hat{s} = \frac{Ms_c}{|Ms_c|} \tag{4.31}$$

with:

$$M = I_n \otimes \begin{pmatrix} \mu^t s_c & -\mu^t \times s_c \\ \mu^t \times s_c & \mu^t s_c \end{pmatrix} \tag{4.32}$$

Again, I_{2n} is the identity matrix with $2n$ rows and $\otimes$ is the Kroenecker product of matrices. In the 2-dimensional case, for the second term of equation 4.27 derived with respect to s :

$$\frac{ds_c}{ds} = (I_{2n} - \frac{1}{n}T) \tag{4.33}$$

This term represents the change of the centered shape s_c with respect to the input shape s.

In 2D, the last term of equation 4.27 is $\frac{d\hat{s}}{ds_c}$ which accounts for the influence of changes in the centered shape s_c onto the aligned shape $\hat{s}$. This term is obtained with the following equation:

$$\frac{d\hat{s}}{ds_c} = \frac{M's_c + M}{\|Ms_c\|} - \frac{(Ms_c)(Ms_c)^t(M's_c)}{\|Ms_c\|^3} \tag{4.34}$$

where M is the matrix defined in equation 4.32 and M' denotes the tensor of rank 3 given by:

$$M' = \frac{dM}{ds_c} \tag{4.35}$$

An algorithmic construction for evaluating M' can be consulted in [27]. The minimisation of the energy term $\gamma E_{shape}(M)$ presented in equation 4.12 is then solved by evaluating 4.27 with the expressions 4.28, 4.33 and 4.34 deduced.

4.5 Results

To test the algorithm, two groups of experiments have been designed: experiments with synthetic images and experiments with real images. The first group uses designed binary images which are synthetic images created with simple geometric objects. This design facilitates comparisons between the expected results and the outcomes of the segmentation approach. For the second category, the experiments were carried out with MRI images from the VHP male dataset [89, 4]. These MRI images were selected from areas of the head with different levels of difficulty in segmenting the skull. The training shape procedure is similar for both groups of experiments and is described in the following subsection.

4.5.1 Training set creation

In all the experiments, the training set consists of six object shapes, which are in turn made up of a fixed number of sampled points taken along the object's perimeter at equal distances from each other. This number of control points is 40 for synthetic images and 80 for real images. Figure 4.5 shows an example of the training shapes acquired.

The trained shapes were acquired with a manual labelling process. The user is presented with an image containing one outline of one object. As the initial step, the user selects with the mouse a number of points on the object contour. The shape of the object is reconstructed from these points by means of a quadratic B-spline interpolation. The resulting curve is resampled and the control points are stored in the same order and number for each shape. This process is repeated six times for each object. The object outlines labelled were one ellipse and one rectangle for the experiment with synthetic images, and two anatomical contours for the experiment with real images. In the case of experiments with real images, since there is only one image for each anatomical region, the training process consists of manually labelling the skull area in the CT image (equivalent to the MR image to be segmented). Even though it seems like a lot of work for the synthetic images, the manual segmentation is useful to simulate the variation of the shape distribution. For real images there may be tens or hundreds of images to segment having similar shaped regions, and labelling just six is worthwhile if it gives better results for the rest of the images. Better yet, the results for the rest can then be fed back into the statistical model to improve it.

4.5.2 Synthetic images

Figure 4.6 presents the synthetic image designed for the experiment and figure 4.7 shows the results of the proposed algorithm applied to this image. Each row in figure 4.7 represents the outcomes of the algorithm for different values for the parameters introduced in equations 4.1 and 4.12. The parameter combination is presented in table 4.2. As expected, setting $\gamma = 0.0$ results in the whole contour of the composed object being detected as illustrated in first row of figure 4.7. The second row of figure 4.7 shows a contour 'trapped' between the forces of the GVF term and the shape term. In this case, the contour converges to a "bad solution" with just some portion of the rectangular shape detected. In the third row, the shape term of the snake is high enough to deform the active contour

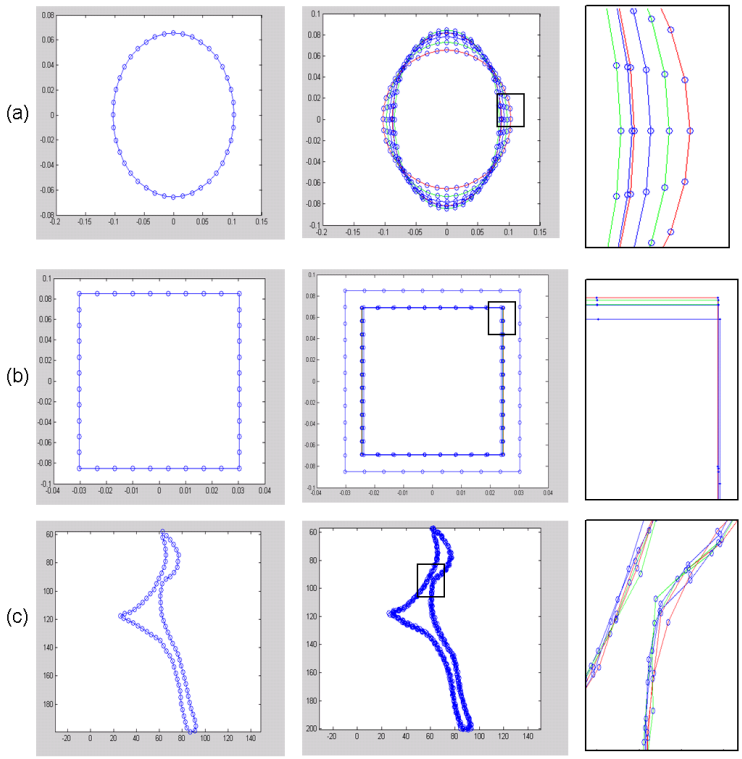

Figure 4.5: Examples of one element of each training set.(a) Ellipse with 40 control points. (b) Rectangle with 40 control points and (c) A portion of the skull represented with 80 control points. The first column shows one element of each training set. The second column shows the six shapes acquired for each object, and the third column shows a detail of the distribution of the control points in the squared area marked in the image of the second column.

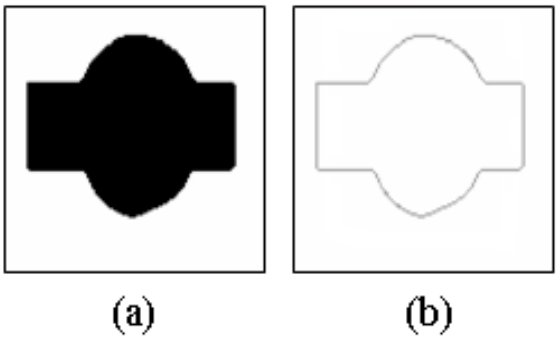

Figure 4.6: Synthetic image created with an ellipse and a rectangle overlapped to simulate occlusion (a) The object is represented with black pixel on a white backround. (b) The border of the image is represented with a gray-line.

towards the borders of the rectangular contour. Finally, the last two rows show an acceptable approximation to the objects of interest (i.e. a rectangle and an ellipse, respectively). It is important to remember that the shape of the object to be detected is given to the algorithm by the user (i.e. the training set in column 4 of table 4.2 is selected beforehand for the appropriate shape).

Row #	Shape term	Tension Rigidity	Trained shape
1	$\gamma = 0$	$\alpha = \beta = \mu = 0.5$	Rectangle
2	$\gamma = 10$	$\alpha = \beta = \mu = 0.5$	Rectangle
3	$\gamma = 80$	$\alpha = \beta = \mu = 0.5$	Rectangle
4	$\gamma = 100$	$\alpha = \beta = \mu = 0.5$	Rectangle
5	$\gamma = 100$	$\alpha = \beta = \mu = 0.5$	Ellipse

Table 4.2: Parameters for segmenting the image in figure 4.6(b) using a rectangular trained shape for rows 1-4, and an ellipse for the row 5

4.5.3 Real Images

The next experiment consists of segmenting the bone area shown in figure 4.1(b) including shape information. Figure 4.8 displays some results for different γ values. As in the case of synthetic images, if the γ value is increased, the shape information influences the outcome, resulting in a scheme directed by the shape. This will compensate for the missing information of bone components of high intensity in the MR image. A very high value of γ will direct the resulting contour to a shape configuration within the distribution of trained shapes. As can be seen in this figure the result of setting a low shape term gives a "poor segmentation" with respect to the expected object because of the high variability of pixel intensities in bone regions.

For this region, the average error between the correct segmentation and the final active contour obtained from the MRI segmentation is $\bar{e} = 1.97$ pixels (or 0.8mm in real values) with a standard deviation $\sigma = 0.87$ pixels using $\gamma = 4 \times 10^7$ and $\alpha = \beta = \mu = 0.5$. At this stage the γ parameter values were not normalised and represent the sum of the

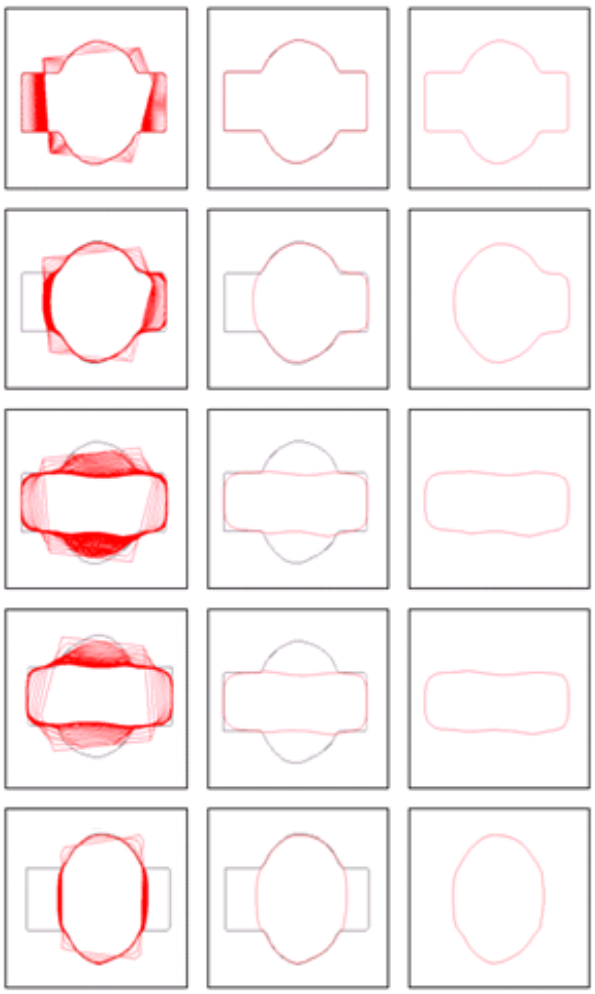

Figure 4.7: Extracting one object from the image in figure 4.6(b). Table 4.2 gives the parameters used for each row. The first column displays the active contour evolution at each iteration (red lines) overlaid on the feature map (gray pixels). The central column shows a comparison between the final state of the snake and the feature map (gray line). The rightmost column of this figure displays the resulting detected contour.

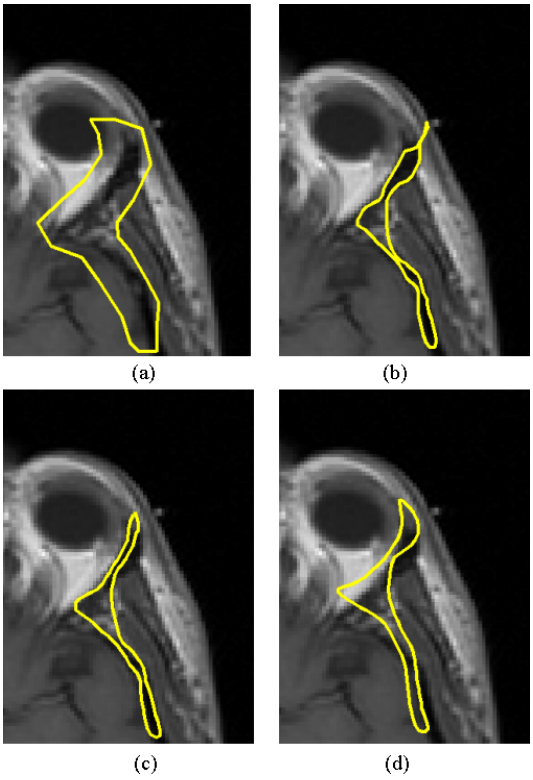

Figure 4.8: Results of the MRI segmentation for different shape parameters. (a) Initialization. Result for: (b) $\gamma = 1 \times 10^7$ (c) $\gamma = 2 \times 10^7$ and (d) $\gamma = 5 \times 10^7$

displacements of the shape energy term E_{shape}[2]. This error rate is calculated by averaging the distances between the control points from the CT segmentation and the control points from the resulting MRI segmentation and assuming that the CT segmentation represents the correct skull shape at the correct position in the volume.

Figure 4.9 shows the result of assembling, by means of a 3D interpolation with Radial Basis Functions [14], the points of several contours extracted with the algorithm proposed. The image illustrates the results for the upper half of the head for two situations: without shape included and with the shape term included. Figure 4.10 presents the skull model obtained with a CT segmentation used for the evaluation.

Figure 4.11 shows colored models which represent the distance between the two models in figure 4.9 and the correct model (shown in figure 4.10) of the same region. In the case of the pure image driven algorithm the average error is $\bar{e} = 2.70$ mm with $\sigma = 7.47$ mm and for the case of the shape driven approach the error rate is $\bar{e} = 2.1$ mm with $\sigma = 6.9$ mm. These rates were calculated using a geometric distance between the 3D surface models [31] [78] using $\gamma = 4 \times 10^7$ and $\alpha = \beta = \mu = 0.5$.

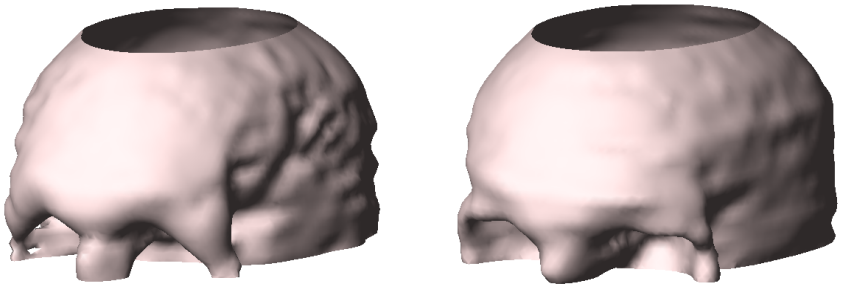

Figure 4.9: Results of segmenting the shape without shape term included (left) and with a shape term included (right). These models were created by a RBF surface interpolation process.

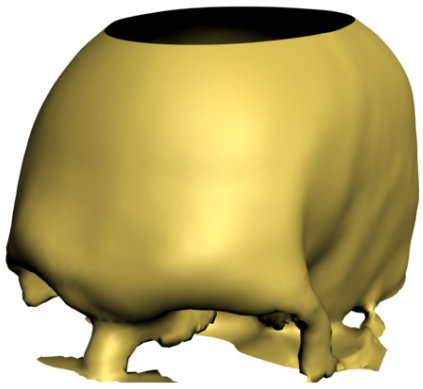

Figure 4.10: Portion of the skull segmented from the CT scans. This model was generated by joining all the contours of the skull by means of a RBF surface interpolant.

[2]In the 3D extension of the algorithm presented in next chapter the γ values are normalised using $max(\gamma)$ as a unit.

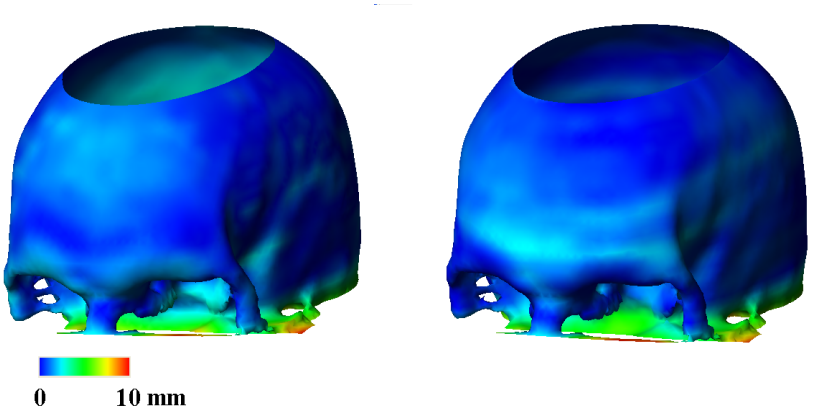

Figure 4.11: Visual comparison between the results of the segmenation approach without (left) and with (right) shape term and the skull segmented with CT scans. The area where the skull topology becomes more complex makes the control of the snake evolution more difficult causing more error as shown in the lower part of the models.

4.6 Discussion

The presented integration offers a number of advantages over other methods. With respect to the image feature aspect, the forces used to guide the active contour can be calculated by means of a vector field with a potential. The algorithm presented in this section uses a static potential that is calculated only one time at the beginning of the process in contrast to other techniques that use a dynamic approach (e.g. [72]). This is an advantage for future implementations because the algorithm can be parallelised. A second advantage of the algorithm is that the gradient information can be exploited in regions where the contour is clearly defined by the gradient profile and the shape information is used to guide the contour evolution in areas where it is not possible to establish a clear border (e.g. in regions where the pixel intensity values fail to distinguish between skull and air). Additionally, the gradient vector flow potential increases the range of capture (which is the region of influence of an object's edge on the active contour) allowing the evolution of the active contour through concave regions, especially when two edges of the object contour are relatively near to each other. In other gradient based approaches, this situation stops the contour evolution process.

The results obtained from this 2D approach are acceptable for areas of the skull where no important changes in topology are present, as at the top of the head. The regularity and smoothness of this area allows easy definition of the expected shapes for training purposes. Also, it facilitates the training and initialisation stages of the algorithm.

Even though acceptable results can be obtained with this approach for the top of the head, things become complicated for training and initialisation stages in areas of the head where discontinuities are present and more than one closed contour has to be segmented (as is the case for the front of the skull in the area of the eye sockets). To overcome these problems it is necessary to partition the skull surface to correctly initialise and train specific areas of the skull external surface. This increases the complexity of the training process. Also, in this initial implementation, the results of the algorithm are highly sensitive to the initialization step. Good initializations in general lead to acceptable results but a failure in the initialisation stage could lead to unacceptable results.

A more robust technique needs to be defined in order to benefit from the 3D information supplied by the volume. This is the subject of the next chapter.

Chapter 5

Skull Extraction in MRI data using a 3D Template-based Approach

In this chapter, a probabilistic method to approximate a 3D skull model from a MRI volume of the head is presented. The method uses a deformable model which iteratively adjusts its shape to fit the skull embedded in a MRI volume. Shape changes in the deformable model are defined combining two elements: information provided by the MRI volume and knowledge about the 3D structure of a skull shape. The influence of these two components in the deformable model evolution, as introduced in chapter 4, is modelled as a Bayesian energy formulation $E(M) = E_{volume}(f, V) + \gamma E_{shape}(M)$, where E is the energy provided by the deformable model M, V is the MRI volume, f is the set of features associated to the volume, E_{volume} is an energy function of the features and E_{shape} is the energy contribution of the shape.

The skull extraction method presented in this chapter is built on the results of the 2D approach presented in chapter 4. This 3-dimensional formulation ameliorates the principal limitations found in the 2-dimensional approach:

- It reduces the problems of the initialisation of the deformable model (sensitivity problems),
- It avoids the requirement of training specific deformable models for different parts of the skull, and
- It reduces the time for creating the training set by means of a semi-automatic approach for collecting the skull examples and their shape parameters.

The main issues to be addressed in the 3D skull extraction process are summarised in table 5.1. Depending on their influence in the deformable model evolution, these issues can be grouped in two categories: issues related to volume features and issues related to shape control.

Regarding volume features, a process for feature extraction is required to analyse regions of the volume containing skull information. Additionally, a method for defining the influence of the extracted features on the deformable model is required. With respect to the shape control aspect it is necessary to:

- Define a representation for the structure of the 3D deformable model.

Issue	Solution Method
Combining volume features and skull shape knowledge	Bayesian approach extended to 3D
Defining volume features and their influence in the deformable model evolution	Energy minimisation for a 3D deformable model
Defining shape representation, shape metrics and shape evolution restrictions	3D Mesh with control points, metrics, shape representation and invariance
Knowledge representation of the skull shape	Gaussian model of skull shapes
Including invariance in the representation	Invariance formulation

Table 5.1: Issues to be addressed in the 3D skull extraction process

- Establish a scheme to represent the shape of the deformable model.
- Define the mechanisms to deal with the variation of shapes for different skull models.
- Establish a metric to compare the models involved.
- Define the way in which the volume features and the shape restrictions will be combined to drive the evolution of the deformation model.

Each of these issues will be discussed in detail in the remainder of the chapter which is organised as follows: Section 5.1 presents an overview of the 3D skull extraction technique considering the main processes involved. Section 5.2 presents in detail the skull extraction process extended to the 3-dimensional case. Section 5.3 describes a series of tests that were conducted to validate the behaviour of the algorithm under different parameter settings. Section 5.4 presents the results of the skull extraction process.

5.1 Overview of the 3D Skull Extraction process

In the 3D skull extraction process, volume features are combined with shape restrictions to produce a 3D skull model that best fits the skull data provided by the MRI. This process can be considered as a bootstrapping technique in which, starting from an approximation of the skull (noisy volume), the aim is to build better approximations of that skull iteratively by means of deforming a skull template. In this document the terms skull template and deformable model will be used interchangeably.

The set of features, defining possible skull borders in the dataset, are used to define a force for attracting the vertices of the deformable model towards the borders of the skull. At the same time the shape term acts by maintaining the structure of the deformable model within the limits of a skull shape. The knowledge of the skull shape is determined from the analysis of a set of skull examples called the training set.

Several modules are needed to implement the volume processing tasks and the shape restrictions in the skull extraction process. Figure 5.1 shows the main stages involved. The pre-processing and statistical processing modules work together with the 3D segmentation

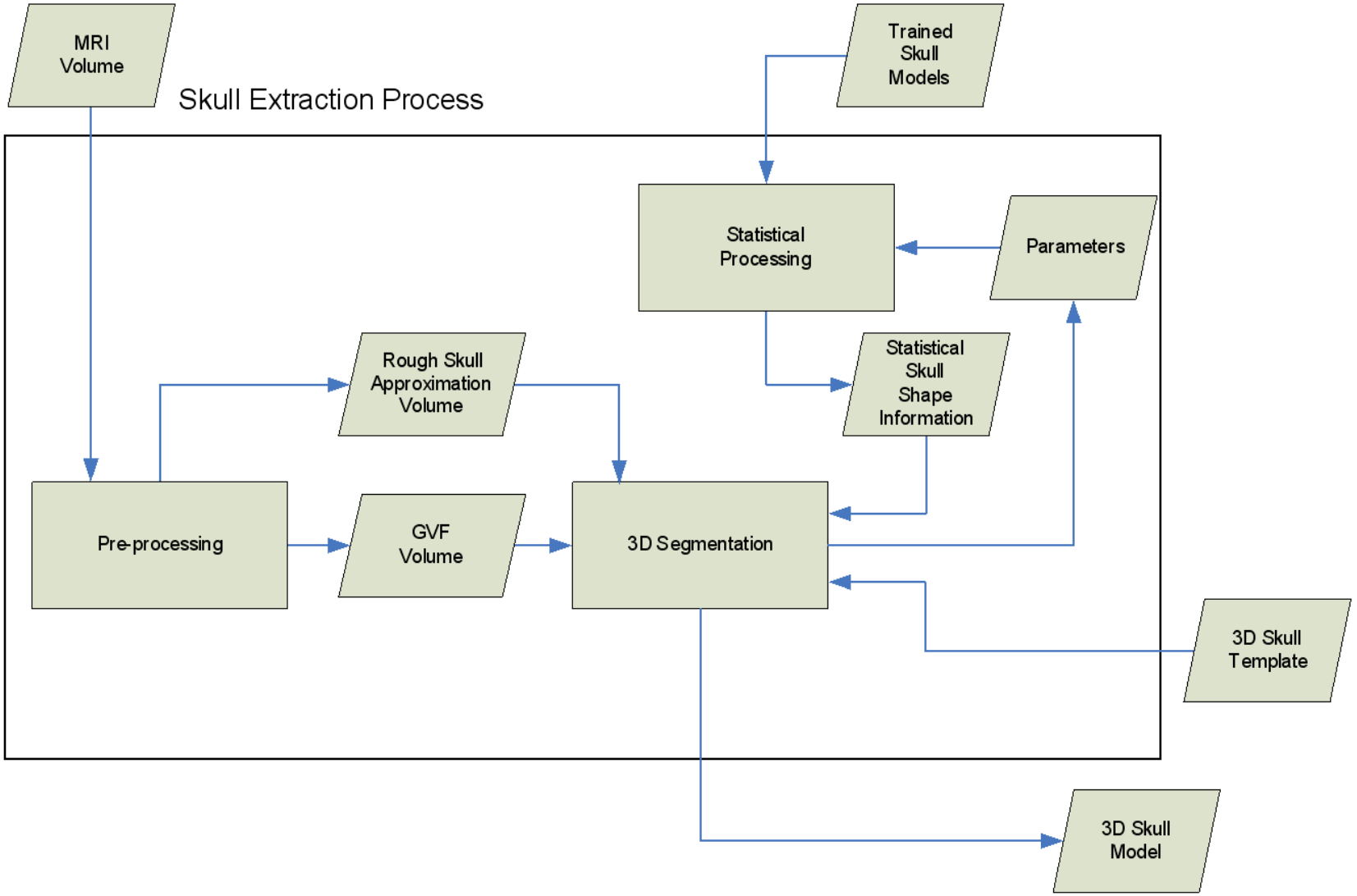

Figure 5.1. Components of the skull extraction process

module in an iterative algorithm to produce a 3D skull model. These modules are described in detail in the following subsections.

5.2 Pre-Processing

The pre-processing module receives as input the initial MRI volume and produces as output an approximation of the skull volume and a vector field associated with that approximation. Figure 5.2 shows an example of the volume produced by the pre-processing module. The initial skull approximation is used to estimate the position, orientation and global proportions of the skull to extract. It is also, is used to limit the searching space for reducing the number of steps required for the extraction algorithm to find a solution. The vector field produced is used to define the forces at each point of the space that will attract the vertices of the deformable model towards the skull borders.

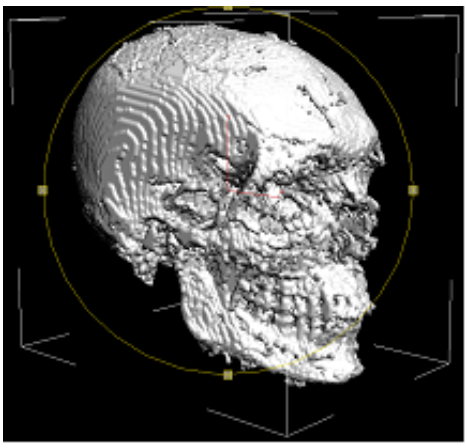

Figure 5.2: Noisy skull approximation. Result of the region-growing algorithm for the entire MRI volume after isosurface processing.

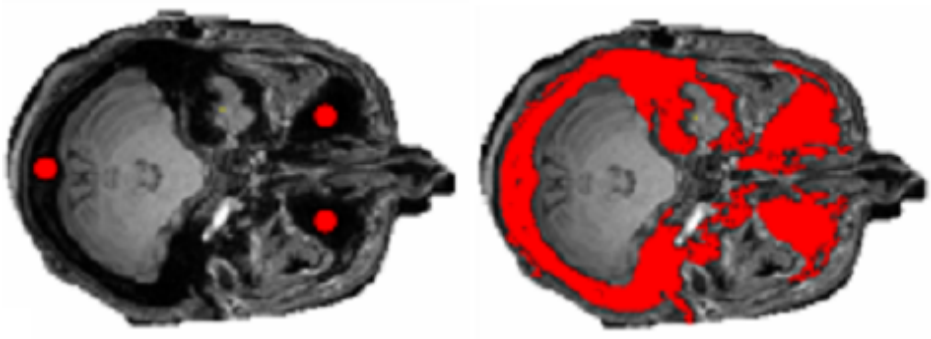

Figure 5.3: Results of the multi-seed region growing algorithm.(Left) three seeds selected by the user with red dots. (Right) the area of the image segmented by applying the region growing algorithm which groups pixel neighbours with similar intensities.

For producing a skull approximation, a set of seeds is chosen by a user based on an intuitive knowledge about the skull shape. Figure 5.3 shows the process for a 2D slice of a

single MRI dataset. The user selects areas of an image with low intensity pixels that are probable skull regions. Then, a multi-seed region growing algorithm is applied for each seed taking into account similarity of pixel intensities and neighbour connectivity with previous and subsequent slices. The information of several slices is merged and a volume is created. The result is a binary volume in which probable skull voxels have a value of 1 and the rest of the voxels have a value of 0.

For an MRI volume the user requires to select on average 100 points (seeds) for creating the initial skull approximation. The multi-seed region-growing software implemented has the capability to modify the intensity used for grouping regions (to select seed neighbours), edit the selection and to show the 3D reconstruction of the regions selected, so that the user can make corrections when needed. Processing a volume takes in average one and a half hour of manual work. At this point, the accuracy of the resulting approximation is not so important. The statistics of the shape term will compensate for the error during the algorithm execution: missing information will be completed and extra information eliminated.

The volumetric field associated with the skull approximation is defined as a function of the gradient of the initial skull volume produced. The gradient vector flow is a potential force $v(x)$ calculated in terms of the gradient and defined at each point of the volume x. This vector field is calculated in order to define a series of attracting forces acting on the deformable model and originated from volume features. For this purpose, an n-dimensional formulation for a GVF for the field $v(x)$ is applied which is defined by the equilibrium solution for the vector diffusion equation [114]:

$$u_t = g(\mid \bigtriangledown f \mid) \bigtriangledown^2 u - h(\mid \bigtriangledown f \mid)(u - \bigtriangledown f) \tag{5.1a}$$

$$u(x, 0) = \bigtriangledown f(x) \tag{5.1b}$$

In equation 5.1a, the term on the right $h(\mid \bigtriangledown f \mid)$ is referred to as the smoothing term since this will produce a smoothly varying vector field. The second term, $(u - \bigtriangledown f)$, is referred as the data term since it encourages the vector field u to be close to $\bigtriangledown f$ computed from the data. The weighting functions g and h apply to the smoothing and data terms, respectively. Since these weighting functions are dependent on the gradient of the edge map, the weights themselves are spatially varying. Applying the same criteria used for the 2D implementation the weighting factors chosen are [113]:

$$g(\bigtriangledown f) = \mu \tag{5.2a}$$

$$h(\bigtriangledown f) = \mid \bigtriangledown f \mid^2 \tag{5.2b}$$

The term $v(x)$ defines a direction vector for each point in the space $x = (x_i, y_i, z_i)$. These vectors point towards the border of the skull. In fact, 3-D GVF has an identical structure to the 2-D GVF formulation described in Eq. 4.8 since it is written in a dimension independent form.

5.3 Statistical Processing

The statistical processing module covers all the aspects related to the skull shape formulation. In this section, three main aspects required to integrate the shape knolwedge for controlling the evolution of a deformable model are presented. First, the representation of the structure of the deformable model is covered. Second, the definition of the shape

representation for the deformable model and the mechanisms to make this representation invariant are described. Third, the method to gather information for acquiring skull shape knowledge is described. Additionally, the way that this skull shape knowledge is applied to the deformable model evolution is also presented.

5.3.1 Deformable Model and Shape Representation in 3D

There are two main aspects to be covered in this section: the representation of the the deformable model and the representation of its shape. In this context, we will refer to the shape of an object as the set of geometric properties that are maintained between objects of the same type (i.e. skulls) independent of position, size and orientation. For this particular work, an explicit model of a skull in the form of a triangle mesh is used as the deformable model. A triangle mesh M is a pair of sets $(\mathbf{V}, \mathbf{T})$, where $\mathbf{V}$ is a set of vertices $\mathbf{v} \in \mathbb{R}^{\mathbf{3}}$, $\mathbf{T}$ is a set of triplets of edges, $\mathbf{T} \subseteq \{(u, v, w) \mid u, v, w \in \mathbf{E} \wedge u \neq v \neq w\}$, defining triangular polygons, and $\mathbf{E}$ is a set of edges between vertices, $\mathbf{E} \subseteq \{(s, t) \mid s, t \in \mathbf{V} \wedge s \neq t\}$. The union of all the triangles $\bigcup_{i=1}^{k} \mathbf{t_i} \in \mathbf{T}$ defines a continuous closed surface $S(M)$.

The shape of the deformable model M is defined as a set of N 3-dimensional control points defining the shape of the triangle mesh M. The control points set is a subset of the vertices of the model $\mathbf{V}$. Each control point influences the spatial positions of the neighour vertices. For simplicity, the shape will be represented as a vector s with the following structure:

$$s = (x_1, y_1, z_1 ..., x_N, y_N, z_N)^T \tag{5.3}$$

with x_i, y_i, z_i being the coordinates of each control point. The number N of control points used in our implementation is $N = 3000$ due to computational restrictions in the implementation[1].

The method to represent the shape knowledge is based on a characterisation of the control point sets by means of a multivariate Gaussian distribution. The distribution is used for modelling the variation in position of each control point of all the shape examples of the training set. The expression for this probability distribution is given by:

$$\rho(s) \propto \exp(-\frac{1}{2}(s - \mu)^T \Sigma_{\perp}^{-1}(s - \mu)),$$

where μ is the average of the training set and $\Sigma_{\perp}$ is the covariance matrix of the training set. Under this convention, the energy of the deformable model M can be expressed in terms of its shape descriptor s by means of the following energy term E_{shape}:

$$E_{shape}(s) = \log(\rho(s)) + const = -\frac{1}{2}(s - \mu)^T \Sigma_{\perp}^{-1}(s - \mu) \tag{5.4}$$

As in the 2-dimensional case, in our 3-dimensional implementation the distance between two deformable models M_s and $M_{\hat{s}}$ is calculated by means of an approximation to a Mahalanobis distance using a simple Euclidean distance d between the sets of control points (as presented in section 4.4.4).

[1] The current Matlab implementation is limited by the size of the matrices involved for the computations.

5.3.2 Alignment of training shapes

An optimal alignment of two shapes s and $\hat{s}$ with respect of rotations, translation and scaling (known as full Procrustes fit) requires to minimise the distance:

$$D^2(s,\hat{s}) = \parallel \hat{s} - \beta s\Gamma - 1_k\gamma^T \parallel^2 \tag{5.5}$$

where D is the distance between the two shapes, $\beta >= 0$ is a scaling factor, Γ is a matrix accounting for rotations, and γ a vector accounting for translations. Setting corresponding derivatives to zero, the solution for the optimal parameters $\hat{\beta}$, $\hat{\gamma}$, and $\hat{\Gamma}$ are the following expressions [47], [86] and [35]:

$$\hat{\gamma} = 0 \tag{5.6}$$
$$\hat{\Gamma} = UV^T \tag{5.7}$$

The rotation term $\hat{\Gamma}$ is given in terms of the matrices derived from a single value decomposition of the matrix product $\frac{\hat{s}^T s}{\|s\|\|\hat{s}\|}$ as follows:

$$\frac{\hat{s}^T s}{\parallel s \parallel\parallel \hat{s} \parallel} = V\Lambda U^T \tag{5.8}$$

The rotation estimator derived is:

$$\hat{\beta} = \frac{trace(\hat{s}^T s\hat{\Gamma})}{trace(s^T s)} \tag{5.9}$$

and finally, the expression for $\hat{s}$ is:

$$\hat{s} = \hat{\beta} s_c\hat{\Gamma} + 1_k\hat{\gamma}^T + \sqrt{D^2(s_c,\hat{s})} \tag{5.10}$$

Given a set of m training vectors $\chi = \{s_i\}_{i=1..m}$ which are centered and normalised, there are several ways to align them [35], [47]. In this research, we align them with respect to the Procrustes estimate of the mean vector which is defined as:

$$\hat{\mu} = \arg \inf_{\mu:S(\mu)=1} \sum_{i=1}^{n} \sin^2 \rho(s_i,\mu) = \arg \inf_{\mu:S(\mu)=1} \sum_{i=1}^{n} \hat{D}^2(s_i,\mu)$$

the point in shape space corresponding to the arithmetic mean of the Procrustes fits,

$$\bar{s} = \frac{1}{n}\sum_{i=1}^{n} s_i^P \tag{5.11}$$

has the same shape as the full Procrustes mean [35].

5.3.3 Training of the 3D Skull Shapes

Figure 5.4 shows an example of a training set of points created from skull sampled points at the top of the skull for individuals 03, 04, 06, 09, 10 and 14 of the UOS dataset.

The initial training shapes used were the Visible Human Project (VHP) male dataset [4] and a commercial synthetic skull model[2]. The synthetic model is shown in figure

[2] web site: http://www.turbosquid.com/FullPreview/Index.cfm/ID/248625

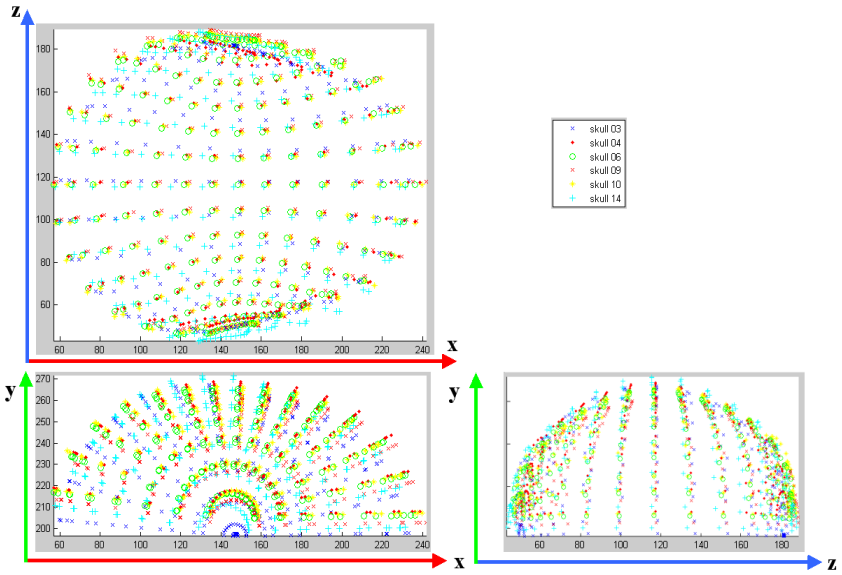

Figure 5.4: example of a training set of points created from skull sampled points at the top of the skull for individuals 03, 04, 06, 09, 10 and 14 of the UOS dataset

5.6. At this point, the only requirement for the synthetic skull template was to have the most important anatomic features located in the right place. The skull model of the VHP was created from the CT data. The VHP skull model is a precise anatomically correct model of the skull. In contrast, the synthetic model is not anatomically correct. Even though the second model is not anatomically correct, both models contain the most important geometric features that we wanted to model (i.e. the frontal area of the skull). Additionally, and in order to add some shape variability to the training set, 5 skull models were created from rough approximations of the set of skulls to segment and added to the training set. The process for generating these 5 models was the following: The 60 noisy skull volumes generated at the pre-processing stage were registered with the commercial skull model using a non-rigid registration algorithm. The algorithm will be described later in section 5.4.2. As a result, 60 rough approximations of the skull volumes were generated. A principal component analysis (PCA) was applied to the vertices of each model. With the PCA analysis it is possible to reconstruct any skull model from the set by means of a linear combination of the average skull and a set of coefficients (the principal components of each particular model). The first 17 coefficients containing more than 95% of the variability were chosen. Finally a K-means clustering analysis with 5 centres was applied to the PCA coefficients of the 60 skulls. The average coefficients of each cluster were used to reconstruct each of the synthetic skulls. With this procedure, 5 skull models containing most of the shape variation in the set of skulls to segment were created.

5.3.4 Invariance of the Shape Term in 3D

The definition of an invariable representation becomes a key aspect in order to compare and assess shape properties of different skulls. The shape of the deformable model s is the input to the energy functional E_{shape} (equation 5.12). As explained in chapter 4, the aim of this functional is to determine the similarity between the input shape s and the family

of shapes defined by the training set of skull shapes. In order to make this formulation invariant, the input shape and the training shapes have to be defined in the same system of reference (i.e. normalised and aligned). Since the training shapes are aligned and normalised with respect to the mean shape $\bar{s}$, the argument of the energy term (equation 5.4) must be also aligned. The energy for the aligned and centered shape $\hat{s}$ is:

$$E_{shape}(\hat{s}) = -\frac{1}{2}(\hat{s}-\mu)^T\Sigma_{\perp}^{-1}(\hat{s}-\mu) \tag{5.12}$$

with $\hat{s}$ as defined in equation 5.10. The translation of the shape s is eliminated by:

$$s_c = (I_{3n} - \frac{1}{n}\Gamma)s$$

with:

$$\Gamma = \begin{pmatrix} 1 & 0 & 0 & 1 & 0 & 0 & \cdots \\ 0 & 1 & 0 & 0 & 1 & 0 & \cdots \\ 0 & 0 & 1 & 0 & 0 & 1 & \cdots \\ 1 & 0 & 0 & 1 & 0 & 0 & \cdots \\ \vdots & \vdots & \vdots & \vdots & \vdots & \vdots & \ddots \end{pmatrix} \tag{5.13}$$

Essentially S_c represents an origin centered shape. The energy term E_{shape} can be minimised with respect to the aligned shape $\hat{s}$ by means of evaluating $\frac{dE_{shape}(s)}{ds}$ using the chain rule with the following expression:

$$\frac{ds}{dt} = -\frac{dE_{shape}(s)}{ds} = -\frac{dE_{shape}(\hat{s})}{d\hat{s}} \cdot \frac{d\hat{s}}{ds_c} \cdot \frac{ds_c}{ds} \tag{5.14}$$

with:

$$\frac{dE_{shape}(\hat{s})}{d\hat{s}} = (\Sigma_{\perp}^{-1}(s-\mu))^T \tag{5.15}$$

$$\frac{ds_c}{ds} = (I_{3n} - \frac{1}{n}\Gamma) \tag{5.16}$$

$$\frac{d\hat{s}}{ds_c} = \frac{d(\hat{\beta}s_c\hat{\Gamma} + 1_k\hat{\gamma}^T + \sqrt{D^2(s_c,\hat{s})})}{ds_c} \tag{5.17}$$

Note that the terms D, $\hat{\gamma}$, $\hat{\Gamma}$, and $\hat{\beta}$ in equation 5.17 are all functions of the aligned shape $\hat{s}$ as expressed in equations 5.5-5.9. Equation 5.17 represents the expression that is used to obtain, by means of a minimisation, the nearest most probable shape of a configuration of control points in the 3D space. This is the key aspect to the 3D energy shape formulation. Equation 5.12 is used to evaluate the term $\gamma E_{shape}(M)$.

5.4 3D Segmentation

Figure 5.5 shows the main stages of the 3D segmentation module.

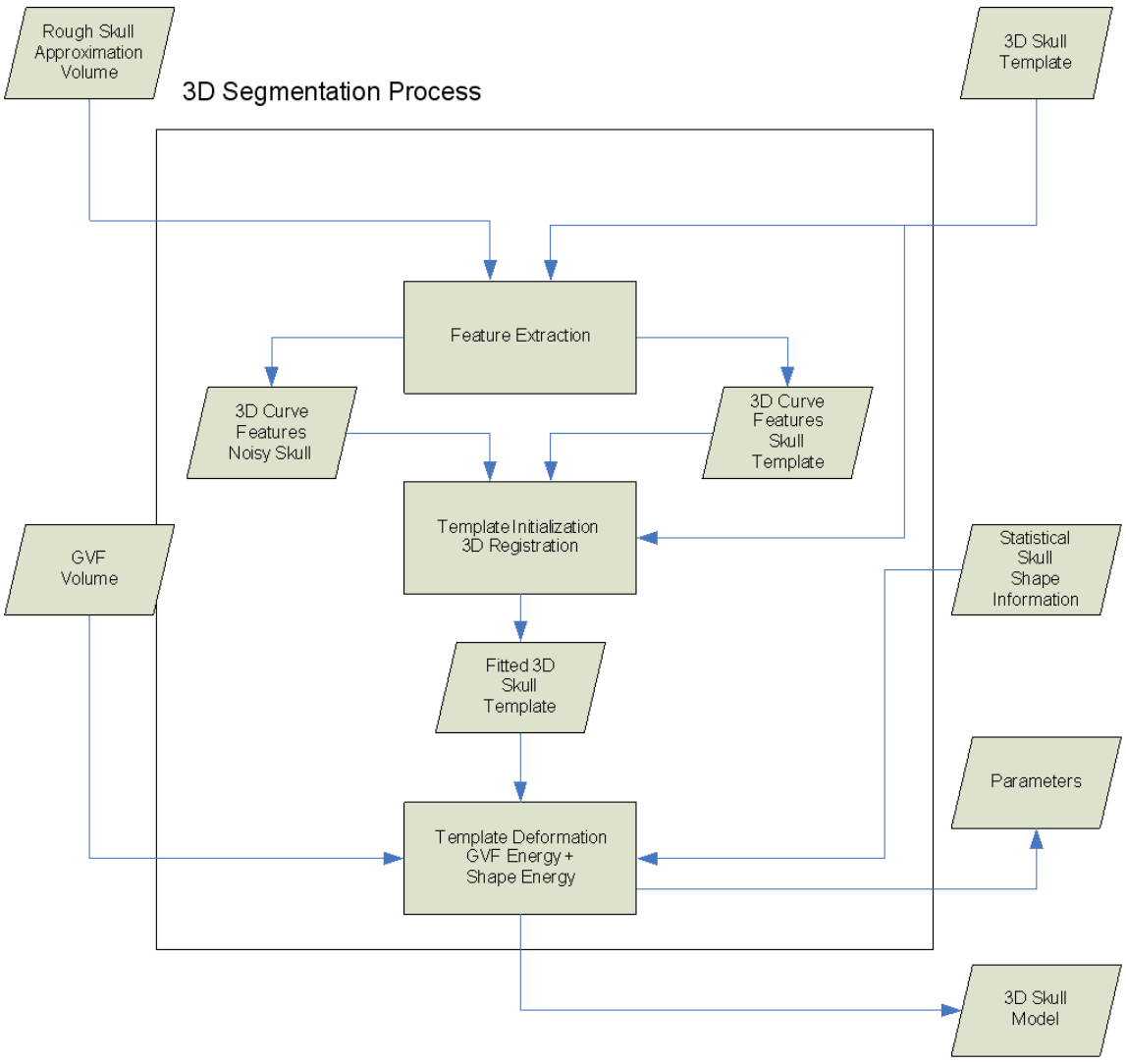

Figure 5.5: Elements of the 3D Segmentation process

5.4.1 The 3D Deformable Model

A skull template consisting of a surface made up of a triangle mesh with 18,546 vertices and 36,710 triangles is the starting point used for the 3D segmentation algorithm. The model is uniformly sampled by means of a KD-tree algorithm [108] and 3000 vertices of the mesh are selected to act as control points. The synthetic skull used as the template is a commercial 3D model[3] (see figure 5.6).

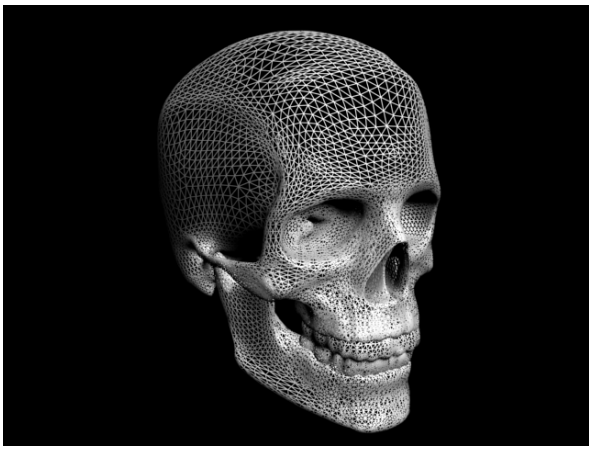

Figure 5.6: Skull template used for the deformation based surface reconstruction process.

5.4.2 Feature Extraction Module

The noisy initial volume and the deformation models are processed in similar ways. In the feature extraction module, a set of 3D features is identified in prominent areas of both. The surface of the noisy model is created by means of a marching cubes algorithm applied to the input noisy volume. In the noisy surface model, a user manually draws a number of surface curves in pre-defined areas of the skull. These are the borders of the eye cavities, the border of the nasal aperture, and the edges of the jaw. A similar set of curves is marked in the skull template model. These sets of curves will be matched in the template initialization module.

5.4.3 Template Initialization and 3D Registration Module

In the template initialisation module a pair of sets of 3D curves are used, one corresponding to the features of the noisy skull and the other to the features of the deformable model. These curves are matched by means of a point registration algorithm. The registration step reduces the problems of initialisation with the deformable model by making the initial template coincide with the volume of the noisy skull. In this research, the Robust Point Matching (RPM) [19, 20] is used for this purpose (see appendix F).

Usually in a registration process there are two problems to solve. First, the correspondence between the control points must be found. In general, the number of points of each matching set is different. Second, the transformation between the control points must be estimated. There are two types of transformation: rigid and non-rigid.

[3]Models web page: http://www.turbosquid.com/FullPreview/Index.cfm/ID/248625

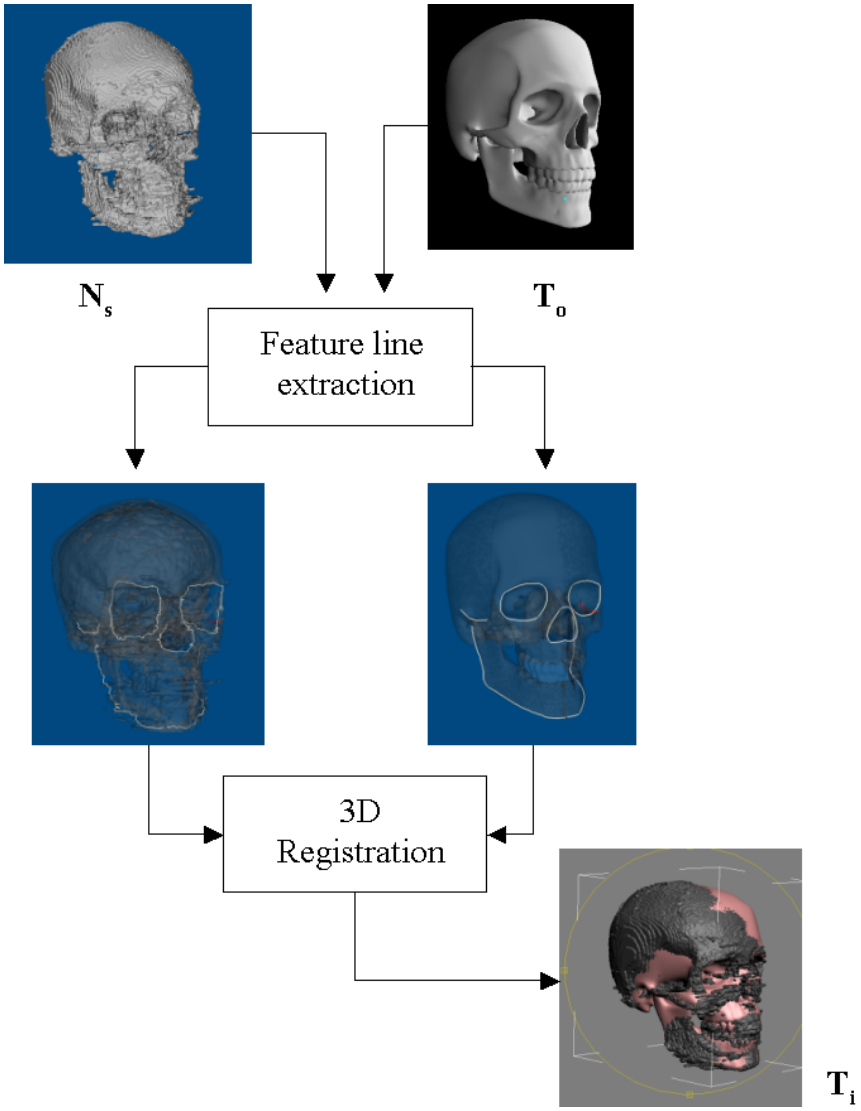

Figure 5.7: Feature lines are extracted from both the noisy pre-segmented skull N_s and the clean skull template T_o. This gives a set of correspondence features in the form of surface curves that can be registered to define the initial shape of the template. Based on this pair of features, a warping process is defined using the relation between the surface curves, resulting in the initial skull template T_i.

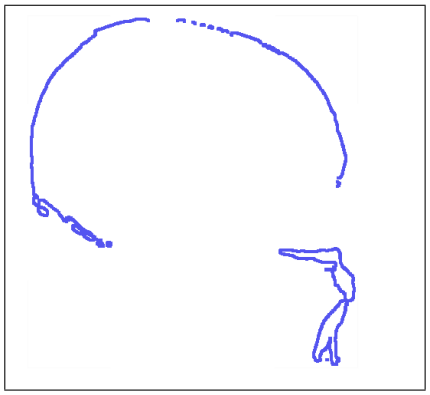

Figure 5.8: Example of a profile curve generated from intersecting a noisy skull model with a cutting plane.

In rigid transformations, the distance between any two coordinate locations remains unchanged by the transformation. In non-rigid transformation this restriction is not imposed, allowing more flexibility to the deformation. We are interested in the non-rigid type of transformation in order to obtain a template closest to the border of the volume of the noisy skull.

The Robust Point Matching method solves for both the correspondence and the transformation between two sets of points. The registration problem is much easier the non-rigid transformation is first estimated once the correspondence between points is given. Additionally, information about an approximate spatial transformation can be of considerable help in a search for the correspondence. This duality points to a natural way of solving the line matching problem. Appendix F, "Robust Point Matching Algorithm", describes the components of this registration technique.

For extracting the 3D curves the vrmesh 3D curve sketching tool is used [4]. A user is presented with an interface allowing drawing curves on the surface of a model. This tool has a 3D editor with the standard functions to manipulate triangular mesh such as zooming and rotation, which facilitates the manipulation of the models. The user has the option to draw a smooth open or closed curve on the surface by selecting a set of points on the surface and the curve is obtained by drawing a minimum length path curve interpolating the points and the triangles between them. The time required for generating a set of curves for a noisy skull model takes between 10 and 15min. Additional feature curves can be generated by intersecting the skull models with a cutting plane at the centre of the head. Figure 5.8 shows a profile curve obtained with this method.

After finding the spatial correspondence between the pair of 3D features the space surrounding the skull template is deformed in order to fit the noisy volume, preserving some of the spatial distribution of the model. A schematic diagram of the template initialisation is shown in figure 5.7.

5.5 Deformable Model Evolution

The skull template deformation algorithm is shown in figure 5.9. The corresponding data flow graph is presented in figure 5.10. The inputs of the algorithm are two 3D mesh

[4] see http://www.vrmesh.com/

models. The first model represents an initial noisy volume of the skull to segment. This model is generated as described in section 5.2 using an isosurfacing process on the MRI volume data. The second model is a skull template initialised as described in section 5.4.3. The algorithm deforms the skull template (deformable model) to find a skull model that best fits the information provided by the noisy skull volume. The deformation is conducted by changing the positions of a set of control points defined in the deformable model according to the image features found in the volume and the shape restrictions. The stop condition used in the algorithm is a fixed number of iterations (in our case 100). At each iteration, the deformable model control points are moved towards the direction of the most probable skull configuration. The number of iterations was chosen after running the algorithm several times and observing that changes in the deformable model control points after 60 iterations were small (less than 1.5mm in average) for the combination of parameters used.

The displacement of the control points is stored in three 1-dimensional vectors d_1, d_2 and d_3. Vectors d_1 and d_2 accounts for changes when volume features are taken into account. Vector d_1 has values when the deformable model is near to the noisy skull model. Vector d_2 stores the contribution of the Gradient Vector Flow when a control point is far from the noisy volume. Vector d_3 stores displacements originated by the shape term. Each of the vectors d_1, d_2 and d_3 has three components $d_1(x)$, $d_1(y)$ and $d_1(z)$ (one for each dimension).

At each step of the main loop and for each control point, the algorithm checks if the control point is close to a region of the noisy skull model. The search is made in the normal direction of the surface where the control point lies (i.e. normal to the deformable model surface). If the noisy volume lies within a radius of 5mm (that can be adjusted by the user) then d_1 is calculated (i.e. moving the control point in the direction of the noisy volume). The control point displacement is a fraction of the distance calculated. This makes the deformable model change slowly to maintain the mesh structure. Currently the value used for the displacement is set to 10% of the distance. If the control point is not near the noisy volume then the displacement vector d_2 is calculated using the values obtained of the GVF at that point.

With the information collected in vector d_1 and d_2, the skull template is deformed using a Radial basis function with thin plate spline base (RBF-TPS) approach. Each of the control points are moved to their new positions and the RBF-TPS calculated function is used to deform all the space surrounding the control points (i.e. deforms the skull template).

In the last step, after deforming the skull template, each control point is "corrected" by using the shape term. A new displacement vector d_3 is calculated and a new RBF-TPS deformation function is calculated and applied to the control points. The stop condition is evaluated, and if not finished then the algorithm returns to the main loop.

The output of the deformation template module, is a complete skull model fitted to the noisy data. There are several alternatives for defining the stop condition. One criterion is that that the sum of displacements calculated for the deformation vectors d_3 at each step of the algorithm are maintained under a given value for a fixed number of iterations. The second criteria is to define a fixed number of iterations for the deformation template algorithm. In this research work we used the second criteria.

Algorithm 1 Template Deformation

Require: Skull template properly initialised
  while (stop condition not met) **do**
    $Variable\ initialisation$:
    $i = d_j(x_i) = d_j(y_i) = d_j(z_i) \leftarrow 0$;
    $\{(i,j)|\ 1 \leq j \leq 3;\ 0 \leq i \leq Number\ of\ Control\ Points\}$
    for *each control point* i **do**
      calculate intersection of the ray from CP_i (at the skull template)
      to the noisy volume in its normal direction within a range
      if (intersection exists) **then**
        calculate $d_1(x_i), d_1(y_i), d_1(z_i)$ in direction of the intersecting point
        set $d_2(x_i) = d_2(y_i) = d_2(z_i) \leftarrow 0$
      else
        set $d_1(x_i) = d_1(y_i) = d_1(z_i) \leftarrow 0$
        calculate $d_2(x_i), d_2(y_i), d_2(z_i)$ from the GVF direction
      end if
    end for
    Deform the skull template with a RBF-TPS and
    $CP_i \rightarrow CP_i + d_1 + d_2$
    Update the CP_i control points
    Initialise $d_3(x_i), d_3(y_i), d_3(z_i) \leftarrow 0$
    Calculate the shape energy term
    Apply the shape term to the skull template using RBF-TPS with
    $CP_i \rightarrow CP_i + d_3$
    Update the CP_i control points
    Evaluate the stop condition
  end while

Figure 5.9: Template deformation algorithm.

5.6 Parameter Testing

The skull extraction formulation contains a weighted combination of a volume feature and shape terms controlling the evolution of the deformable model. For analysing the influence of these terms a set of combinations of their weights were tested. This section presents two main tests conducted on the parameters of the algorithm:

- With the first test we demonstrate the correctness of the shape term in taking an arbitrary configuration of the deformable model template for producing a final configuration with the correct shape proportions.
- In the second test, we show the capacity of the algorithm to use volume features and shape features in combination.

Two weighting factors are tested: the volume feature factor (VFF) affecting the influence of these features in the final result, and the shape factor (SF) which accounts for the restriction in shape form.

5.6.1 Notation used for the models

For the following set of tests, we will make reference to different states of the deformable model during the process of segmentation. The initial state of the skull template model will be denoted by the letter S (source model). This source model is deformed n times by the algorithm. The state of the model at the iteration j will be denoted by D_j for $j = \{1...n\}$. The deformed models D_j will be compared to a reference model R. The model R will be specified for each test.

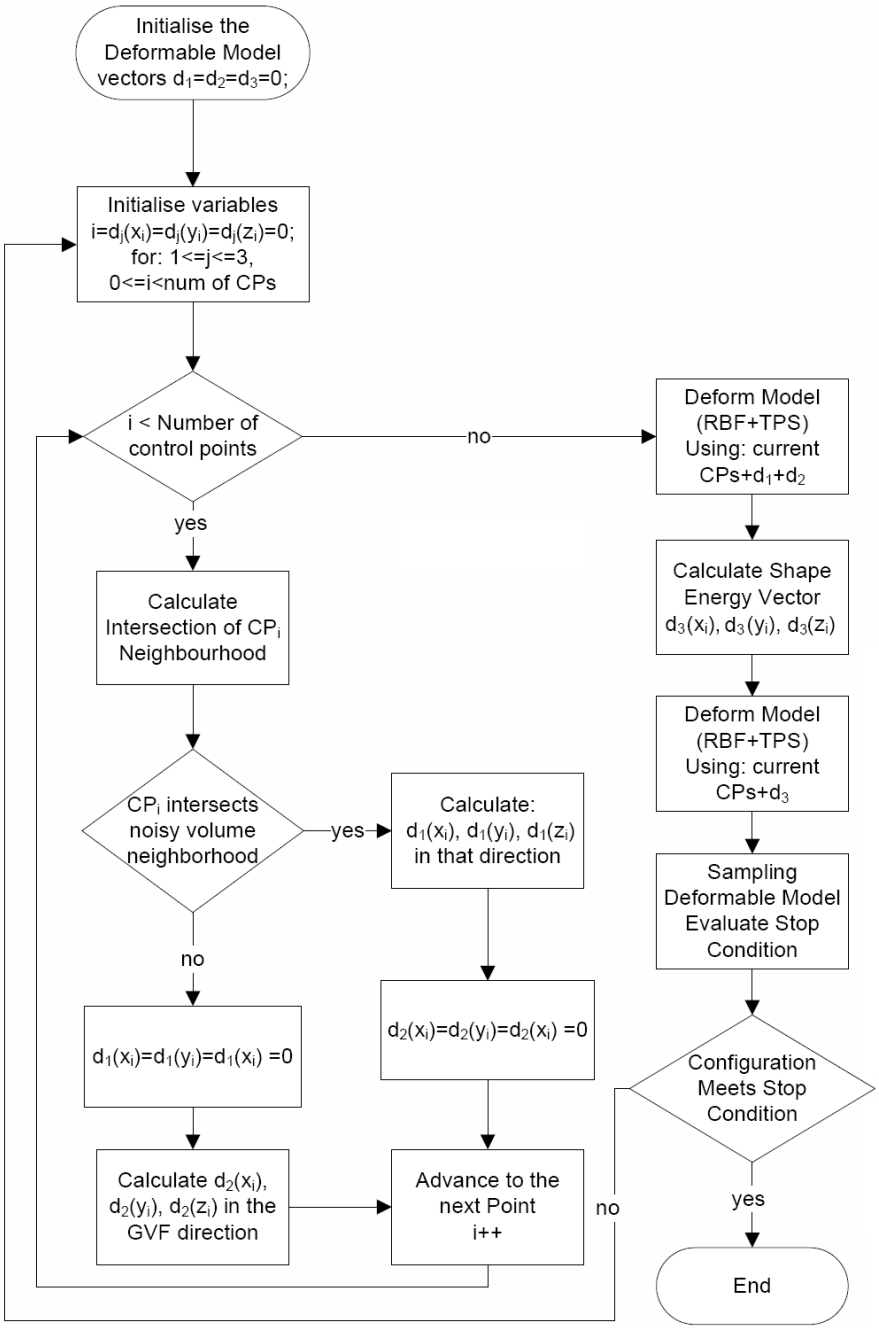

Figure 5.10: Flow Chart of the 3D segmentation algorithm.

5.6.2 Effect of the shape restrictions

To assess the results of the algorithms, a skull model was deformed manually using a free form deformation algorithm (FFD) [107]. Figure 5.11 shows the base model (left) and deformed model(right) used for this test. Figure 5.12 shows the difference in mm between the source and target models. The deformed model will be our source model S. S is processed using our algorithm with only the shape term acting on it. The objective is to recover the normal skull proportions of S. In order to have a comparison reference, a model R was created applying our shape recovering algorithm to S with a shape factor (SF) of 1.0 for 100 iterations.

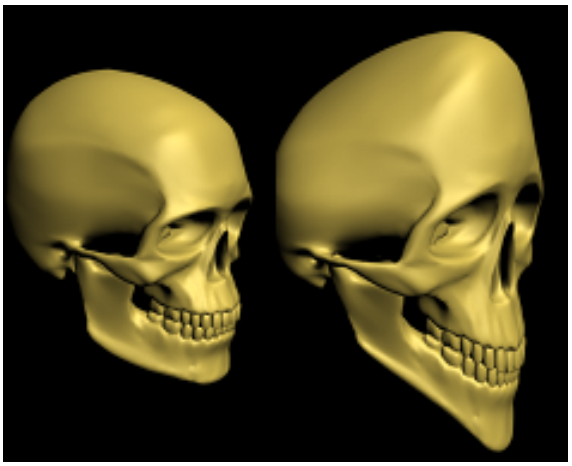

Figure 5.11: Original target model (Left) and an arbitrarily deformed model (Right) created by applying a free form deformation (FFD) technique to the model on the left.

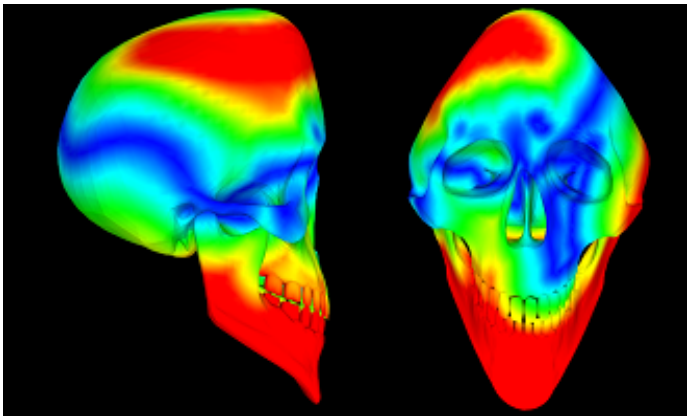

Figure 5.12: Surface comparison between the models in figure 5.11. A BGYR colour scale is used where blue represents nearest points while red represents points with more that 20mm of difference.

Figure 5.13 shows the distances between D_j and R at each iteration and for three different SF. The graph illustrates the behaviour of the algorithm for the parameters $SF = 0.1$, $SF = 1.0$, and $SF = 10.0$. The comparison was conducted for 80 iterations.

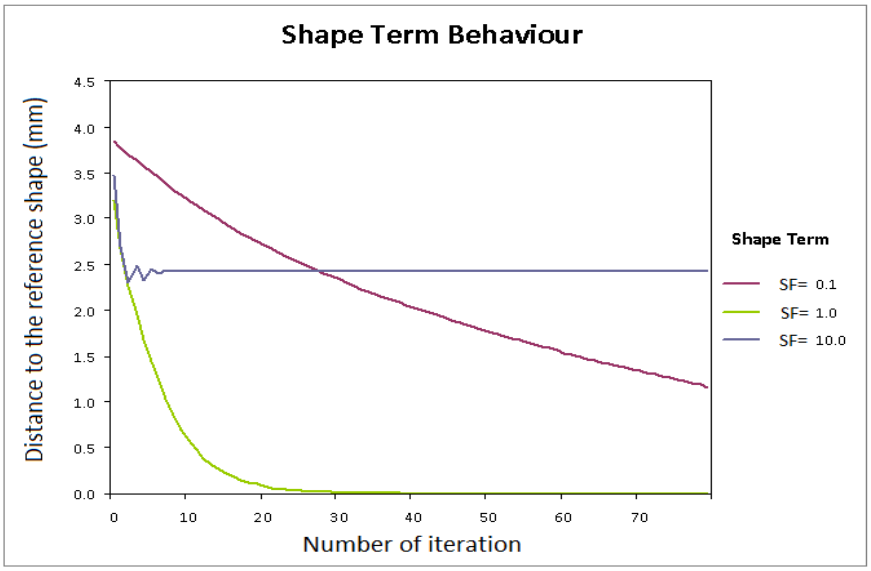

Figure 5.13: Graph showing the behaviour of the shape term result with respect to a reference R model after 80 iterations.

Figure 5.13 shows that when using $SF = 1.0$, the resulting model converges towards a solution (in this case represented by $y = 0.0$) in a regular and smooth way after 30 iterations. The graph shows that if the shape is reduced to one tenth of the original value ($SF = 0.1$) the curve decreases regularly at a slower rate. When a higher shape factor is used ($SF = 10.0$), the algorithm converges to a shape configuration before the first 10 iterations. In this case, this solution is around 2.5 mm from the base line defined by R. This behaviour is expected and the reason for that is because the shape term makes the deformed model D converge to the nearest shape configuration with respect to its current dimensions at a given state (i.e. the invariant formulation includes possible changes in the scale of the objects). This convergence is abrupt because the factor used is high. When the shape factor is higher the first iterations present abrupt changes before stabilising. These cases exemplify the three main situations available when setting up the shape term parameter. Figure 5.14 shows the results of the parameter combinations.

5.6.3 Effect of the volume features and shape restrictions

In this set of tests, the aim was to illustrate the effects of combining shape and volume feature terms. The test involves segmenting the MRI volume of subject 1 of the UOS with different parameters for volume and shape weighting factors. The source model S is the initialised skull template according to the initialisation procedure presented in section 5.4.3. The parameter values tested are shown in table 5.2 and a graph illustrating the results is presented in figure 5.15. The graph shows the distance between D_j and R at each step j of the skull segmentation algorithm. For clarity, the graph only shows the first 20 iterations of the algorithm. In this case (similar to the previous test), R is an average model obtained by applying the algorithm with $SF = 1.0$ with 100 iterations to the deformable model S . As shown in table 5.2, four cases were tested.

In case 1, only image features were used to direct the segmentation process ($VFF = 1.0$, $SF = 0.0$). After initialisation, the deformable model evolves guided by image features

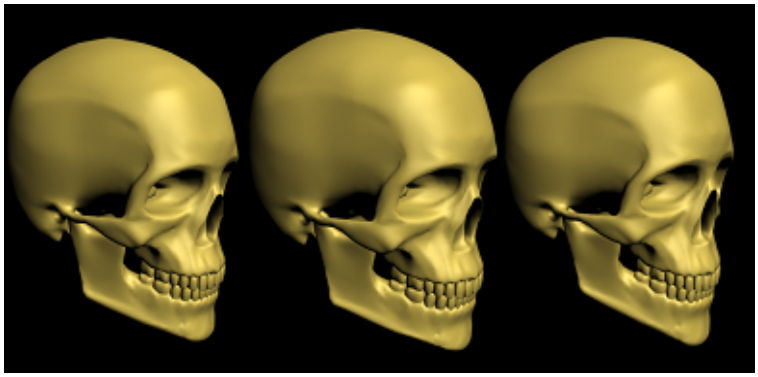

Figure 5.14: Results after 80 iterations for the three shape parameters plotted in graph 5.13: $SF = 0.1$(left); $SF = 1.0$(middle); and $SF = 10.0$(right).

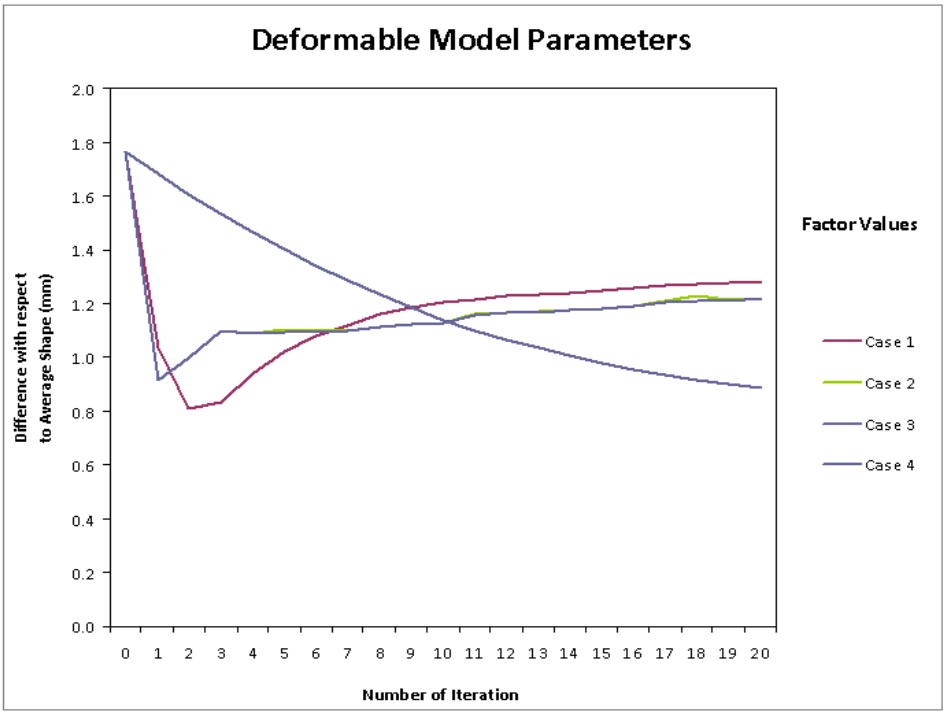

Figure 5.15: Evaluation of results for four combinations of image feature and shape factors.

Case i	Image Features	Shape Factor	Behaviour of the curve
1	$\beta = 1.0$	$\gamma = 0.0$	unsmooth and divergent
2	$\beta = 1.0$	$\gamma = 0.1$	unsmooth convergent
3	$\beta = 1.0$	$\gamma = 1.0$	smooth and convergent
4	$\beta = 1.0$	$\gamma = 10.0$	smooth and convergent

Table 5.2: Four image feature and shape factors applied for segmenting a skull model

defined by edges of the noisy skull volume and the influence of its gradient vector flow field. Regions of the deformable model far from the skull volume are pulled towards the borders of the skull. As a result, the surface of the model generated after 20 iterations is apparently similar to the surface of the skull volume in terms of surface distance value but it is a "poor result" in terms of shape. The entire skull configuration contained in the initial deformable model is distorted at each step of the algorithm when there is no restriction apart from the image features. The spike at the area of the left zygomatic bone (see figure 5.16) is in this case due to some noisy data near the skull influencing the template evolution. The deformable model evolves blindly towards the borders of the volume of interest. In the graph it can be observed that the algorithm converges towards a solution near to the final volume, but as the number of iterations continue this model diverges from the solution. Figure 5.16 (second row) shows that the left zygomatic bone has an outlier due to noise components in the volume, causing the skull shape to be distorted. Also, the nasal aperture presents an unusual asymmetry due to free deformation with no shape restrictions.

In case 2, the deformable model is now under the influence of a small amount of the shape term. With respect to case 1, this setting modifies the behaviour of the algorithm by imposing a restriction in the evolution of the deformable model. However, the amount of shape influence is small compared to the image feature amount ($VFF = 1.0$, $SF = 0.1$). The algorithm gives more priority to the image feature term resulting in a final configuration that is still poor in terms of shape. Figure 5.16 (third row) shows a small improvement in the final skull shape. This improvement can be observed in the area of the back of the skull (contours of the parietal bone area) and the zygomatic arch. There are still problems with the noise in the left zygomatic bone area.

In case 3, a balanced combination of image features and shape factors is used. The results are improved in terms of global shape parameters. Figure 5.16 (4th row) shows that the problem in the left zygomatic bone has been corrected, as the shape term stops the deformable model accepting such outliers. Also the area of the mandible has a more regular and smooth surface. The nasal aperture maintains some symmetry, and, furthermore, the area of the maxilla and especially the left superior teeth area are also corrected with respect to the previous configurations presented.

Finally for the 4th case, when there is a high shape factor, the deformable model gives priority to the shape term, making the model converge to the nearer average skull shape almost independently of the image features. This is similar to the results produced using the pure shape term variation in section 5.6.2.

The processing time for registering two sets of curves with 700 points each is 7 minutes approx. and using 60 iterations. This number of points was the average used for registering each of the skull models. For calculating the gradient vector flow in 3D for a sub-volume of 256x256x50 voxels the processing time is 16 minutes using 120 iterations for calculating

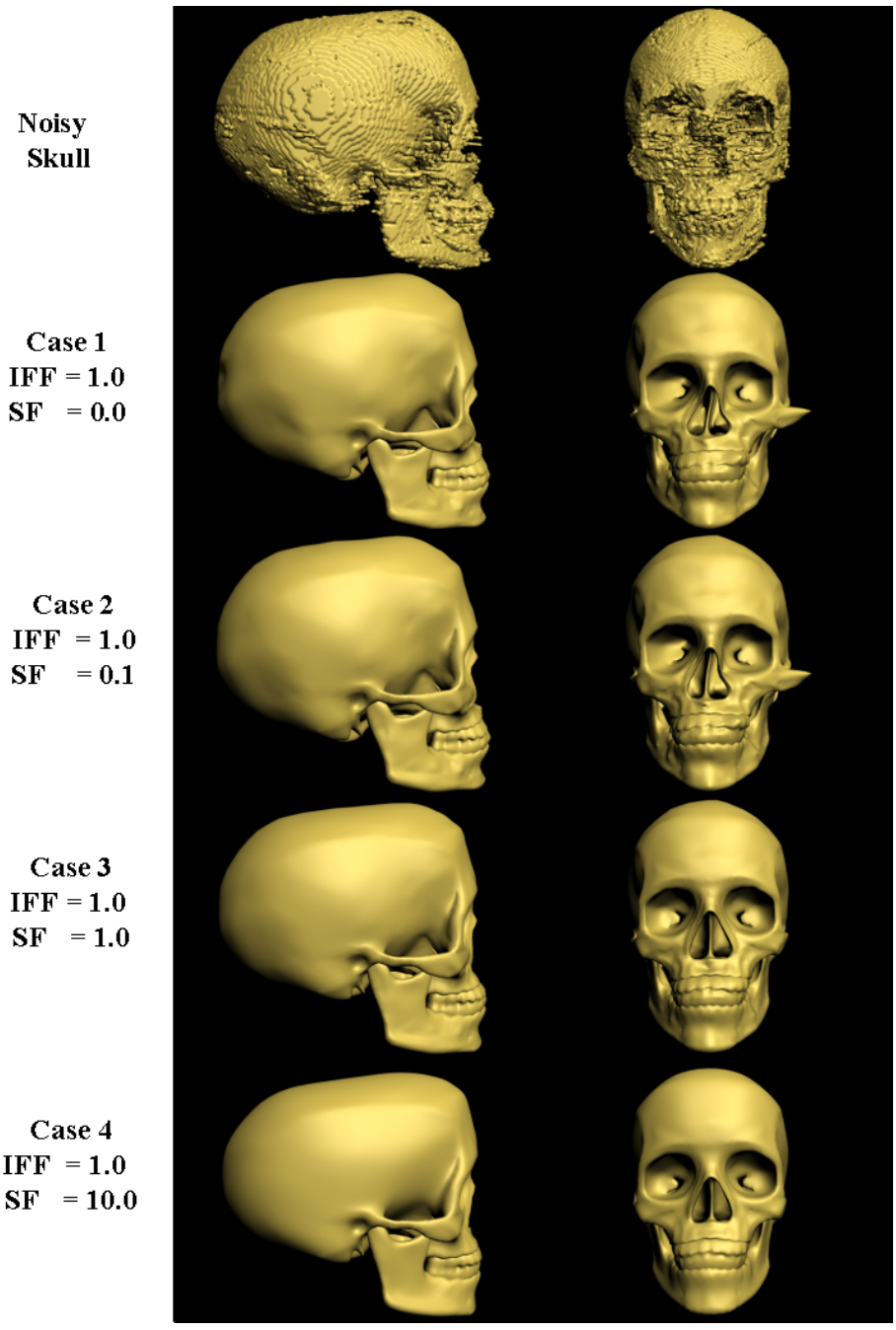

Figure 5.16: Results of the segmentation process combining Image Feature Factor (IFF) and the Shape Factor (SF)

the solution to the gradient descent differential equation. The sub-volume dimension corresponds to the spatial region of the MRI volume was the area of the head is located. A total of 180 hours were required to process the 60 skull models of the database using 3000 control points per model and 100 iterations (i.e. 3 hours on average per dataset)[5].

5.7 Creating a database of skull-face models

Skull shape varies from individual to individual. One shortcoming of using global shape descriptors is that new models tend to be deformed to the shape configurations spanned by the trained shape space. Working in combination with the covariance regularisation a strategy of local matching gives the algorithm flexibility to deal with new skull configurations.

5.7.1 Parameters used in the extraction process

The strategy to address the problem of skull global shape variability was implemented in two stages. First, the template deformation based segmentation algorithm was applied to the noisy skull volumes with 100 iterations using a deformable model with control points along the entire skull surface equally distributed. The number of control points used was 3000. The training set was created with a subset of vertices of the synthetic skull template. As explained in section 5.3.3, a skull model generated from the VHP male skull and five skull model approximations were included in the training set in order to include shape variability.

In the first stage, small values for the shape term were used to give more weight to the image feature term ($VFF = 1.0$, $SF = 0.015$). The results of the segmentation at this stage are skull templates with features globally matching the noisy skull volume, i.e. the models are not completely correct in some parts.

In a second stage, a local correction process was applied to skulls produced in stage 1. This used the same deformable model template configuration but with a denser number of control points in specific regions: 1024 points in the area of the face, and using $VFF = 0.1$, $SF = 0.5$ and 100 iterations. The regions of the skull enhanced in the second stage are: the eye aperture borders, the noise aperture contour , the zygomatic bridges and the border of the jaw. This local correction step allows the algorithm to recover the shape in specific areas. Also, in combination with the variance regularisation, local correction gives the flexibility to segment a wide range of skull shapes.

In general, the parameters values were found by running several tests based on the test criteria presented in sections 5.6.2 and 5.6.3 selecting the combinations of parameters with regular behaviours for the 60 skull models.

5.7.2 Three dimensional Database of head Models

The results of applying the previous algorithms to the UOS MRI dataset is a new database of 60 skull and skin models. Figures 5.17 and 5.18 shows an entry of the database. Figures 5.19 and 5.20 show the skull and face model structure. Each model consists of two 3D triangle meshes representing the skull and face layers. The skull model consists of 18,546 vertices and 36,710 triangles whilst the face model consists of 25,566 vertices and 49,128 triangles.

[5]These results were obtained using a Dell Dimension DXP061 computer with two Intel(R) processors

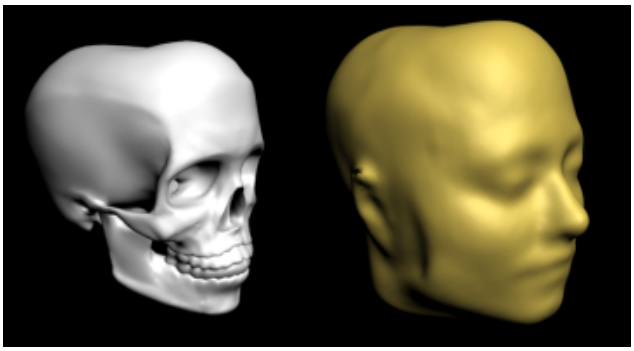

Figure 5.17: The resulting surface models for the skull and face of the first individual of the database. The face model is produced using the isosurfacing technique presented in section 3.2.

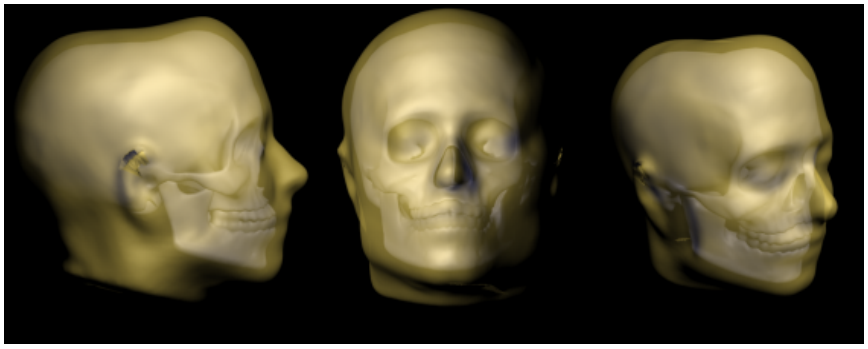

Figure 5.18: Superimposed layers of the skull and face for the first individual of the database.

The set of skull-face models has several useful characteristics that can benefit the design and implementation of a craniofacial reconstruction system:

First, the amount of points in the skull and face offers a great level of detail to analyse the skull-face relation. Additionally, the vertices of the resulting models defining the surfaces can be refined at the level of detail required. The analysis of the face can be more detailed in comparison with current techniques that use a sparse set of anthropometric landmarks.

Second, the template is created with an explicit model of a skull which makes it easy for the user to manipulate. This is in contrast to abstract representations used in other approaches such as, for example the level-set [39, 25] formulation which uses an implicit function in 4D to represent the skull surface at a given level.

Third, the origin of the skull models is the same deformable model (template represented with a triangle mesh). In other words, they are represented using the same system of reference. This facilitates the way they can be used for their analysis in different contexts. Several processes of the craniofacial reconstruction systems benefit from this property such as the statistical analysis, the training set creation, the feature location, matching of models, etc. A set of corresponding points is always required for conducting these tasks. The correspondence between models also eliminates the problem of landmark interpretation and placement. In the case of the face models, they are also created with a common face template and, similar to the skull models, this facilitates their analysis under different contexts.

Fourth, the database consists of skull-face models for each subject. This property make it is possible to test different craniofacial reconstructions strategies and systems by using a subset of models of the database. The rest of the models can then be used to simulate unknown skulls to be reconstructed. It is possible to assess the results quantitatively by comparing the surfaces of the real models with the reconstructed models. This will be done in chapter 6.

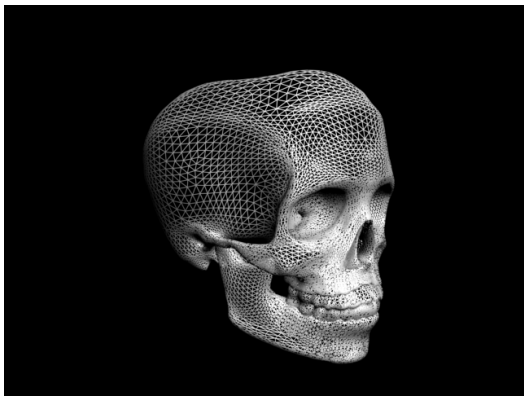

Figure 5.19: Resulting skull mesh generated from the 3D skull segmentation approach.

6600 running at 2.4GHz and 2.0 GB of ram memory.

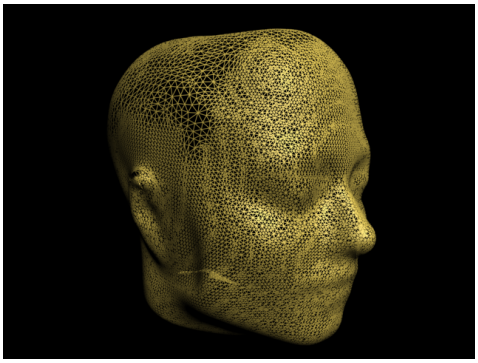

Figure 5.20: Face mesh. Result of the extraction process of the face layer.

5.8 Summary and discussion

In this chapter, a 3D technique for segmenting the skull in MRI data problem was presented. The technique works by incorporating statistical knowledge of the skull shape to a deformable model evolving toward volume features under a gradient vector flow field. A bootstrapping algorithm requiring only an initial rough approximation of the skull is proposed. A first approximation of the volume of the skull is iteratively refined combining shape knowledge and image features. The technique presented in this chapter, combined with the skin extraction process (see section 3.2), are the two main components needed for creating skull-face models from MRI datasets.

The segmentation technique presented was applied to the UOS MRI dataset, resulting in a unique dataset of detailed skull-face models. This database has applications in craniofacial reconstruction systems. The skull extraction algorithm can also be used for segmenting other kinds of MRI data.

An approach similar to the work presented in this thesis is presented by Luthi et. al. [59]. A deformable model of a skull is used to segment the skull in a pre-processed MRI head volume. The skull and the deformable model are registered using a landmark based approach. A set of landmarks are manually identified in both skull models and this relationship is used for defining the non-rigid registration. In contrast, our work uses a two sets of 3D curves in both models. To maintain the shape of the deformable model, Luthi et. al's technique implements a shape term defined with the (PCA) coefficients of a statitical model of skull shapes. The deformable model mesh is deformed under the shape restrictions at each step of an iterative algorithm. Both aspects are similar to our approach. However, to impose more control on the shape, the deformable model in Luthi et. al's approach is defined at different level of details and the head volume must be processed several times. The resulting model at each cycle (i.e. for each level of detail) is combined to maintain the deformable model mesh structure. In contrast, our technique requires only one deformable model at the same level of detail during all the process. In Luthi et. al's work, the statistical skull model requires several skull samples to be constructed given the issues with the covariance matrix. In contrast, our technique does not have restrictions on the number of models to use (i.e. from one to n models can be used). In our approach a covariance regularisation step is incorporated, which makes the shape term calculation more robust and requires less skull models to train (only one model is needed as a minimum).

The results of the technique presented in this chapter can be used directly to conduct statistical studies about measures and proportions of the skull and face. Some examples of possible applications of this type of data, not only in forensic but also in other medical applications, are for example calculating a geodesic distance between features, approximating areas to continuous functions for analysing geometrically some parts of the skull, analysis of the relation between specific skull and face regions, etc. In the next chapter, the database of skull-face models created using the techniques described in this chapter will be used as part of a new craniofacial reconstruction approach.

Chapter 6

A Computer-Based Craniofacial Reconstruction System

The aim of forensic craniofacial reconstruction is to produce an estimated face model corresponding to an unknown skull, for identification purposes. To make the reconstruction process faster, more flexible and reduce some of the subjectivity and inconsistencies associated with traditional approaches, two and 3-dimensional computer-based reconstruction systems are being developed [12]. Computerised facial reconstructions have the advantage that they can be implemented in situations where traditional facial reconstructions cannot or where the implementation of traditional approaches would be simply impractical (e.g. in the case of mass disasters) [30].

Despite the development of computer based approaches, some authors argue that the reasons to continue using traditional techniques for creating facial reconstructions is the realism they provide: "the main advantage of traditional techniques is the realism provided by the artist on the final result of the process" [1]. In constructing hand made face models, accuracy is sacrified for visual realism leading to craniofacial methodologies where non reproducible results are obtained. The main issues in computer based approaches are how to represent the relationship between the main variables defining a human face (e.g. skull shape, age, ethnicity), and how this relationship can be exploited to create more reliable and replicable results. In this respect, this work does not pretend to replace the role of the forensic artist but to supply her with computational tools allowing her to make more objective and reproducible facial reconstructions.

According to Wilkinson [109] there are several steps which an ideal computer-based facial reconstruction system has to cover. First, information must be collected about the skull to be analysed. This process can be done using a 3D scanner device (e.g. a laser scanner). Second, the reconstruction process must be defined where information about age, sex and ethnic group of the person can be added. Third, the facial reconstruction is produced. In addition, current information sources for creating facial reconstructions must be diversified to take advantage of modern technology, benefitting from its capability to produce more detailed and complete information about the structure and composition of the human head.

In this chapter, a method for creating a craniofacial reconstruction system using information sources generated from MRI data is presented. The information consists of 3D models of the skull and face. The database of head models presented in chapter 5 provides the essential mechanism to design a system in which the computer can be used to create a

[1] Martin Evison, Personal communication, October 2004.

face estimation algorithmically. Based on the implicit information contained in the head model database. Combined with a registration-based craniofacial reconstruction approach using a spatial deformation technique, a novel approach to Craniofacial Reconstruction (CFR) is presented in this chapter.

The chapter is organised as follows: Section 6.1 describes some preliminary considerations and notation used on the rest of the chapter. Section 6.2 presents an overview of the CFR system architecture. Section 6.3 the function of the biological and geometric skull analyisis component of the system is described. In section 6.4 is presented the template head construction method used for approximating the reconstructed face. The approximation is achieved by fitting the skull model of the template to the unknown skull being analysed. In section 6.5 the process of face reconstruction from the head template is described. In Section 6.6 the summary and conclusions of the chapter are presented.

6.1 Preliminary Considerations

The database of head models is represented by the set $H = \{S_i, F_i\}$, where S_i and F_i are i^{th} skull and face models in the database respectively. The unknown skull and its corresponding face model will be referred by the terms S_u and F_u respectively. These models are both elements of a head model H_u (i.e. $H_u = \{S_u, F_u\}$). For testing purposes the unknown skull is simulated by choosing and removing one of the skulls of the database. The reconstructed face model $\hat{F}_u$, can be compared quantitatively with the real unknown face F_u. This means that different strategies for the craniofacial reconstruction system can be tested and evaluated.

6.2 Overview

The craniofacial reconstruction system consists of three main elements as illustrated in figure 6.1: Skull Examination, Template Construction and Face Construction. The input skull is analysed and a set of main features extracted. Combining these features with information about the skull-face relationship, and a spatial deformable technique, this system creates possible face estimations for the input skull. The anthropometric information is provided by the database of head models presented in chapter 5. The use of the face surface to deform the surrounding 3D space (equivalent to volume deformation) addresses some of the problems encountered in techniques based on estimating landmark positions in models [64, 104]. The use of spatial deformation allows the facial tissues (skull, muscle, etc.) to be dealt with as a single component, thus freeing the procedure from the problem of placing and interpreting anthropometric landmarks associated with soft tissue depth tables. Facial soft tissues should change in response to the changes in the skull, and therefore the face is not merely a mask depending on a small number of soft tissue depth points, as is the case, for example, in [22].

Each of the elements of this craniofacial reconstruction system are made up of modules designed for specific tasks and they will be explained in the following sections.

6.3 Skull Examination

For a real, unknown skull, the results of the forensic, anthropological and dentological analysis, as well as findings obtained at the site where the corpse was found, are com-

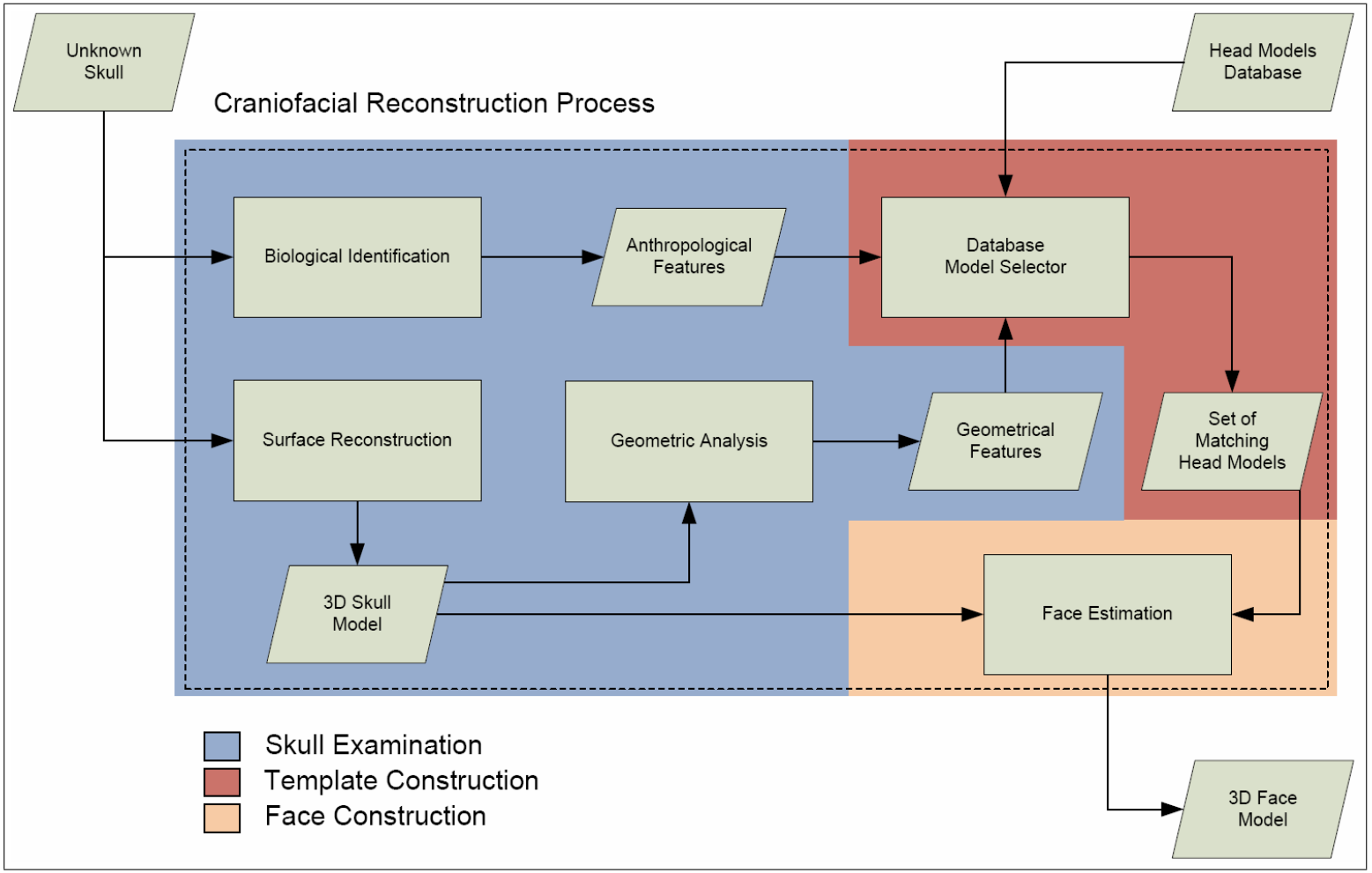

Figure 6.1. System for creating Craniofacial Reconstructions

piled and organized. In our system, there are two main modules designed to extract this information: the biological identification module and the geometric analysis module.

6.3.1 Biological Identification

This is the first step in a craniofacial reconstruction system [103], as described by Quatrehomme [75]: "Whatever the technique adopted, CFR demands a thorough anthropological analysis. After a precise observation of the skull, the classical measurements (horizontal, vertical and sagittal) must be made. Index and angles are calculated, giving the race and the general shape of the skull and face".

We assume this analysis has been conducted and the main characteristics of the individual such as ancestry, sex, age and body constitution have already been determined (labelled as 'Anthropological Features' in figure 6.1). All this information is available from the individuals modelled in our database. Thus we can choose to use or ignore specific criteria in the reconstruction process. For example we could choose to only use the sex information, or to use the body mass index, etc. Chapter 7 will present a series of reconstructions where different criteria are used in the reconstruction process. In a real situation, this will be an external module where the information is supplied by a forensic expert analysing the skull remains.

6.3.2 Skull Digitisation and Surface Reconstruction

In order to conduct a proper geometric analysis of the skull using computiational tools, it is necessary to create a digital representation of this object. This can be done using a laser scan, CT or MRI. Usually, the skull will be sampled and represented as a 3D sparse point set in the case of a laser scan, or as a stack of images forming a volume in the case of CT and MRI devices. In all cases, an isosurfacing process (similar to the processing used for extracting the face from MRI, as described in section 3.2), can be applied to the digital volume. In our case, when a model from the database is selected this step is not necessary because the skull is already in digital form.

6.3.3 Geometric Analysis

Once in a digital format, it is possible to conduct a geometric analysis of the skull in order to determine the main features describing its shape. To facilitate this analysis, a registration process is carried out between the digitised skull and a 3D skull template. The registration method used is the Robust Point Match algorithm [19, 20] (see appendix F) applied to a set of 3D feature curves matched between the models to register. This strategy is the same as used in the template initialisation process described in section 5.4.2 and uses the same set of curves. These curves are used because they can be consistently identified in different skull models as explained in section 5.4.2.

This registration step is necessary so that the unknown skull is in a common reference system making it possible to determine spatial correspondences with other skulls. The advantage of the registration process will become evident when the deformation approach is presented in the following sections.

6.4 Template Construction

In this stage, the database model selector chooses a set of head models from the database matching some criteria in terms of the unknown skull features. Features such as the age, sex, body constitution, PCA coefficients, and geometric properties of the unknown skull are used as selection conditions. The aim of the selection module is to create a set of base models $\mathbf{H}_b$ consisting of k reference head models whose facial models F_r^i $(i = 1 \dots k)$, will be combined for producing a face estimation:

$$\mathbf{H}_b = \{\mathbf{H}_r^1, \mathbf{H}_r^2 \dots \mathbf{H}_r^k\} = \{\{S_r^1, F_r^1\}, \{S_r^2, F_r^2\}, \dots \{S_r^k, F_r^k\}\} \tag{6.1}$$

The reference models are a group of selected head models from the database with similar skull features than the unknown skull being processed.

As previously stated, the skull component S_u will simulate the skull of an unknown deceased person, and will be used as the input to the reconstruction algorithm. The skin layer F_u will then be used to evaluate the results. Figure 6.2 shows a schematic diagram of the stages involved in the template selection and face estimation processes.

To create the set $\mathbf{H}_b$, each of the i head reference models $\mathbf{H}_r^i$ will be selected according to a similarity criteria between S_u and each of the reference skulls S_r^i. For example, if the criterion is the minimum procrustes distance [35] d between the skull shapes, then for a database of head models with n elements, the base model set $\mathbf{H}_b$, is the set of k models defined by the following expression:

$$\mathbf{H}_b = \{\{S_r^i, F_r^i\} \mid i \in \{j \mid d(S_r^j, S_u) < \varepsilon, j \in \{1 \dots n\}\}\} \tag{6.2}$$

where n is the number of elements of the database, S_r^j is a reference skull model of the j^{th} database entry, and $\|\mathbf{H}_b\| = k$ for some threshold value ε accounting for a limit for the difference in procrustes distance d between models S_r^j and S_u.

The elements of the set $\mathbf{H}_b$ are the base head models used for creating a head template. Figure 6.2 shows an example for selecting one of the elements $\mathbf{H}_r^i \in \mathbf{H}_b$. The process of transforming the set $\mathbf{H}_b$ to an estimated face is presented in the following section.

6.5 Face Reconstruction

In this stage, the information of S_u, and the set $\mathbf{H}_b$ are combined in order to produce a face. A deformation approach is used for adjusting the shape information of the models contained in the set $\mathbf{H}_b$, fitting the skull S_b to the unknown skull. An average model of the face layers is calculated and used as an estimation of the face for the skull S_u. The details of the deformation function are presented in the next section. The final face model construction process involves 2 main sub-processes: the face estimation and the warping of the chosen database models to the unknown skull.

6.5.1 Face Estimation Process

Figure 6.3 shows schematically the face estimation process. In this stage, a deformation function f will be calculated between S_u and each of the reference skulls $S_r^j \in \mathbf{H}_b$. This function is defined as:

$$f_j(S_r^j) = S_u \tag{6.3}$$

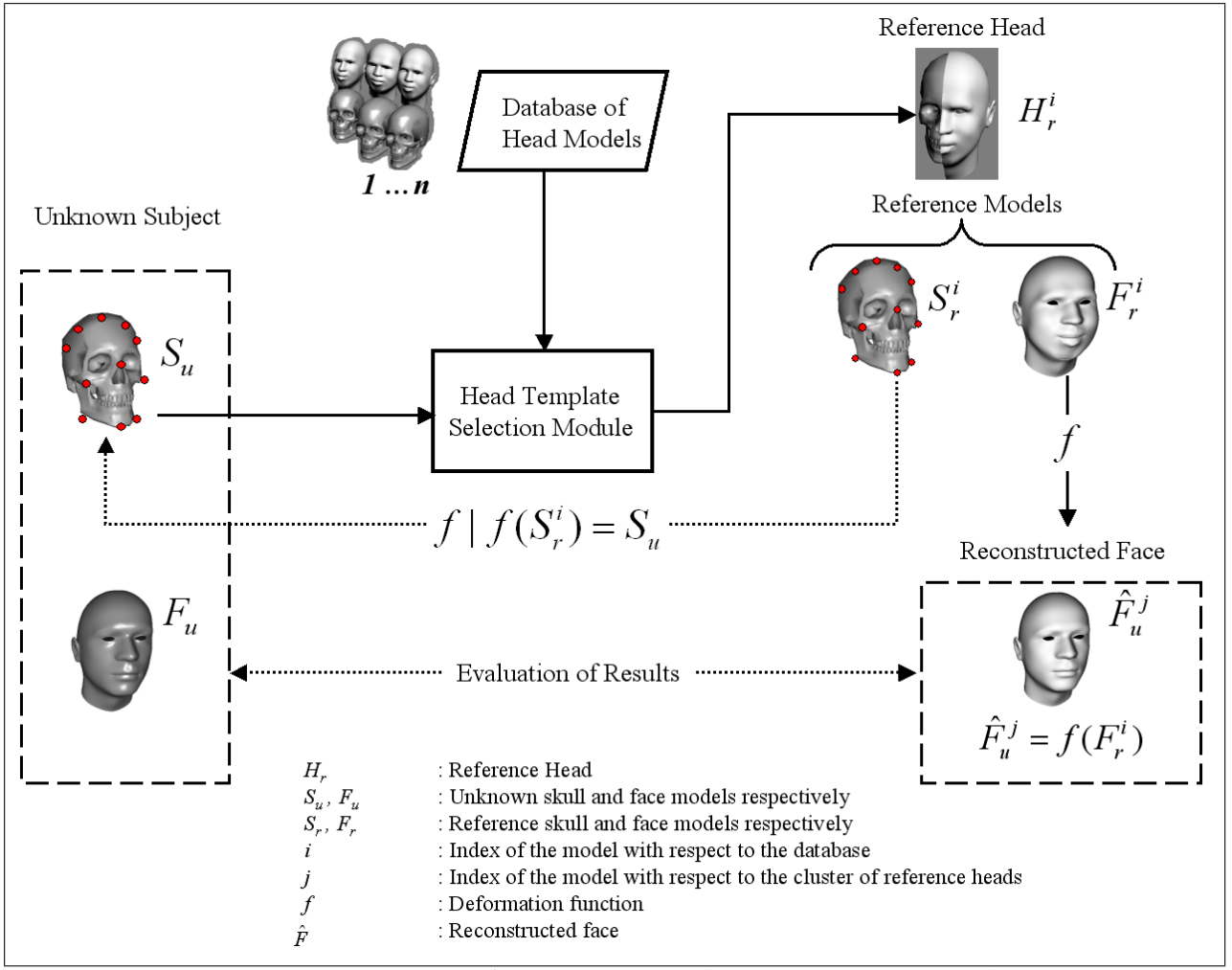

Figure 6.2 The template selection process. An unknown skull S_u is given as input and after an analysis, the selection module obtains a reference head model H_r^i. This reference model, one of the n different models contained in the database, is selected according to a set of matching criteria with respect to the skull S_u. A function f representing a spatial deformation is calculated fitting the skull S_r^i to S_u. This function, applied to the reference face F_r^i will be used to estimate an unknown face F_u^j.

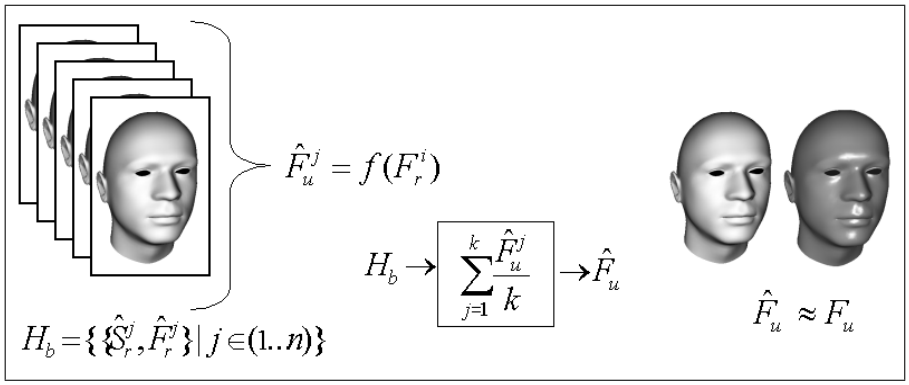

Figure 6.3: Process of face construction from the template.

This mapping function f_j will be used to estimate a deformed face $\hat{F}_u^j$ for each of the j reference models, by applying this function to the corresponding reference face F_r^j as follows:

$$\hat{F}_u^j = f_j(F_r^j) \tag{6.4}$$

The resulting reconstructed face $\hat{F}_u$ is then the average of the $\hat{F}_u^j$ elements:

$$\hat{F}_u = \sum_{j=1}^{k} \frac{\hat{F}_u^j}{k} \tag{6.5}$$

The functions f_j are based on the Radial Basis Function deformation approach [14]. This approach requires a set of matching control points between a source and target model. In general, finding a set of matching features in two 3D models is a complex task. However, the structure of the models obtained in the extraction process described in chapter 5 facilitiates this task, as described in the next section.

6.5.2 Warping the Template to The Unknown Skull

Both the unknown skull S_u and each of the reference skulls S_r contain a set of control points. A Radial Basis Function (RBF) is used to deform S_u into S_r.

The vector x of control points for each skull model is a subset of the vertices of the skull models. These vertices are the result of a regular sampling process carried out using a kd-tree data structure on the topology of the skull mesh. The number of points used for matching the skull models is 3000. These points are the same points used as control points in the template registration process presented in chapter 5. It is complex to determine matching points between two three-dimensional objects specially when the number of points in the sets to match are not equal. However, in our case, this process is direct and simple because all the skull meshes are referenced to the same model, i.e. the meshes share topology and the vertices are in the same relative spatial positions.

In general a RBF is a smooth, continuous function which interpolates the given data and provides at least C^1continuity. A RBF offers several advantages over other methods of deformation[14]. The geometry of the control-points is not restricted to a particular configuration. This implies that the distribution of the control-points can be both sparse and irregular [111]. Another advantage is that the behavior of the interpolant can be

controlled to meet specific requirements. A RBF can be purely deformable, or contain some form of linear component allowing both local and global deformations.

Interpolation aims to approximate a real-valued function $f(\mathbf{x})$ for which we have a finite set of values $f = \{f_1,\ f_2, ...,\ f_n\}$ at the distinct points $\mathbf{x} = \{x_1,\ x_2, ...,\ x_n\}$. In 3D each function f and point $\mathbf{x}$ has 3 components for each dimension, i.e. $\mathbf{x}_j = \{x_j, y_j, z_j\}$, $f_j = \{u_j, v_j, w_j\}$ for $j = 1...n$. Therefore, defining the object which interpolates a number of known points relies upon determining the coefficients α_i from the expression:

$$f_k(\mathbf{x}) = p_m(\mathbf{x}) + \sum_{i=1}^{n} \alpha_i \phi_i(\parallel \mathbf{x} - \mathbf{x}_i \parallel) \tag{6.6}$$

The coefficients of the function $f_k(\mathbf{x})$ are determined by requiring that $f_k(\mathbf{x})$ satisfy the interpolation conditions: $f_1(\mathbf{x}) = u_j$, $f_2(\mathbf{x}) = v_j$, and $f_3(\mathbf{x}) = w_j$, $j = 1, ...n$ giving n linear equations and the additional compatibility constraints:

$$\sum_{i=1}^{n} \alpha_i^k = \sum_{i=1}^{n} \alpha_i^k x_i = \sum_{i=1}^{n} \alpha_i^k y_i = \sum_{i=1}^{n} \alpha_i^k z_i = 0 \tag{6.7}$$

The value of the function ϕ_i depends only on the distance of the point $\mathbf{x}$ to each of the control points $\mathbf{x}_i$ (The $\mathbf{x}_i$ points are called centers). The weights of the basis functions α_i are found by placing the centres back into $f_k(\mathbf{x})$ and solving the resulting set of linear equations.

The polynomial term p_m is included to allow a certain degree of polynomial precision. We now describe a way of calculating the interpolant function given a set of points in 3D. In the 3D form, the Radial Basis Function (RBF) transformation is determined by $n + 4$ coefficients in each dimension. These conditions gurantee that the RBF is affine reducible, i.e. the RBF is purely affine whenever possible. In the case where the polynomial is absent from the RBF, there are no corresponding compatibility constraints. The coefficients of the basis functions and the polynomial can now be found by solving the linear system [111]:

$$W = L^{-1}Y \tag{6.8}$$

$$L = \begin{bmatrix} G & P \\ P^T & \mathbf{0} \end{bmatrix} \tag{6.9}$$

$$G = \begin{bmatrix} g(r_{11}) & g(r_{12}) & \dots & g(r_{1n}) \\ g(r_{21}) & g(r_{22}) & \dots & g(r_{2n}) \\ \vdots & \vdots & \ddots & \vdots \\ g(r_{n1}) & g(r_{n2}) & \dots & g(r_{nn}) \end{bmatrix} \tag{6.10}$$

$$P^T = \begin{bmatrix} 1 & 1 & \dots & 1 \\ x_1 & x_2 & \dots & x_n \\ y_1 & y_2 & \dots & y_n \\ z_1 & z_2 & \dots & z_n \end{bmatrix} \tag{6.11}$$

$$W^T = \begin{bmatrix} \alpha_1^1 & \alpha_2^1 & \dots & \alpha_n^1 & p_{01} & p_{11} & p_{21} & p_{31} \\ \alpha_1^2 & \alpha_2^2 & \dots & \alpha_n^2 & p_{02} & p_{12} & p_{22} & p_{32} \\ \alpha_1^3 & \alpha_2^3 & \dots & \alpha_n^3 & p_{03} & p_{13} & p_{23} & p_{33} \end{bmatrix} \tag{6.12}$$

$$Y^T = \begin{bmatrix} u_1 & u_2 & \dots & u_n & 0 & 0 & 0 \\ v_1 & v_2 & \dots & v_n & 0 & 0 & 0 \\ w_1 & w_2 & \dots & w_n & 0 & 0 & 0 \end{bmatrix} \tag{6.13}$$

where ^{T} is the matrix transpose operator, $\mathbf{0}$ is a 3x3 matrix of zeros and p_{ik} are the coefficients of the polynomial. Notice that the $(i,h)^{th}$ entry of G is $g(r_{ij})$ such that:

$$r_{ij} = [\vec{x}_i - \vec{x}_j]^{\frac{1}{2}} \text{ or } r_{ij} = [(x_i - x_j)^2 + (y_i - y_j)^2 + (z_i - z_j)^2]^{\frac{1}{2}} \tag{6.14}$$

Intuitively, $g(r_{ij})$ measures the effect of the j^{th} control-point on the transformation at the i^{th} control-point. The system is now solved using Singular Value Decomposition (SVD) and the complete set of coefficients in W are obtained to evaluate equation 6.6.

After obtaining the coefficients of the interpolant, the function $f_k(x)$ is fully specified, and can be calculated in terms of a vector x of control points. This function f_k corresponds to the deformation used for estimating the reference face model $\hat{F}_u$ as previously described.

6.5.3 Evaluation of the Reconstructions

To evaluate the results of the facial reconstruction technique, a tool for comparing two meshes called metro [21] is used. Metro numerically compares two triangle meshes S_1 and S_2 independently of their level of detail. Metro evaluates the difference between the two meshes on the basis of the approximation error measure defined in [21]. It adopts an approximate approach based on surface sampling and the computation of point-to-surface distances (see figure 6.4). For a given point i the nearest point is computed evaluating the $d_i(p, S)$ distance. A square regular grid is created, covering the bounding box of the two meshes. Then a neighborhood data structure is constructed as an array of cells. Each cell containing a list of all vertices included in the cell as well as all the faces intersecting the cell. Given a point, the nearest point on a surface can be quickly found. The surface of the reference mesh S_1 is sampled, and for each elementary surface parcel the distance to the S_2 mesh is computed. Error is visualized by colouring the S_1 mesh with respect to the evaluated approximation error. For each vertex, the error on each mesh vertex (as the mean of the errors on the incident faces) is computed, and a colour proportional to that error is assigned. The faces are then coloured by interpolating vertex colours. For each point of the first surface, the neighbours in the second mesh are found and deviation between them found. Figure 6.5 shows an example of the output of this tool. Apendix B gives more details about the metro toolkit.

6.6 Summary and Discussion

In this chapter, we have presented a template-based craniofacial reconstruction system that makes use of data extracted from MRI data. The strength of this work lies in the extensibility of the sources of information and the approach adopted to conduct the reconstruction.

The MRI acquisition process, based on a non-invasive, detailed and safe technology, allows the data to be extended as required. The specific design of datasets for modelling the facial features of specific populations is possible. The data generated, in the form of surface models, makes it possible to model the skull-face relationship at different levels of

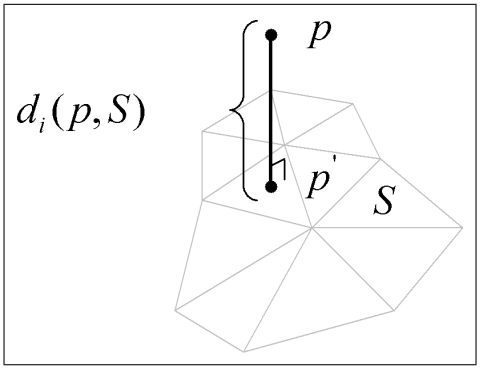

Figure 6.4: Distance from a reference point P in the base mesh with respect to the intersection of its normal intersecting the surface S at P'.

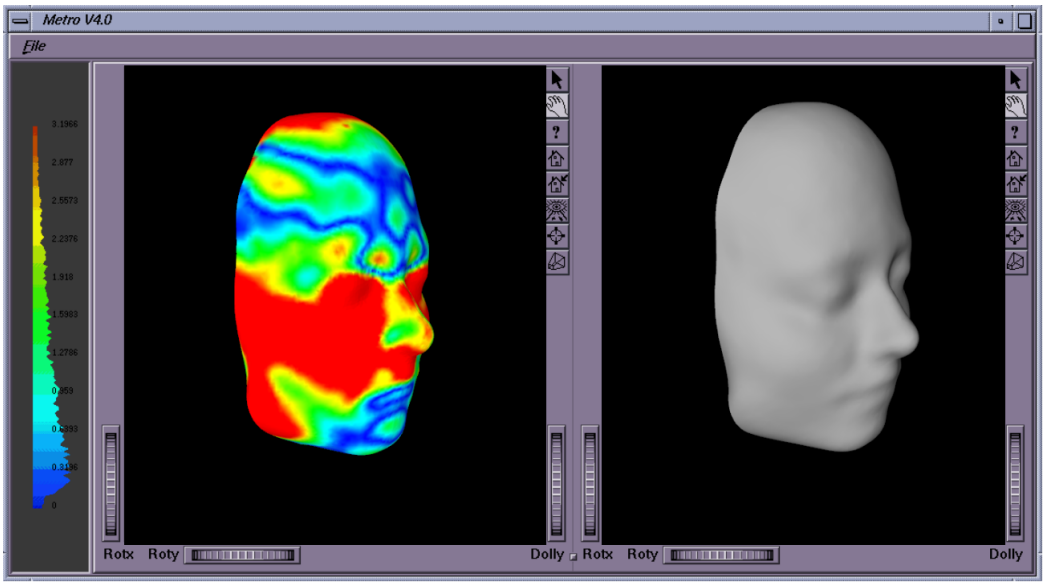

Figure 6.5: The metro graphic output window.

detail. Due to the density of the models (i.e. number of points contained in each model), continuous approximations to the skull and face models are also possible.

Based on the 3D set of head models, the sources of information used provide the craniofacial reconstruction system with a series of advantages. First, using an implicit way to incorporate tissue depths of the whole head, the dependence of the skull-face is modelled statistically, rather than inferred from a limited number of anthropometric landmarks coming from specific populations.

Second, the models used in the systems are referenced to a common model (i.e. they share the same triangular mesh topology). The registration of the skull and face meshes was conducted by using anatomical features as references. Points in a given area of one model are then related to similar indexed points of any other model in the database. Hence, features can be located and matched automatically between models by referring to the same index vertices. This advantage ameliorates the problem of landmark interpretation and location between models found in several CFR systems. Additionally, this property facilitates the statistical analysis of the skull and face given that the models are represented using a common system of reference.

Third, the possibility of creating a large scale database of head models, will contribute to the area of craniofacial reconstructions in the sense that quantitative studies can be conducted to assess the reconstruction results. Most work in the area proposes different strategies to accomplish the CFR task. However, most of them cannot be assessed quantitatively because insufficient data is available to assess the results.

The architecture of the system gives an initial platform to experiment with new techniques. The use of an algorithmic method to reproduce the face guarantees repeatability in the results. The modular design makes it possible to replace specific components with its functionality so that other combinations can be tested in the system.

A validation study showing the system functionality will be presented in the next chapter. The mechanism to evaluate the results, at the surface level will use the techniques presented in section 6.5.3.

Chapter 7

Evaluation of the Craniofacial Reconstruction System

This chapter presents a set of experiments for testing our craniofacial reconstruction system using the database of head models presented in chapter 5. The main objectives of the experiments are: to show that it is possible to create facial approximations close to the real face for a given skull (reconstruced faces with less than 2 mm average error with respect to real facial surfaces), and to evaluate the results of several facial reconstructions when different criteria are given to the system. The latter, will contribute to the discussion on whether providing more criteria to the CFR system will result in better reconstructions. In this context, as we are interested on surface similarity, good reconstructions are those which minimises the surface to surface distance similarity.

In section 6.6, the strategy to estimate the face for an unknown skull based on a set of head models was presented. The head models selected from the database are chosen by a selector module. The selector chose models with similar skull features to the skull being analysed according to a set of criteria such as geometric similarity, age similarity, sex, etc. A template head is built from the set of selected heads and used to produce the final face. Figure 6.2 illustrates the elements involved in the model template construction. Section 7.1 will describe the criteria used for selecting the models used for constructing the template model. The criteria used will potentially impact upon the final reconstruction. Section 7.2 will describe how the criteria are chosen. In section 7.3 are presented the results of the experiment. A discussion of the results is presented in section 7.4.

7.1 Criteria for creating the head template

The database used for this experiment consists of 40 head models. A set of representative features for each skull was obtained and used. The set contains the most common features used for identification in forensic applications (i.e. sex, age, ethnic group and body build) [109]. Additionally, another two features involving geometrical properties of the skull were also included: Principal Component Analysis (PCA) coefficients of the skull models [44] and Procrustes distances between skull models [47]. These two geometrical features were calculated using all the vertices of the mesh of the skull models [40]. Including both, PCAs coefficients and Procrustes distances between skulls, is useful to determine the impact of the skull similarity factor in the final reconstruction results. The database was partitioned in 5 different ways using the following conventions to define each partition type:

- Sex: Models are classified in males and females.

- Age: Five categories were defined in terms of a range of ages for each individual in the database. The ranges are defined as shown in table 7.1.
- Tissue Volume: The volume of the tissue was approximated from the 3D head models by calculating the difference between the volume of the face model and the volume of the skull. This ratio is assumed to be directly proportional to the body mass index BMI. For simplicity we will use BMI to refer to this partition.
- PCA: The first 17 principal components (representing more than 95% of the variations in the skull models) were chosen for each of the skulls, then 5 groups were defined using a K-Means clustering algorithm with five kernels [32]. Each of the subjects in the database is assigned a PCA group.
- Procrustes Distances: For each model in the database, a Procrustes alignment is conducted against the rest of the models in the database and then the five models with the lower distances are chosen for each skull.

The first three partition types reflect the usual features extracted from skull examination. PCA and Procrustes distance partitions are used to assess the impact of using head models with similar skull shapes.

Feature	Class group	Class label	Number of elements in the class	Male	Females
Sex	01	sex_1	20	20	0
	02	sex_2	20	0	20
Age	20-25	age_1	13	7	6
	26-30	age_2	6	3	3
	31-40	age_3	7	2	5
	41-50	age_4	6	5	1
	51-70	age_5	8	3	5
PCA	01	pca_1	12	8	4
	02	pca_2	3	2	1
	03	pca_3	15	5	10
	04	pca_4	1	0	1
	05	pca_5	9	5	4
Tissue volume	01	$tvol_1$	8	0	8
	02	$tvol_2$	9	3	6
	03	$tvol_3$	13	8	5
	04	$tvol_4$	5	5	0
	05	$tvol_5$	5	4	1

Table 7.1: Distribution of the database with respect to main biological and geometrical features. The procrustes feature is not included in this table because the sets of models to construct the template are particular to each skull model being analysed

With the the set of features defined, a total of 27 combinations of testing features (numbered from t0 to t26) were used. We will refer to each of these combinations as a criteria of selection (COS). Some of the selected criteria were designed to observe the amount of variation in the CFR results when they are taken to extreme values (for example,

$$A_1 = \{sex_1, sex_2\}$$
$$A_2 = \{age_1, age_2, age_3, age_4, age_5\}$$
$$A_3 = \{pca_1, pca_2, pca_3, pca_4, pca_5\}$$
$$A_4 = \{pro_1, pro_2, pro_3, pro_4, pro_5\}$$
$$A_5 = \{tvol_1, tvol_2, tvol_3, tvol_4, tvol_5\}$$

Figure 7.1: Auxiliar sets needed for applying the selection operator Sc for the experiments.

to observe what happens in the results when the system is given wrong feature values as input deliberately). In the next subsection, a standard set notation is described to define each criteria tested in the experiments.

7.1.1 Notation used

Let M be a n-ary domain $M = M_1 \times M_2 \ldots \times M_n$, and let $C : M \rightarrow \{T, F\}$ be a condition (predicate) on elements (n-tuples) of M (T and F represent a true or false value). Then, a selection operator S_c is the operator that maps any (n-ary) relation R on M to the n-ary relation of all n-tuples from R that satisfy C. i.e. $\forall R \subseteq M$, $S_c(R) = \{m \in R \mid Sc(M) = T\}$. In our particular case, M is the set of indexed head models $M = \{m_1 \ldots m_n\}$ in the database. H will represent the set of all the head models with their specific features contained in the database. In other words, H will be our universal set consisting of n head models with k specific features associated with each skull with the following structure:

$$H = \{(m_i, f_{ij}) \colon i \in \{1...n\},\ j \in \{1...k\},\ m_i \in M,\ f_{ij} \in \bigcup_{\alpha=1}^{\alpha=5} A_\alpha, S_c(H)\}$$

with S_c defining the appropriate feature combination known for each particular individual in the database. The sets A_α of possible attributes (or features) for each skull are shown in figure 7.1.

The following set definitions $S_i \subset S_0$, $i \in \{1...5\}$ are used to define the set partitioning M into disjoint classes with respect to specific feature values contained in sets A_α presented in table 7.2.

Set definition:	Head models classified by
$S_1 = \{(m, f) \colon m \in M,\ f \in A_1\} \cap H$	Sex
$S_2 = \{(m, f) \colon m \in M,\ f \in A_2\} \cap H$	Age Band
$S_3 = \{(m, f) \colon m \in M,\ f \in A_3\} \cap H$	PCA clustering
$S_4 = \{(m, f) \colon m \in M,\ f \in A_4\} \cap H$	Procrustes distances
$S_5 = \{(m, f) \colon m \in M,\ f \in A_5\} \cap H$	Tissue volume

Table 7.2: Auxiliar sets needed for apply the selection operator Sc for the experiments. Each of the sets Si represents a different partition of the set H.

The sets S_i are the mechanism for conducting the selection of different models with matching criteria for each reconstructed unknown skull, which is key aspect for creating the head template in the reconstruction process.

Test	Feature criteria	Set definition for the template
t_0	All the database (the universal set)	$T_0 = H$
t_1	Sex	$T_1 = \{(m, f)\colon (m, f) \in S_1,\ f = s_u\}$
t_2	Age band	$T_2 = \{(m, f)\colon (m, f) \in S_2,\ f = a_u\}$
t_3	PCA band	$T_3 = \{(m, f)\colon (m, f) \in S_3,\ f = p_u\}$
t_4	$Proc$ distance	$T_4 = \{(m, f)\colon (m, f) \in S_4,\ f = r_u\}$
t_5	BMI band	$T_5 = \{(m, f)\colon (m, f) \in S_5,\ f = v_u\}$
t_6	Sex & Age	$T_6 = \{(m, f)\colon (m, f) \in T_1 \cap T_2\}$
t_7	Sex & Age & PCA	$T_7 = \{(m, f)\colon (m, f) \in T_6 \cap T_3\}$
t_8	Sex & Age & $Proc$	$T_8 = \{(m, f)\colon (m, f) \in T_6 \cap T_4\}$
t_9	Sex & Age & BMI	$T_9 = \{(m, f)\colon (m, f) \in T_6 \cap T_5\}$
t_{10}	Sex & Age & PCA & BMI	$T_{10} = \{(m, f)\colon (m, f_1) \in T_7 \cap T_5\}$
t_{11}	Sex & Age & $Proc$ & BMI	$T_{11} = \{(m, f)\colon (m, f_1) \in T_8 \cap T_5\}$
t_{12}	$\overline{Sex}$	$T_{12} = \overline{T_1}$
t_{13}	$\overline{Age}$	$T_{13} = \{(m, f)\colon (m, f) \in S_2,\ f = O_a(f)\}$
t_{14}	$\overline{PCA}$	$T_{14} = \overline{T_3}$
t_{15}	$\overline{Proc}$	$T_{15} = \overline{T_4}$
t_{16}	$\overline{BMI}$	$T_{16} = \{(m, f)\colon (m, f) \in S_5,\ f = O_v(f)\}$
t_{17}	$\overline{Sex}$ & $\overline{Age}$	$T_{17} = T_{12} \cap T_{13}$
t_{18}	$\overline{Sex}$ & $\overline{Age}$ & PCA	$T_{18} = T_{17} \cap T_3$
t_{19}	$\overline{Sex}$ & $\overline{Age}$ & $Proc$	$T_{19} = T_{17} \cap T_4$
t_{20}	$\overline{Sex}$ & $\overline{Age}$ & $\overline{PCA}$	$T_{20} = T_{17} \cap T_{14}$
t_{21}	$\overline{Sex}$ & $\overline{Age}$ & $\overline{Proc}$	$T_{21} = T_{17} \cap T_{15}$
t_{22}	$\overline{Sex}$ & $\overline{Age}$ & $\overline{BMI}$	$T_{22} = T_{17} \cap T_{16}$
t_{23}	$\overline{Sex}$ & $\overline{Age}$ & PCA & $\overline{BMI}$	$T_{23} = T_{17} \cap T_3 \cap T_{16}$
t_{24}	$\overline{Sex}$ & $\overline{Age}$ & $Proc$ & $\overline{BMI}$	$T_{24} = T_{17} \cap T_4 \cap T_{16}$
t_{25}	$\overline{Sex}$ & $\overline{Age}$ & $\overline{PCA}$ & $\overline{BMI}$	$T_{25} = T_{20} \cap T_{16}$
t_{26}	$\overline{Sex}$ & $\overline{Age}$ & $\overline{Proc}$ & $\overline{BMI}$	$T_{25} = T_{21} \cap T_{16}$

Table 7.3: Different criteria used for the experiments. In this table it is presented the logical rules for defining each of the 27 criteria used in the experiment (right column)

Age and volume tissue group definition

Table 7.3 presents the definition of the 27 criteria used. In this table, m represents the index of head models in the database, f represents a particular feature value, and the specific features of the unknown skull namely sex, age band, pca group, procrustes group, and tissue volume group are represented with the letters s_u, a_u, p_u, r_u and v_u respectively.

For the *age* feature, the models in the database were grouped in band ages as presented in table 7.1.

The feature *vol* refers to the soft-tissue volume present in each head model, and we assume that it is directly proportional to the BMI index value of the individual. This variable is calculated using the difference between the volume of the face model and the skull model. The opposite bands for age and volume are calculated using the O_a and O_v operators:

$$O_a(a_u) = \begin{cases} age_4 \ if \ (a_u \in \{age_0, age_1, age_2\}), \\ age_0 \qquad\qquad\qquad\qquad \text{otherwise} \end{cases}$$

$$O_v(v_u) = \begin{cases} vol_4 \ if \ (v_u \in \{vol_0, vol_1, vol_2\}), \\ vol_0 \qquad\qquad\qquad\qquad \text{otherwise} \end{cases}$$

For example considering the COS presented in table 7.3, the COS 9 (t9) uses the sex, age and BMI features of the unknown skull to select a set of head models with the same (or similar features) to create a template. The criterion of selection 16 (t16) uses a set of head models with different BMI features to the unknown skull (e.g. if the unknown skull is from a slim person then, a selection of overweight subjects are used to create the template). COS 17 (t17) uses opposite sex and different range of age subjects for creating the skull template (e.g. if the unknown skull belongs to a person young and male, the models used for creating the skull template are chosen older and females).

7.2 Experiments using the criteria

The database used for this experiment contains 40 head models. These models belong to 20 male and 20 female subjects. For exploring the capabilities of the craniofacial reconstruction system, the faces of their 40 skull models were estimated. The head models were grouped according to five biological and geometric characteristics. In the first group, biological features such as sex, age band, and body build were considered. For the second category, geometric measures such as PCA coefficients [44] and geometric distance were used.

A leave-one-out test was conducted for each head model of the database. The skull of a selected head model is used to simulate an unknown skull. This skull is used as the input for the craniofacial reconstruction system. Then, a set of possible faces for that skull model is produced using different criteria.

From the analysis of the unknown skull a set of features is obtained and used in the selection of the head models from the database. That selection is used to create the head template. The strategy for conducting the tests is based on defining different COS for each test. The general approach for the experiments was to start with few criteria used in choosing the models. Then add more criteria and compare the results. The question we wanted to address was if this incremental approach will produce better reconstructions in terms of surface similarity distances.

A total of 27 criteria were tested for each skull, and the results were assessed comparing the average difference between the reconstructed face and the real face known from the head model (quantitative surface to surface comparison). The definition of these criteria was presented in section 7.1. A total of 850 reconstructions were possible combining the different features and the number of individuals for each category. The distribution of the models involved in this experiments are shown in figure 7.1.

7.3 Results

The results of the comparison between the reconstructed facial surface and the real face surface are evaluated by comparing the average difference between the surfaces. As an example, figure 7.2 shows the best reconstruction for the skull of subject 18 of the UOS dataset. This reconstruction has the lower average distance between surfaces and it was obtained using criterion t6 (i.e. selecting models of individuals of the same sex and similar age than the unknown skull). Figure 7.3 shows an example of the results for the same skull based on COS t0-t5.

Table 7.4 presents the average difference between real and reconstructed faces. Table 7.5 gives the Root Mean Squared (RMS) a statistical measure of the magnitude of the average differences. A graph, showing the histogram of the differences, to show the distribution of the average differences, is presented in figure 7.4. This graph, shows the "normality" of the difference distribution of the results which is useful to describe the type of variable we are analysing. Appendix D presents a description of the main terms involved in the analysis of variance.

Analysis of variance (ANOVA) is used to test hypotheses about differences between means. This analysis is a family of multivariate statistical techniques for inferring whether there are real differences between the means of three or more groups or variables in a population, based on sample data. The results of the ANOVA analysis for the average differences of each COS tested are presented in table 7.8.

A one-way between groups analysis of variance was conducted to explore the impact of including sex, age, body build and geometric information on the results of a craniofacial reconstruction, in a correct (t0-t11 criteria) and incorrect way (t12-t26 criteria)[1]. Subject facial reconstructions were divided into 27 groups using combinations of these features as presented in the previous section. There was a statistically significant difference at the $p < 0.05$ level in reconstructions scores for the 27 criteria tested: $F(26, 823) = 6.528$, $p < 0.001$. Despite reaching statistical significance, the actual difference in mean scores between the groups was quite small.

Post-hoc comparisons using the Tukey HSD method [79] indicate that the mean scores for a first group of CFR (t0, t1, t2, t3, t4, t5, t6) were significantly different from a second group of CFR (t16, t18, t20, t21, t22, t24, t25, t26). A third group of CFR criteria tested (t7, t8, t9, t10, t11, t12, t13, t14, t15) did not differ significantly from any CFR test in either the first or second groups. Table 7.6 shows the values describing the mean variation for each test. Table 7.7 presents the values of the mean distributions sorted in terms of similarity between groups. This sorting is used to determine which groups are related between each other.

Descriptive statistics shows that there were higher differences between the real and reconstructed face made with criteria in the second group with higher indices than in the

[1] in this context "correct" means using the same or similar features between the unknown skull subject and the head model subjects selected from the database. Incorrect means using different features.

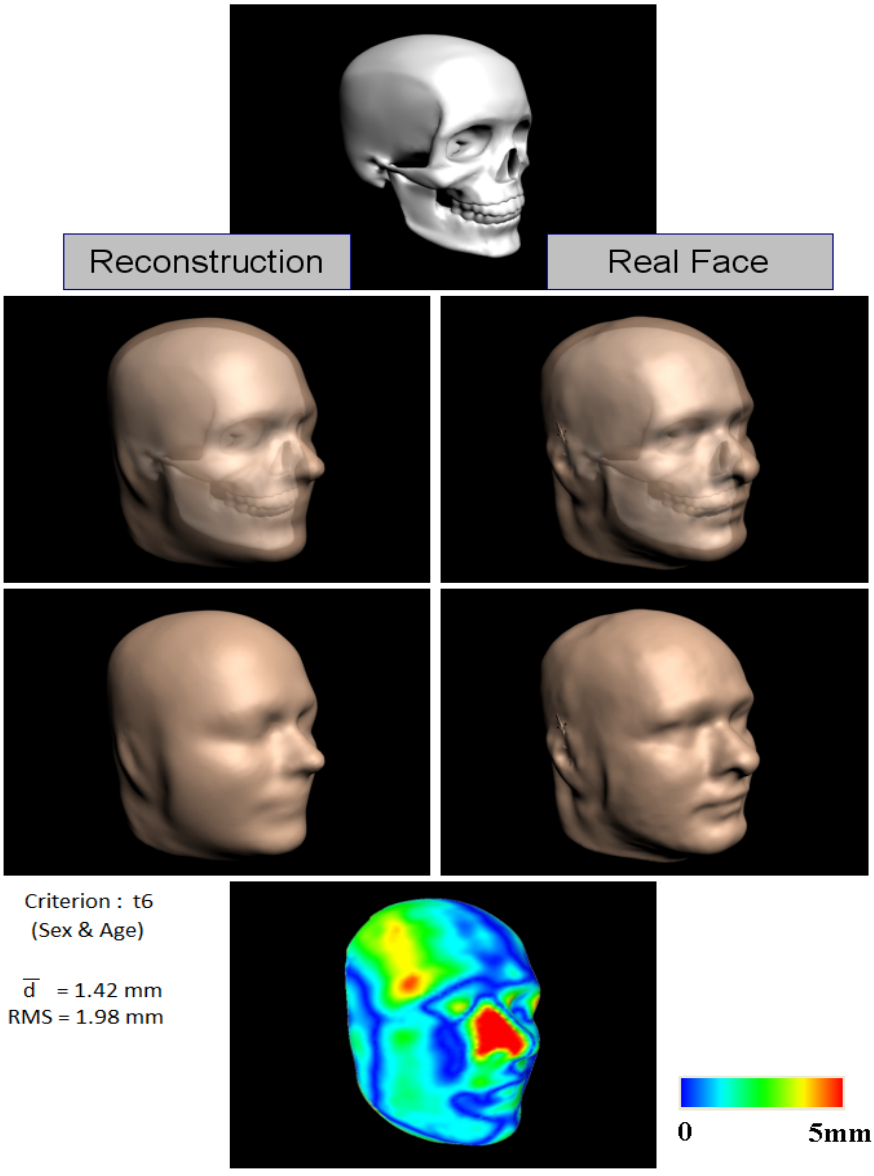

Figure 7.2: An example of the best reconstruction for skull model 18 of the UOS dataset (corresponding to model index 13 of the experiments). The best reconstruction score was obtained applying criterion t6 based on sex and age.

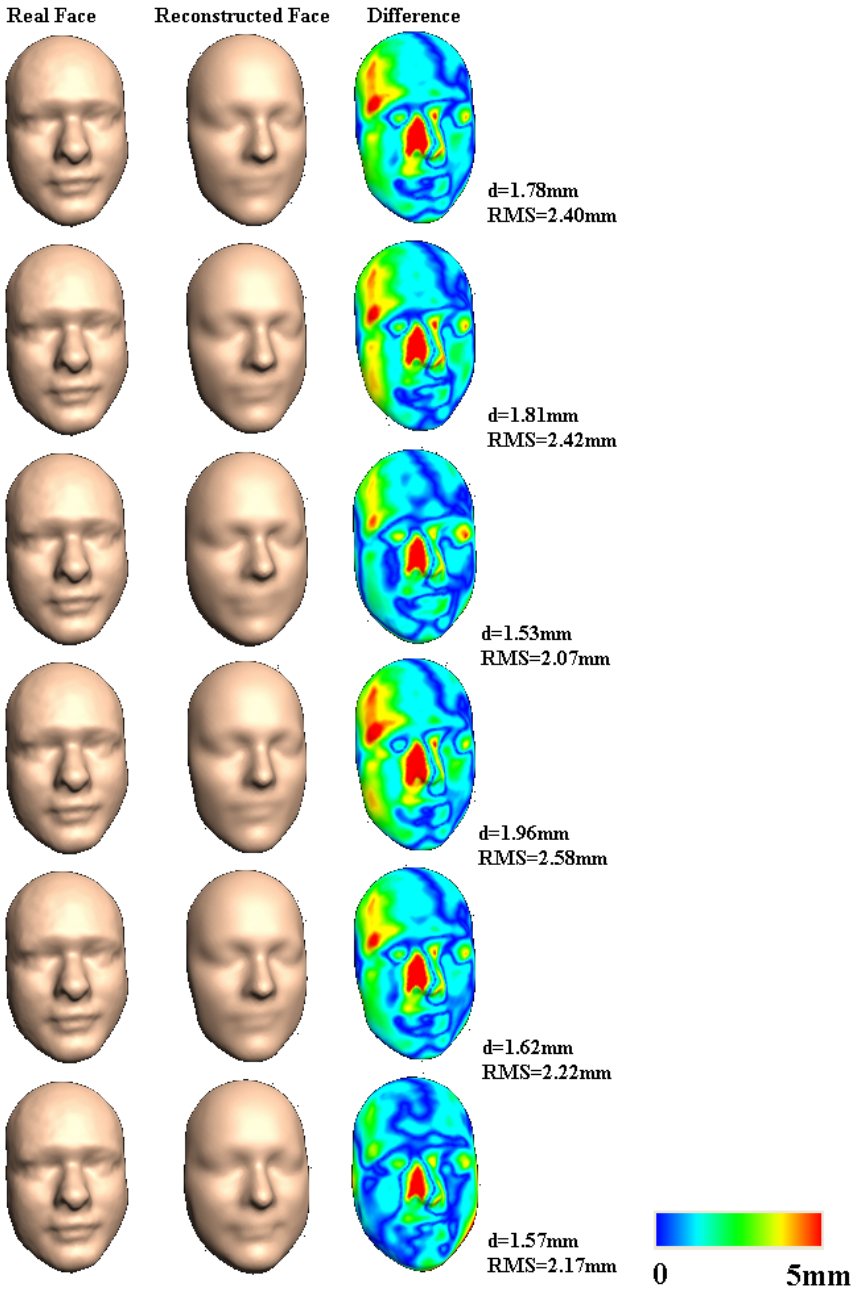

Figure 7.3: An example of the several outputs of the CFR system for the skull of the subject 18 of the UOS dataset. Each row represents a criteria for the reconstruction (t0-t5). The complete set of reconstruction for this skull can be found in table 7.4 row number 13.

	t0	t1	t2	t3	t4	t5	t6	t7	t8	t9	t10	t11	t12	t13	t14	t15	t16	t17	t18	t19	t20	t21	t22	t23	t24	t25	t26
1	1.70	1.65	1.59	1.42	1.41	2.02	2.15	2.15	2.39	0.00	0.00	0.00	1.84	1.58	1.95	1.73	1.47	2.04	1.62	0.00	2.57	2.04	3.27	0.00	0.00	3.27	3.27
2	1.90	1.61	2.00	1.99	1.83	1.92	1.60	1.76	1.48	1.60	0.00	1.60	2.19	2.08	1.86	1.95	2.29	2.43	0.00	2.46	2.43	2.70	2.46	0.00	2.46	2.46	0.00
3	3.55	3.43	3.29	3.01	3.29	2.69	2.02	2.02	2.02	0.00	0.00	0.00	3.68	3.16	3.86	3.82	4.20	3.44	2.12	2.12	4.13	4.13	0.00	0.00	0.00	0.00	0.00
4	2.56	2.45	2.54	2.08	2.24	2.58	2.52	0.00	2.53	1.93	0.00	1.90	2.72	2.95	2.86	2.83	1.57	3.12	2.55	2.38	3.59	3.44	0.00	0.00	0.00	0.00	0.00
5	1.81	1.68	1.83	1.82	1.50	1.97	1.60	1.80	1.60	1.53	0.00	1.53	1.99	2.22	1.89	1.95	2.41	2.50	2.90	0.00	2.63	2.50	2.53	0.00	0.00	2.53	2.53
6	2.08	2.25	2.66	1.68	1.82	2.20	2.88	2.57	2.69	0.00	0.00	0.00	2.01	1.85	2.37	2.47	2.75	1.75	1.49	1.61	2.07	2.77	2.97	0.00	2.97	2.97	0.00
7	1.93	2.07	1.83	2.45	1.94	1.91	2.00	0.00	0.00	0.00	0.00	0.00	1.91	1.98	1.95	1.99	2.43	1.97	2.88	2.22	1.93	1.99	0.00	0.00	0.00	0.00	0.00
8	1.84	1.73	2.15	1.83	1.83	3.21	2.36	0.00	2.89	0.00	0.00	0.00	2.01	1.75	1.86	1.88	1.85	1.91	0.00	1.99	1.91	1.95	1.97	0.00	2.20	1.97	1.94
9	1.68	1.69	1.78	1.69	2.79	1.50	1.89	0.00	0.00	1.74	0.00	0.00	1.76	2.15	1.68	1.65	2.53	2.20	0.00	2.95	2.20	2.21	2.10	0.00	0.00	2.10	2.10
10	3.28	3.14	2.99	2.75	3.19	3.34	2.09	2.09	1.93	0.00	0.00	0.00	3.41	3.00	3.57	3.46	2.56	3.42	2.50	3.32	4.00	3.86	4.44	0.00	4.44	4.44	0.00
11	2.07	2.23	1.84	1.79	1.76	2.13	2.57	0.00	3.09	2.57	0.00	0.00	2.01	2.54	2.32	2.59	2.84	2.73	2.87	2.68	2.53	2.78	2.74	2.87	2.68	2.39	2.80
12	1.28	1.20	1.26	1.27	1.25	1.38	1.18	1.64	1.16	1.41	0.00	1.41	1.48	1.54	1.32	1.35	1.93	1.73	1.72	1.69	1.99	2.05	0.00	0.00	0.00	0.00	0.00
13	1.78	1.81	1.53	1.96	1.62	1.57	1.42	2.64	1.42	1.91	2.64	1.91	1.86	2.10	1.72	2.10	2.35	2.32	2.27	2.23	2.41	2.46	2.27	2.11	2.17	2.36	2.42
14	1.92	1.71	1.71	1.85	1.97	1.97	1.45	1.68	1.95	1.26	0.00	1.68	2.19	2.18	1.97	1.93	3.10	2.34	2.37	0.00	2.48	2.34	0.00	0.00	0.00	0.00	0.00
15	1.56	1.38	1.49	1.52	1.59	1.62	2.46	0.00	2.46	2.46	0.00	2.46	1.79	1.70	1.61	1.56	2.75	1.90	1.86	1.88	2.20	2.29	0.00	0.00	0.00	0.00	0.00
16	1.24	1.13	1.37	1.54	1.23	1.16	1.30	1.37	1.11	1.95	1.79	1.61	1.48	1.51	1.26	1.31	2.10	1.64	2.57	0.00	1.63	1.64	0.00	0.00	0.00	0.00	0.00
17	1.76	1.89	1.30	2.22	1.66	1.17	1.35	2.38	1.91	1.22	0.00	1.62	1.77	2.24	1.67	1.84	2.57	2.46	0.00	0.00	2.46	2.46	2.50	0.00	0.00	2.50	2.50
18	1.30	1.15	1.43	1.11	1.13	1.38	1.21	0.00	1.46	1.43	0.00	1.43	1.57	1.36	1.39	1.56	2.22	1.62	2.29	1.48	1.61	3.00	0.00	0.00	0.00	0.00	0.00
19	1.38	1.28	1.38	1.39	1.21	1.49	1.33	1.32	1.44	0.00	0.00	0.00	1.58	1.56	1.41	1.49	1.66	1.84	0.00	1.65	1.84	2.15	0.00	0.00	0.00	0.00	0.00
20	1.06	1.26	1.41	1.04	0.94	1.13	1.46	1.80	1.33	1.75	0.00	0.00	1.07	1.04	1.13	1.22	1.78	1.11	1.94	1.94	1.41	1.41	1.94	1.94	1.94	0.00	0.00
21	2.00	1.78	1.95	2.19	2.03	1.75	1.74	0.00	0.00	2.25	0.00	0.00	2.25	2.25	2.02	2.02	2.60	2.74	0.00	0.00	2.74	2.74	2.66	0.00	0.00	2.66	2.66
22	1.36	1.37	1.43	1.49	1.39	1.37	1.34	1.34	1.42	1.38	1.44	1.42	1.48	1.72	1.44	1.44	1.92	1.83	2.47	2.47	2.03	2.03	1.96	0.00	0.00	1.96	1.96
23	1.22	1.27	1.17	1.52	1.29	1.03	1.13	1.21	1.19	1.06	1.27	1.04	1.40	1.69	1.29	1.21	2.19	1.90	2.49	1.80	2.15	2.53	2.27	0.00	2.27	2.27	0.00
24	1.60	1.42	1.47	1.29	1.36	1.64	0.00	0.00	0.00	0.00	0.00	0.00	1.83	2.02	1.85	1.79	1.40	2.28	1.84	1.75	2.69	2.57	0.00	0.00	0.00	0.00	0.00
25	1.84	1.94	2.40	1.93	1.88	1.88	1.77	1.77	1.98	0.00	0.00	0.00	1.85	2.28	1.84	1.84	2.86	2.31	2.36	2.43	2.47	2.64	0.00	0.00	0.00	0.00	0.00
26	3.07	3.36	2.80	3.44	3.04	2.26	3.01	2.78	3.32	2.46	2.78	2.78	2.78	3.49	2.92	3.09	3.68	3.42	3.23	3.37	3.54	3.55	3.54	3.27	3.48	3.65	3.55
27	1.85	1.92	2.14	2.26	1.91	1.85	2.25	0.00	0.00	1.72	0.00	0.00	1.85	1.72	1.73	1.84	2.50	2.00	2.64	0.00	2.19	2.00	2.49	0.00	0.00	2.49	2.49
28	1.29	1.12	1.76	1.29	1.32	1.36	1.59	1.59	0.00	0.00	0.00	0.00	1.53	1.47	1.31	1.35	1.68	1.69	1.54	1.75	1.96	1.89	1.73	1.73	1.73	0.00	0.00
29	1.73	1.92	2.39	1.45	1.45	1.67	2.85	0.00	2.85	2.85	0.00	2.85	1.70	1.82	2.02	1.87	1.87	1.78	2.20	2.04	1.92	1.80	2.23	0.00	0.00	0.00	0.00
30	0.94	0.89	0.96	1.01	1.01	1.02	0.99	1.65	1.09	1.08	0.00	1.09	1.22	1.25	0.95	0.98	1.83	1.67	0.00	0.00	1.67	1.67	2.04	0.00	0.00	2.04	2.04
31	2.10	1.95	2.12	2.49	2.26	2.10	1.96	0.00	2.74	1.75	0.00	0.00	2.30	2.46	2.01	2.04	1.81	2.59	2.57	2.18	2.62	3.21	0.00	0.00	0.00	0.00	0.00
32	1.30	1.26	1.06	1.92	1.53	1.42	1.27	1.91	1.52	1.45	1.43	1.43	1.50	1.76	1.10	0.97	2.49	1.95	3.21	2.07	1.77	2.11	0.00	0.00	0.00	0.00	0.00
33	1.53	1.52	1.35	1.85	2.29	1.07	1.40	1.40	2.16	1.16	1.23	0.00	1.67	2.00	1.53	1.52	2.50	2.20	2.85	0.00	2.29	2.20	2.35	0.00	0.00	2.35	2.35
34	1.70	1.48	2.62	1.56	1.71	1.94	2.63	2.21	3.01	0.00	0.00	0.00	1.98	1.42	1.77	1.73	1.61	1.90	0.00	2.20	1.90	1.80	1.78	0.00	1.91	1.78	1.78
35	2.28	2.39	2.11	2.38	2.65	1.90	2.28	2.57	0.00	1.91	2.57	0.00	2.24	2.73	2.27	2.27	3.25	2.77	2.56	0.00	3.18	2.77	2.56	2.56	0.00	0.00	2.56
36	1.50	1.57	1.74	1.46	1.59	1.62	1.99	2.17	2.35	0.00	0.00	0.00	1.52	1.50	1.54	1.50	2.41	1.57	1.82	1.66	1.55	1.84	0.00	0.00	0.00	1.24	0.00
37	2.29	2.14	1.99	2.13	1.81	2.51	2.02	0.00	2.09	1.71	0.00	0.00	2.49	2.56	2.32	2.38	3.47	2.81	2.66	2.66	2.99	2.99	0.00	0.00	0.00	0.00	0.00
38	1.23	1.41	1.36	1.36	1.21	1.51	1.36	1.66	1.25	2.23	2.68	0.00	1.25	1.44	1.24	1.31	2.11	1.49	2.06	2.06	1.68	1.68	2.06	2.06	2.06	0.00	0.00
39	1.75	1.62	1.47	2.00	1.63	1.81	1.44	2.33	1.49	1.53	0.00	1.71	1.96	2.22	1.66	2.07	1.04	2.46	2.78	2.07	2.35	3.04	0.00	0.00	0.00	0.00	0.00
40	1.64	1.49	2.57	1.53	1.72	1.78	1.45	1.45	1.87	0.00	0.00	0.00	1.85	1.93	1.70	1.57	2.75	2.17	2.02	2.31	2.45	2.25	0.00	0.00	0.00	0.00	0.00

Table 7.4: Results of the average differences (mm) between the real face and the reconstructed face. The columns represent the 27 criteria tested and each row corresponds to the index of the model tested. The cells with 0.00 values represent cases where it was not possible to have enough models to meet the selected criterion.

	t0	t1	t2	t3	t4	t5	t6	t7	t8	t9	t10	t11	t12	t13	t14	t15	t16	t17	t18	t19	t20	t21	t22	t23	t24	t25	t26
1	2.30	2.23	2.25	2.04	1.94	2.63	3.11	3.11	3.14	0.00	0.00	0.00	2.52	2.27	2.59	2.36	2.15	2.84	2.51	0.00	3.42	2.84	4.08	0.00	0.00	4.08	4.08
2	2.45	2.21	2.60	2.58	2.37	2.46	2.26	2.37	2.22	2.28	0.00	2.28	2.78	2.65	2.42	2.52	2.96	3.03	0.00	3.06	3.03	3.45	3.06	0.00	3.06	3.06	0.00
3	4.44	4.23	4.19	3.79	4.14	3.54	2.64	2.64	2.64	0.00	0.00	0.00	4.66	4.08	4.81	4.74	5.09	4.53	3.10	3.10	5.29	5.29	0.00	0.00	0.00	0.00	0.00
4	3.39	3.21	3.42	2.83	3.09	3.51	3.35	0.00	3.42	2.77	0.00	2.80	3.61	3.79	3.74	3.66	2.27	4.04	3.33	3.04	4.69	4.53	0.00	0.00	0.00	0.00	0.00
5	2.33	2.12	2.49	2.28	1.89	2.64	2.08	2.30	2.14	2.19	0.00	2.19	2.63	2.78	2.50	2.53	2.93	3.15	3.57	0.00	3.34	3.15	3.10	0.00	0.00	3.10	3.10
6	2.62	2.86	3.25	2.10	2.30	2.90	3.59	3.26	3.38	0.00	0.00	0.00	2.51	2.46	2.98	3.07	3.35	2.31	1.88	2.08	2.76	3.86	3.69	0.00	3.69	3.69	0.00
7	2.57	2.78	2.58	3.13	2.53	2.48	2.80	0.00	0.00	0.00	0.00	0.00	2.50	2.57	2.60	2.66	3.42	2.45	3.64	2.74	2.42	2.51	0.00	0.00	0.00	0.00	0.00
8	2.31	2.21	2.68	2.26	2.28	4.05	2.93	0.00	3.64	0.00	0.00	0.00	2.53	2.19	2.36	2.40	2.34	2.40	0.00	2.52	2.40	2.46	2.52	0.00	2.86	2.52	2.48
9	2.29	2.18	2.47	2.18	3.39	2.04	2.65	0.00	0.00	2.35	0.00	0.00	2.54	2.80	2.29	2.29	3.07	3.00	0.00	3.63	3.00	3.10	2.90	0.00	0.00	2.90	2.90
10	4.23	3.95	3.86	3.62	4.11	4.36	3.02	3.02	2.69	0.00	0.00	0.00	4.52	4.16	4.58	4.49	3.43	4.69	3.68	4.38	5.31	5.57	5.47	0.00	5.47	5.47	0.00
11	2.61	2.82	2.36	2.33	2.31	2.72	3.28	0.00	3.85	3.38	0.00	0.00	2.54	3.09	2.89	3.17	3.45	3.28	3.43	3.26	3.14	3.37	3.32	3.48	3.26	3.00	3.49
12	1.60	1.49	1.62	1.58	1.57	1.80	1.53	2.35	1.46	1.95	0.00	1.95	1.89	1.90	1.65	1.71	2.47	2.14	2.12	2.15	2.47	2.51	0.00	0.00	0.00	0.00	0.00
13	2.40	2.42	2.07	2.58	2.22	2.17	1.98	3.39	1.98	2.45	3.39	2.45	2.52	2.75	2.35	2.76	3.07	3.01	3.02	2.83	3.12	3.24	3.00	2.96	2.86	3.08	3.24
14	2.69	2.39	2.39	2.64	2.90	2.85	1.99	2.38	2.76	1.72	0.00	2.39	3.06	2.86	2.74	2.64	4.08	3.16	3.08	0.00	3.44	3.16	0.00	0.00	0.00	0.00	0.00
15	1.89	1.68	1.88	1.81	1.91	1.98	3.15	0.00	3.15	3.15	0.00	3.15	2.24	2.12	1.96	1.92	3.29	2.36	2.31	2.31	2.73	2.82	0.00	0.00	0.00	0.00	0.00
16	1.58	1.42	1.71	1.96	1.57	1.50	1.68	1.73	1.40	2.43	2.21	1.99	1.92	1.97	1.63	1.70	2.60	2.21	3.57	0.00	2.19	2.21	0.00	0.00	0.00	0.00	0.00
17	2.23	2.40	1.71	2.77	2.11	1.49	1.76	3.00	2.41	1.55	0.00	2.03	2.22	2.78	2.12	2.34	3.19	3.02	0.00	0.00	3.02	3.02	3.09	0.00	0.00	3.09	3.09
18	1.93	1.77	2.02	1.72	1.71	1.98	1.72	0.00	1.96	2.01	0.00	2.01	2.24	1.89	2.02	2.29	2.99	2.16	3.09	1.98	2.11	3.93	0.00	0.00	0.00	0.00	0.00
19	1.67	1.58	1.74	1.78	1.50	1.79	1.69	1.63	1.83	0.00	0.00	0.00	1.92	1.92	1.69	1.80	2.07	2.29	0.00	2.11	2.29	2.62	0.00	0.00	0.00	0.00	0.00
20	1.48	1.75	1.91	1.39	1.33	1.52	1.96	2.34	1.81	2.41	0.00	0.00	1.46	1.41	1.56	1.70	2.36	1.51	2.41	2.41	1.85	1.85	2.41	2.41	2.41	0.00	0.00
21	2.60	2.31	2.52	3.02	2.61	2.34	2.44	0.00	0.00	2.95	0.00	0.00	2.94	2.82	2.62	2.62	3.30	3.44	0.00	0.00	3.44	3.44	3.37	0.00	0.00	3.37	3.37
22	1.72	1.66	1.96	1.77	1.67	1.93	1.75	1.81	1.97	1.95	2.10	1.97	1.97	2.16	1.92	1.89	2.33	2.43	2.95	2.95	2.76	2.76	2.66	0.00	0.00	2.66	2.66
23	1.80	1.84	1.60	2.19	1.91	1.43	1.63	1.69	1.76	1.49	1.70	1.57	1.96	2.31	1.80	1.63	2.91	2.53	3.27	2.47	2.71	3.30	2.88	0.00	2.88	2.88	0.00
24	2.15	1.96	1.89	1.71	1.77	2.15	0.00	0.00	0.00	0.00	0.00	0.00	2.43	2.59	2.49	2.46	1.67	3.00	2.26	2.13	3.71	3.50	0.00	0.00	0.00	0.00	0.00
25	2.54	2.74	2.96	2.72	2.54	2.78	2.69	2.69	2.96	0.00	0.00	0.00	2.49	3.01	2.50	2.59	3.52	3.04	3.14	3.15	3.21	3.59	0.00	0.00	0.00	0.00	0.00
26	3.73	4.15	3.48	4.15	3.72	2.84	3.75	3.52	4.16	3.06	3.52	3.52	3.37	4.17	3.56	3.73	4.38	4.03	3.80	4.01	4.20	4.17	4.19	3.87	4.28	4.32	4.17
27	2.49	2.71	2.68	3.16	2.67	2.45	2.77	0.00	0.00	2.33	0.00	0.00	2.44	2.37	2.26	2.43	3.35	2.64	3.55	0.00	2.75	2.64	3.15	0.00	0.00	3.15	3.15
28	1.62	1.43	2.30	1.61	1.68	1.77	2.06	2.06	0.00	0.00	0.00	0.00	1.95	1.85	1.66	1.70	2.10	2.16	2.04	2.30	2.53	2.46	2.34	2.34	2.34	0.00	0.00
29	2.45	2.71	3.04	2.06	2.07	2.38	3.59	0.00	3.59	3.59	0.00	3.59	2.32	2.61	2.76	2.63	2.50	2.53	3.02	2.94	2.73	2.50	2.95	0.00	0.00	0.00	0.00
30	1.18	1.12	1.19	1.30	1.23	1.29	1.28	2.25	1.37	1.34	0.00	1.37	1.48	1.58	1.19	1.25	2.34	2.05	0.00	0.00	2.05	2.05	2.56	0.00	0.00	2.56	2.56
31	2.58	2.44	2.52	3.07	2.78	2.60	2.38	0.00	3.51	2.25	0.00	0.00	2.83	3.05	2.48	2.50	2.30	3.27	3.42	2.70	3.29	4.15	0.00	0.00	0.00	0.00	0.00
32	1.60	1.58	1.42	2.29	1.84	1.74	1.68	2.29	1.84	1.97	1.78	1.78	1.82	2.08	1.38	1.26	2.96	2.28	3.97	2.51	2.08	2.56	0.00	0.00	0.00	0.00	0.00
33	2.01	2.06	1.76	2.43	2.93	1.38	1.82	1.81	2.82	1.53	1.62	0.00	2.14	2.57	1.96	1.97	3.20	2.79	3.61	0.00	2.87	2.79	2.94	0.00	0.00	2.94	2.94
34	2.11	1.88	3.29	1.98	2.14	2.50	3.36	2.87	3.81	0.00	0.00	0.00	2.45	1.79	2.18	2.13	2.00	2.36	0.00	2.73	2.36	2.26	2.21	0.00	2.41	2.21	2.23
35	2.80	2.85	2.65	3.01	3.12	2.41	2.91	3.31	0.00	2.55	3.44	0.00	2.85	3.30	2.77	2.79	3.93	3.46	3.31	0.00	3.91	3.46	3.31	3.31	0.00	0.00	3.31
36	2.02	2.21	2.31	1.95	2.15	2.16	2.61	2.82	3.02	0.00	0.00	0.00	2.02	1.95	2.08	1.95	3.13	2.03	2.35	2.13	2.00	2.42	0.00	0.00	0.00	1.71	0.00
37	3.18	2.92	2.86	2.74	2.45	3.43	2.72	0.00	2.76	2.36	0.00	0.00	3.50	3.38	3.23	3.30	4.45	3.71	3.40	3.40	3.95	3.95	0.00	0.00	0.00	0.00	0.00
38	1.84	2.15	1.87	1.84	1.78	2.08	1.86	2.25	1.68	3.03	3.46	0.00	1.74	1.96	1.89	1.99	2.96	2.02	2.73	2.73	2.26	2.26	2.73	2.73	2.73	0.00	0.00
39	2.12	2.05	1.88	2.41	1.98	2.23	1.96	2.93	1.90	2.01	0.00	2.48	2.31	2.68	2.02	2.51	1.35	2.89	3.37	2.44	2.74	3.67	0.00	0.00	0.00	0.00	0.00
40	2.04	1.86	3.27	1.89	2.14	2.21	2.11	2.11	2.79	0.00	0.00	0.00	2.34	2.45	2.13	1.96	3.41	2.76	2.55	2.91	3.14	2.94	0.00	0.00	0.00	0.00	0.00

Table 7.5: Results of the RMS differences (mm) between the real face and the reconstructed face. The columns represent the 27 criteria tested and each row corresponds to the index of the model tested. The cells with 0.00 values represent cases where it was not possible to have enough models to meet the selected criterion.

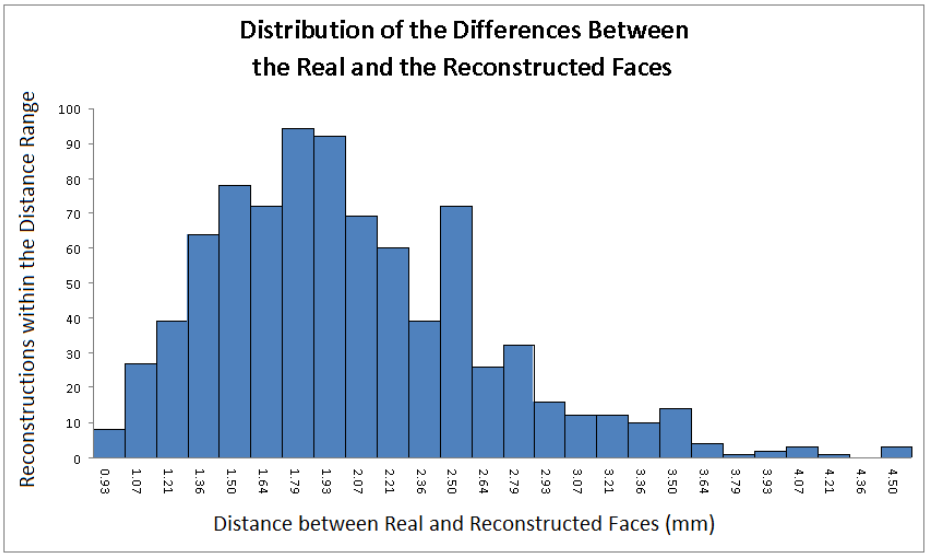

Figure 7.4: Histogram showing the distribution of the average distance between the reconstructed and the real face surfaces.

tests defined with lower indices.

The one-way analysis of variance showed that differences between several of these types of conditions were unlikely to have arisen by chance or sampling error, assuming the null hypothesis to be true with a significance level of 95%. Figure 7.5 shows the average means of the tests involved in the experiments.

For producing the data shown in table 7.4 the processing time was 3.5 hours on average per criteria. A total of 120 hours (approx.) were dedicated to produce the 850 facial reconstructions. The time varies depending on the amount of head templates used for the test [2].

7.4 Discussion

One of the aims of the experiments was to show the impact of using the new type of tissue depth data in our CFR system. The results suggest that, when using the database of head models produced in this thesis, it was possible to obtain face estimations with good levels of accuracy. The metric used was the average distance between the reconstructed and real faces. In our system, approximately 80% of the best reconstruction scores have less than 2.5 mm error and the remainder 20% have less than 3.5mm of error. These figures are, in terms of magnitude comparable with other computerised CFR systems using similar evaluation measurements (note: these systems do not use the same technique nor data but they are computer-based) reporting reconstruction errors around 2.5 mm [100, 110].

This study also sought to determine whether the results of the face reconstructions for different combination of features differed according to the amount and similarity of the features used. An incremental strategy was used for adding more features to the system and evaluating the average distance for each reconstruction. Some COS included subjects

[2] These results were obtained using a Dell Dimension DXP061 computer with two Intel(R) processors 6600 running at 2.4GHz and 2.0 GB of ram memory.

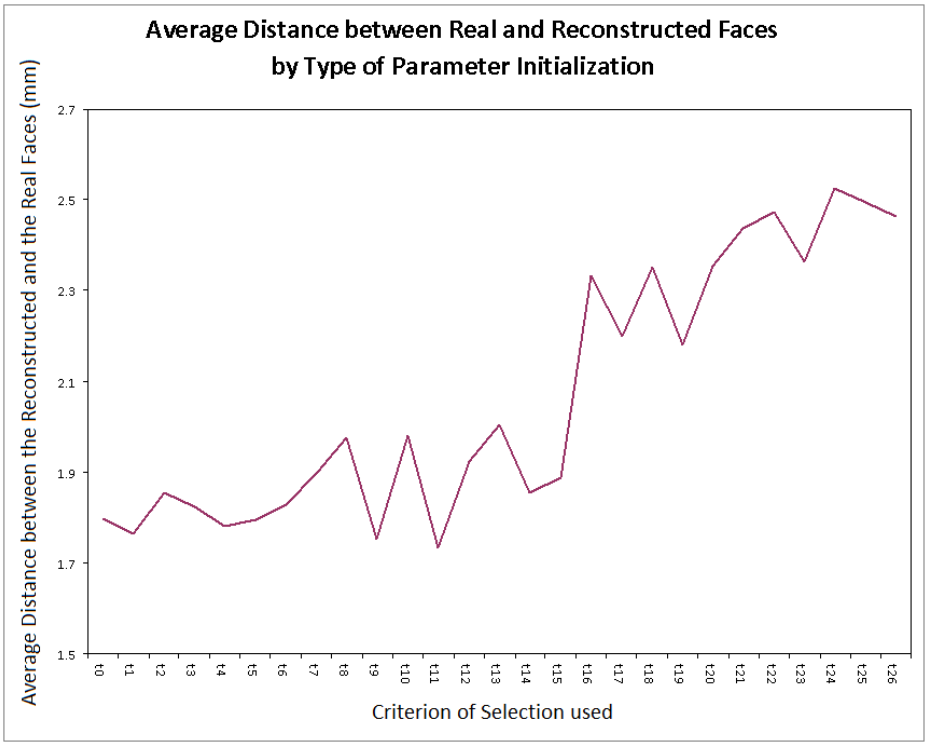

Figure 7.5: Plot of the mean differences for each test meeting the criteria.

with completely different features to the unknown skull being analysed. In some of the tests, by increasing the number of known features seems to improve the results of the reconstructions. For example from t6 (Sex & Age; $\bar{d} = 1.828$) to t9 (Sex & Age & BMI; $\bar{d} = 1.752$) and from t9 (Sex & Age & BMI; $\bar{d} = 1.752$) to t11 (Sex & Age & Proc & BMI; $\bar{d} = 1.734$) (see figure 7.5). However, from the ANOVA analysis, it was not possible to determine a significant difference in the results for the entire set of COS. For example, providing the system with the sex, age, PCA and BMI for a given skull has no significative difference to using only one feature such as sex or age.

One possible reason for this behaviour in the results can be explained by the size of the database. Some of the reconstructions could not be done because there were not enough models having the required COS. Another sets of reconstruction tests had a very limited number of subjects to produce the skull template. The difference between the means in the tests could be refined (better modelled) with more data. More data could lead to more precise and less variable mean behaviour of the average distances between tests impacting the ANOVA tests. The solution is to conduct more tests gathering more subject data containing feature variations representative to the desired population to model.

Another possible reason that can impact in the results is the method to combine different head models used. Currently this method is implemented as a simple linear combination of head models. The assumption that a human face can be derived from a linear combination of another face models is strong. However, when combined the head template estimated with the skull fitting process, the impact of the linear assumption is reduced. This is reflected in the magnitude of the average differences reported in the experiment results (less than 3.5mm for the best reconstruction scores). This assumption

was used as an initial way to test the feasibility of using the MRI generated database.

Figure 7.5 shows that even using the incorrect features t11-t26 the amount of error added in comparison to using the correct features is of a maximum of 0.5mm (approx). t9 and t11 have the best scores as expected (t9: criterion using the right sex, age and BMI for the COS, and t11 using the same sex, age, BMI and Procrustes distance as the COS for the template).

From the ANOVA analysis it was only possible to separate between two classes of COS: Those using the correct features with only one feature from those results produced by using any combination of incorrect features (i.e. COS t1-t6 from COS t16-t26 respectively).

One key aspect is that, even though the amount of data is small the results produced by this system are replicable, and consistent. And can be quantitatively evaluated. Even when the results of this experiment are not conclusive, this setting taken to a large scale can help to understand the main factors affecting the results of a craniofacial reconstruction system and improve the strategies for the algorithmic creation of face estimations at the surface level.

Test Label	N	Mean	Std Dev	Std Error	Lower Bound	Upper Bound	Min	Max
t0	40	1.798	0.560	0.089	1.618	1.977	0.940	3.550
t1	40	1.764	0.578	0.091	1.579	1.949	0.890	3.430
t2	40	1.856	0.558	0.088	1.678	2.034	0.960	3.290
t3	40	1.824	0.527	0.083	1.655	1.993	1.010	3.440
t4	40	1.782	0.572	0.090	1.599	1.964	0.940	3.290
t5	40	1.796	0.538	0.085	1.624	1.968	1.020	3.340
t6	39	1.828	0.543	0.087	1.652	2.005	0.990	3.010
t7	27	1.899	0.446	0.086	1.722	2.075	1.210	2.780
t8	33	1.975	0.649	0.113	1.745	2.206	1.090	3.320
t9	27	1.752	0.475	0.091	1.564	1.940	1.060	2.850
t10	9	1.981	0.672	0.224	1.465	2.498	1.230	2.780
t11	17	1.734	0.518	0.126	1.467	2.000	1.040	2.850
t12	40	1.924	0.531	0.084	1.754	2.094	1.070	3.680
t13	40	2.006	0.545	0.086	1.831	2.180	1.040	3.490
t14	40	1.854	0.613	0.097	1.658	2.050	0.950	3.860
t15	40	1.887	0.616	0.097	1.690	2.084	0.970	3.820
t16	40	2.333	0.649	0.103	2.126	2.541	1.040	4.200
t17	40	2.200	0.550	0.087	2.024	2.376	1.110	3.440
t18	32	2.352	0.467	0.083	2.183	2.520	1.490	3.230
t19	30	2.181	0.471	0.086	2.005	2.357	1.480	3.370
t20	40	2.354	0.639	0.101	2.150	2.558	1.410	4.130
t21	40	2.437	0.622	0.098	2.238	2.636	1.410	4.130
t22	23	2.472	0.621	0.130	2.203	2.741	1.730	4.440
t23	7	2.363	0.556	0.210	1.849	2.877	1.730	3.270
t24	12	2.526	0.779	0.225	2.031	3.021	1.730	4.440
t25	19	2.496	0.710	0.163	2.154	2.839	1.240	4.440
t26	15	2.463	0.487	0.126	2.194	2.733	1.780	3.550
Total	850	2.028	0.619	0.021	1.986	2.070	0.890	4.440

Table 7.6: Descriptive statistics for the 27 criteria. The upper and lower bounds represents the range where most of the average distances are contained. The Min and Max values are the minimum and maximum values of the mean values.

Test Label	N	1	2	3	4	5	6	7
t11	17	1.734						
t9	27	1.752	1.752					
t1	40	1.764	1.764	1.764				
t4	40	1.782	1.782	1.782				
t5	40	1.796	1.796	1.796				
t0	40	1.796	1.796	1.796				
t3	40	1.824	1.824	1.824				
t6	39	1.828	1.828	1.828				
t14	40	1.854	1.854	1.854	1.854			
t2	40	1.856	1.856	1.856	1.856			
t15	40	1.887	1.887	1.887	1.887	1.887		
t7	27	1.899	1.899	1.899	1.899	1.899	1.899	
t12	40	1.924	1.924	1.924	1.924	1.924	1.924	1.924
t8	33	1.975	1.975	1.975	1.975	1.975	1.975	1.975
t10	9	1.981	1.981	1.981	1.981	1.981	1.981	1.981
t13	40	2.006	2.006	2.006	2.006	2.006	2.006	2.006
t19	30	2.181	2.181	2.181	2.181	2.181	2.181	2.181
t17	40	2.200	2.200	2.200	2.200	2.200	2.200	2.200
t16	40	2.333	2.333	2.333	2.333	2.333	2.333	2.333
t18	32		2.352	2.352	2.352	2.352	2.352	2.352
t20	40		2.354	2.354	2.354	2.354	2.354	2.354
t23	7			2.363	2.363	2.363	2.363	2.363
t21	40				2.437	2.437	2.437	2.437
t26	15					2.463	2.463	2.463
t22	23					2.472	2.472	2.472
t25	19						2.496	2.496
t24	12							2.526
sig.		0.058	0.055	0.059	0.080	0.077	0.060	0.056

Table 7.7: Means for groups in homogeneous subsets. The group sizes are unequal. The harmonic mean of the group sizes is used. Type I errors are not guaranteed.

	Sum of Squares	df	Mean Square	F	Sig
Between Groups	55.657	26	2.141	6.528	0.000
Within Groups	269.873	823	0.328		
Total	325.530	849			

Table 7.8: Summary of the ANOVA analysis. In this table df stands for degrees of freedom and F is the value of the F test for the difference between means.

Chapter 8

Conclusions

This thesis has presented a method to produce detailed 3D skull-face models from MRI datasets and a CFR system based on a database of the skull-face models. To produce the 3D skull models, two skull extraction algorithms, one in 2D and one in 3D, were implemented, as described in chapters 4 and 5, respectively. In the 2D approach, the skull surface is extracted by segmenting a set of images of an MRI volume. At each slice, the skull region is segmented as a single contour or, when the skull topology is more complex, as a combination of several partial skull contours. The extracted contours are then assembled to create a 3D skull model. The segmentation process is made up of two components. The first component is an active contour directed by image features which 'blindly' tries to enclose skull areas. The second component is a shape term which adds statistical knowledge of the likely shape to find. The two components are combined to make an active contour evolve towards a minimum within the static potential field calculated from the gradient information in an image.

The 3D approach is an extension of the 2D approach. The 3D method uses a deformable model which iteratively adjusts its shape to fit the skull embedded in an MRI volume. Shape changes in the deformable model are defined by combining, as in the 2D approach, two elements: information provided by MRI volume features and knowledge about the 3D structure of a skull shape. The influence of these two components in the deformable model evolution is modelled as a Bayesian energy formulation. The best fitting skull model is obtained by imposing shape restrictions derived from a training set of skull shapes.

The result of the 3D approach is a database of head models created from MRI data with a high level of detail. This shows that it is possible to generate alternative anthropometric information sources with much greater level of detail than traditional anthropometric sources. This will allow further study into the skull-face relationship and the potential to conduct more analysis on the surface-to-surface dependency between the skull and face. Also, as it is based on MRI data, the information created can be extended and updated according to specific populations.

Certain aspects of the computerised reconstruction process have been designed using simple approaches (e.g. the linear strategy of template creation). The process could potentially be made even more efficient by developing semi-automated elements as in the pre-processing stage to create the first noisy skull approximation or in the case of the skull template registration stage. In the 3D skull extraction method several issues need to be addressed to improve the implementation and reduce possible error sources. During the pre-processing stage, the user is asked to manually identify a set of areas in an MRI scan corresponding to skull regions (the region-growing stage). Even though the task is simple,

this will require training in a real application. The statistical formulation implemented showed that it was possible to obtain acceptable results, but the impact of different errors was not evaluated. In a subsequent stage, this can be done by conducting sensitivity error tests on each stage of the process.

Another aspect to be improved is the registration step used in the initialisation stage. Currently, a set of 3D curves is manually drawn on both the noisy skull and the clean skull template. This process could be automated by analysing the curvature in both models. Even though the initial registration is manual, the errors introduced are not considered to impact on the final result because the main objective is to limit the search space for the deformable model fitting.

The database of skull-face models is used in a CFR system, as described in chapter 6. This CFR system consists of three main stages: skull examination, template construction and face construction. In the first stage, the input skull is analysed and a set of main features extracted. In the second stage, combining these features with information about the skull-face relationship provided by the database, the system creates a head template from combining the information of the selected models. In the last stage, possible face estimations for the input skull are created by fitting the skull of the head template created to the input skull. The anthropometric information is provided by the database of head models presented in chapter 5.

The use of the skull surface to deform the surrounding 3D space (equivalent to volume deformation) addresses some of the problems encountered in techniques based on estimating landmark positions in models. The use of spatial deformation allows the facial tissues (skull, muscle, etc.) to be dealt with as a single component, thus freeing the procedure from the problem of placing and interpreting anthropometric landmarks associated with soft tissue depth tables. Facial soft tissues should change in response to the changes in the skull, and therefore the face is not merely a mask depending on a small number of soft tissue depth points.

The experiments conducted include 5 features with 27 combinations of these features. As a result 850 reconstructions were evaluated. From the statistical analysis, it was not possible to determine a difference between reconstructions created with correct features and using differing numbers of features. A distinction was obtained between features using single correct features with respect to reconstruction carried out with any incorrect feature. Possible explanations for these results are, as discussed in chapter 7, the size of the database and the linear method used to generate the head template.

In our system, approximately 80% of the best reconstruction scores have less than 2.5 mm error. The remaining 20% have less than 3.5mm of error. These figures are, as stated in chapter 7, comparable in terms of magnitude with other computerised CFR systems using similar evaluation measurements. Even though the number of models in the database is limited, the results obtained from this system suggest that accurate reconstructions can be achieved by using the data generated from the skull-face models produced from MRI data.

The experimental results produced in this thesis show the feasibility of including information generated from MRI data. They also show that it is possible to obtain accurate rates of intra-landmark surface estimation by considering statistics of the skull face relationship with the new type of data generated from MRI.

With MRI data, the landmarks commonly used in other studies could be replicated, validated and even replaced using in vivo data from modern individuals at a higher level of detail. Skull and facial features could be examined in ways which have not been possible

until now. Although the interrelationships of certain bony features and their soft tissue counterparts have been described in several works [38], the statistical evidence for the findings have not been published.

The main application of the segmentation method, the data and the CFR system presented in this thesis was focused on forensic applications. The skull segmentation technique can be adapted to segment any other type of volumetric structure with applications in a wide range of medical imaging problems. In addition to the skull and face, MRI data can provide 3-dimensional information about other elements with different tissue types (e.g. muscle, cartilage, etc.). Also, the data produced can be used to create atlases and determine guidelines for modelling missing parts in reconstructive surgery. This information could be of benefit to the maxillofacial and orthodontic fields as a reference collection of healthy subjects. The database of head models can be used to conduct analysis of the skull and face, (e.g. shape variability) and to test different facial reconstruction methods. The craniofacial reconstruction system can be used to produce different face models in terms of the parameters given to the system. Incorporating age changes for a given skull can be used to simulate results of possible corrective surgeries or implant design for facial parts.

There is still debate on whether or not artistic skill can produce reconstructions with better recognition scores than precise accurate reconstructions [90, 70]. Producing an accurate facial surface does not automatically lead to better recognition scores [70]. Our perception of a face is highly influenced by other facial features such as the eyebrow shape, or hair style [109, 29]. Even though, our research was focused generate accurate facial estimations, additional components can be added to the results to produce more realistic faces. Accuracy in the facial estimations will at least produce consistent results based on statistical data.

Also, the method to incorporate the shape restrictions can also be used to guide deformations between different structures (e.g. applications in animation, morphing and shape analysis) and also for evaluating the quality and shape similarity between geometrical objects. This is possible by evaluating the shape function for different objects and determining how different this value is for different models.

Appendix A

Anatomy of the human head

The appearance of the face is mainly determined by the major structures of the head: the skull, the muscles and the skin. This section presents the most important aspects in the relation of between these elements. The interested reader can consult [67, 88]. The skull is the underlying supporting structure of the head formed by the neurocranium and the facial skeleton figure A.1. The neurocranium is the structure that protects the brain and its related tissues. The facial skeleton consists of 14 irregular bones: lacrimal, nasal, maxilla, zygomatic, palatine and the inferior nasal conchae bones (two of each), the mandible and a vomer. The neurocranium is formed by: A frontal bone, two parietal bones and two temporal bones, an occipital and sphenoid bone and the ethmoid bone. The facial skeleton is the anterior part of the skull containing the orbits, nasal cavities, maxilla and mandible, which is the upper and lower jaw. The mandible is the dynamic structure of the head; its size, shape and the number of teeth it normally bears undergo considerable changes with age [67].

The face is the anterior area of the head extends form the forehead to the chin and from one ear to the other. Some bones of the skull determine the shape of the face. The pads in the cheeks and the facial muscles contribute to the final shape of the face. The facial expressions are determined by the motion of the muscles lying between the skin and skull. Facial muscles can be classified into two groups: muscles of mastication and muscles of expression. The number of facial muscles varies in the literature due to the fact that more than 50 muscles can be identified and some of them can be considered as groups of smaller muscles themselves.

The muscles are attached to the bone and belong to the subcutaneous tissue. The eyes and nose act as sphincters and dilators (see figure). The skin of the face is connected to the bones by bands of connective tissue [67]. The muscles of expression are categorised by their regions of influence: the scalp, the eyelid, the nose, the mouth and the neck. Figure A.2 show the most important muscles of the face. Most muscles of the face originate at the bone structure, while their surface inserts into the skin. When contracting, the muscle pulls the skin towards its fixed origin. However, there are other muscles that attach to bone on both ends.

The skin is a system with different components working together to provide protection against external environmental influences (e.g. bacteria and toxic substances), to regulate the body temperature, and to storage of water, fat and blood. Each square centimetre of skin contains on average 1 meter vessels, 15 sebaceous glands, 100 sweet glands, 3000 nerve ends, and 3,000,000 cells [50]. The skin plays an important role in human communication by means of facial expression, texture, colour and scent.

This introduction to the head anatomy is by no means exhaustive, but is useful to

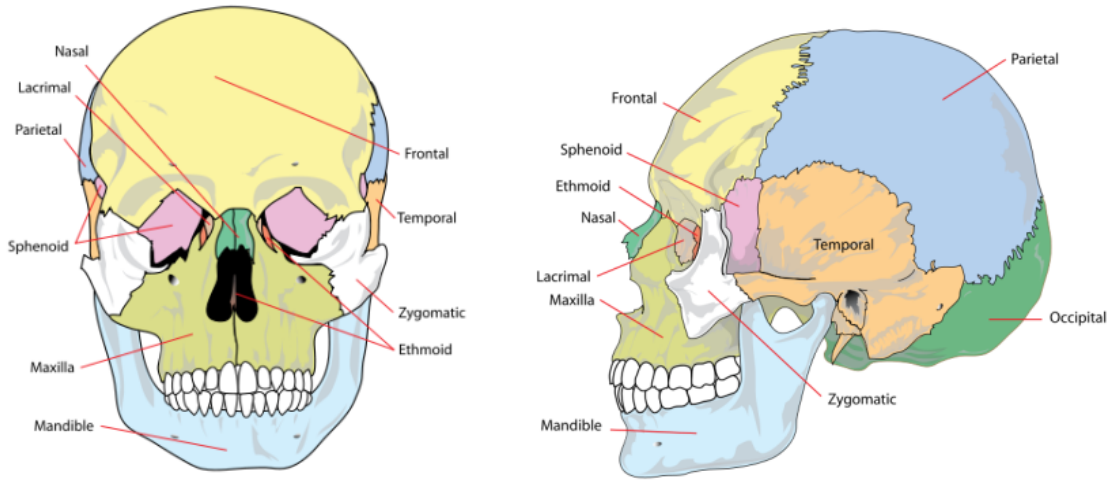

Figure A.1: Frontal and side views of a skull showing the bone structure (image obtained of wikimedia commons available as a public domain resource).

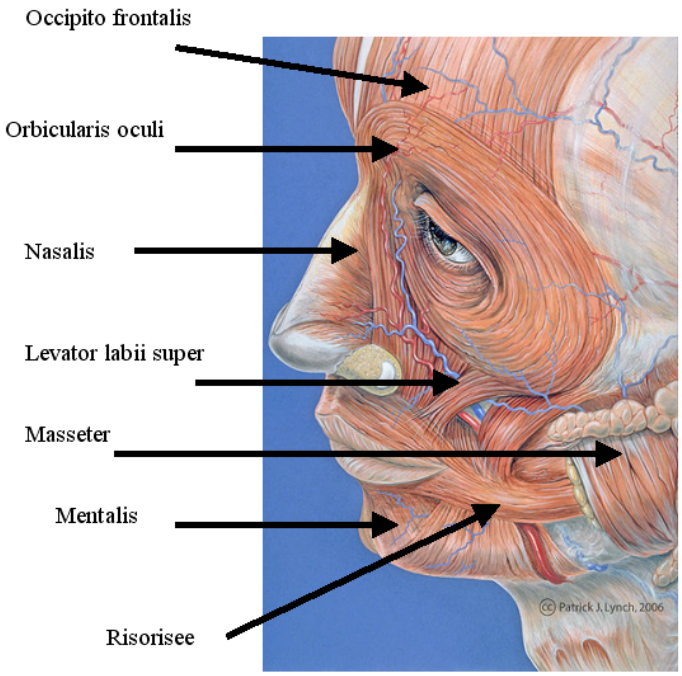

Figure A.2: The main muscles of the face (image obtained of wikimedia commons available as a public domain resource).

give an idea from an anatomic perspective about the complexity of the factors that can influence the shape of the facial surface.

Appendix B

Surface comparison used by metro

Metro software implements an approach based on an error approximation by means of surface sampling and the computation of point-to-surface distances [21]. The surface of the first mesh (pivot mesh) is sampled, and for each elementary surface region the distance to the not-pivot mesh is computed. Thus, the error between two meshes is defined as the distance between corresponding sections of the meshes. Given a point p and a surface S, the distance $e(p, S)$ is defined as:

$$e(p, s) = \min_{p' \in S} d(p, p')$$

Where d is the Euclidean distance between two points. In 3D the one-sided distance between two surfaces S_1, S_2 is defined as $e(S_1, S_2) = \max_{p' \in S_1} e(p, S_2)$ which is not symmetric. (i.e. $e(S_1, S_2) \neq E(S_2, S_1)$). A two sided distance can be obtained by using max $(e(S_1, S_2), e(S_2, S_1))$. Given a set of uniformly sampled distances, the mean distance Em between two surfaces is the surface integral of the distance divided by the area of S_1:

$$E_m(S_1, S_2) = \frac{1}{|S_1|} \int_{S_1} (e(p, S_2)) ds$$

Metro evaluates the difference between meshes on the basis of the approximate distance evaluated with E_m. On each mesh vertex metro computes a distance (as the mean of the distance on the incident faces), and assign a colour proportional to that difference. The faces are then coloured by interpolating vertex colours.

Appendix C

Implementation details and processing times

The software tools for edition, pre-processing and skull segmentation were implemented using the programming language VC++ 6.0 with openGL. The Gradient vector flow calculation, the registration techniques (Robust Point Matching algorithm) and the shape energy calculation were implemented using Matlab 7.0. [1] To draw the 3D curves to generate the matching features to register the skull models, the software vrmesh was used. 3Dsmax software[2] was used for render the skull and face models. The Meshlab[3] software toolkit was used to process the 3D models and for format conversion between files.

In order to give a general idea about the performace of the implemented tools the following is a list summarising the processing times required on the main stages of this project:

- Registration of skull features. The processing time for registering two sets of curves with 700 points each is 7 minutes approx. and using 60 iterations. This number of points was the average used for registering each of the skull models.
- GVF calculation. For calculating the gradient vector flow in 3D for a sub-volume of 256x256x50 voxels the processing time is 16 minutes using 120 iterations for calculating the solution to the gradient descent differential equation. The sub-volume dimension corresponds to the spatial region of the MRI volume was the area of the head is located.
- Template Deformation algorithm. A total of 180 hours were required to process the 60 skull models of the database using 3000 control points per model and 100 iterations (i.e. 3 hours on average per dataset).
- Facial Reconstruction algorithm. For producing the data shown in table 7.5 the processing time was 3.5 hours on average per criteria. A total of 120 hours (approx.) were dedicated to produce the 850 facial reconstructions. The time varies depending on the amount of head templates used for the test. In the worst case 27 facial reconstructions were done per criteria.
- These results were obtained using a Dell Dimension DXP061 computer with two Intel(R) processors 6600 running at 2.4GHz and 2.0 GB of RAM.

[1] more information in : http://www.mathworks.com/

[2] for more information visit: http://usa.autodesk.com/adsk/servlet/pc/index?id=13567410&siteID=123112

[3] available at: http://meshlab.sourceforge.net/

Appendix D

Analysis of variance

In this appendix, a summary of the most important aspects behind the Analysis of variance are presented. The model assumed for the observations from a one-way design is:

$$y_{ij} = \mu_i + \varepsilon_{ij}$$

where y_{ij} represents the j^{th} observation in the ith group, and the ε_{ij} represent random error terms, assumed to be from a normal distribution with mean zero and variance σ^2.

The null hypothesis of the equality of population means can now be written as:

$$H_0 : \mu_1 = \mu_2 = \ldots = \mu_k = \mu$$

leading to a new model for the observations:

$$y_{ij} = \mu + \varepsilon_{ij}$$

Reformulating the model by modeling the mean value for a particular population as the sum of the overall mean value of the response plus a specific population or group effect, leads to a linear model of the form:

$$y_{ij} = \mu + \alpha_i + \varepsilon_{ij}$$

where μ represents the overall mean of the response variable, α_i is the effect on an observation of being in the i^{th} group ($i = 1, 2, \ldots k$) and again ε_{ij} is a random error term, assumed to be from a normal distribution with mean zero and variance σ^2.

When written in this way, the model uses $k+1$ parameters $(\mu, \alpha_1, \alpha_2, \ldots \alpha_k)$ to describe only k group means. In other words, the system is *overparameterized*, which causes problems because it is impossible to find unique estimates for each parameter. The following constraint is generally applied to overcome the problem:

$$\sum_{i=1}^{k} \alpha_i = 0$$

If this model is assumed, the hypothesis of the equality of population means can be rewritten in terms of the parameters α_i as

$$H_0 : \alpha_1 = \alpha_2 = \ldots \alpha_k = 0$$

so that under H_0 the model assumed for the observations is

$$y_{ij} = \mu + \varepsilon_{ij}$$

as before.

The necessary terms for the F-tests are usually arranged in an *analysis of variance table* as shown in table D.1 (N is the total number of observations).

Source of variation	*DF*	*SS*	*MS*	*MSR(F)*
Between groups	$k-1$	BGSS	BGSS/(k-1)	MSBG/MSWG
Within groups (errors)	$N-k$	WGSS	WGSS/(N-k)	
Total	$N-1$			

Table D.1: Results of ANOVA presented in a table. DF stands for degrees of freedom, SS is sum of squares, MS is mean square, BGSS is between groups sum of squares, and WGSS is within group sum of squares.

If H_0 is true and the assumptions listed below are valid, the mean square ratio (MSR) has an F-distribution with $k-1$ and $N-k$ degrees of freedom.

The data collected from a one-way design have to satisfy the following assumptions to make the F-test involved strictly valid:

1. The observations in each group come from a normal distribution.
2. The population variances of each group are the same.
3. The observations are independent of one another.

When significant results have been obtained from an overall F-test, investigators often wish to undertake further tests to determine which particular group means differ. A number of procedures generically known as *multiple comparison techniques* can be employed for this purpose. Such procedures retain the nominal significance level at the required value when undertaking multiple tests. These methods are known as "post hoc multiple comparison" methods since they should only be carried out once an overall effect of the grouping factor has been established. Tukey's honestly significant differences (HSD) is used in this thesis. (For details of these and the remaining multiple comparision techniques, see Everitt, 2001, and Howell, 2002).

Appendix E

Statistical Shape Analysis Theory

Recent advances in electronic and computer technology allow the collection of two and 3-dimensional information about the anatomical structures of the human body in large scales. This information can be applied in a wide variety of disciplines from biology, medicine, anthropology etc. One of the most important tasks is the development of computational techniques to analyse the information contained in the shape of these structures, where shape is a term used to denote the appearance of an object [35]. This appendix presents Procrustes Analysis.

E.1 Shape Distances and Procrustes Analysis

The distance between two shapes should be a measure of how "far apart" the shape sets are. It is simple to standardize the location and size, but not the rotation [35]. The solution is to find the transformation that brings the pre-shape of an object as close as possible to the pre-shape of the other object: With scaling and rotation.

$$d_f(X_1, X_2) = \inf_{\Gamma\beta} \parallel Z_2 - \beta Z_1 \Gamma \parallel \tag{E.1}$$

this is the full Procrustes distance, where β is the scale factor and $Z_r = \frac{HX_r}{\|HX_r\|}$, for $r = 1, 2$

E.1.1 Procrustes Distances

The Procrustes distance $\rho(X_1, X_2)$ is the closest great circle between Z_1 and Z_2 on the pre-shape sphere (see figure E.1) where:

$$Z_j = HX_j / \parallel HX_j \parallel, \quad j = 1 \dots 2 \tag{E.2}$$

the Procrustes distances can be calculated with the following expressions minimizing over rotations and scale to find the closest Euclidian distance between Z_1 and Z_2 :

$$d_f(X_1, X_2) = \sqrt{1 - (\sum_{i=1}^{m} \lambda_i)^2} = \sqrt{1 - \hat{\beta}^2} \tag{E.3}$$

where $\lambda_1 \geqslant \lambda_2 \geqslant \ldots \geqslant \lambda_{m-1} \geqslant \mid \lambda_m \mid$ are the square roots of the eigenvalues of $Z_1^T Z_2 Z_2^T Z_1$

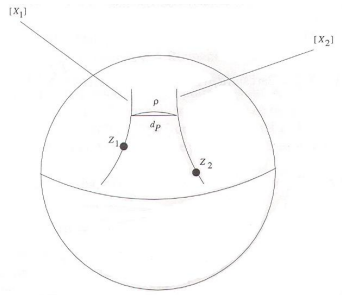

Figure E.1: A diagrammatic view of two shapes X_1 and X_2 on the pre-shape sphere, which correspond to the shapes of the original configuration matrices X_1 and X_2 which have pre-shapes Z_1 and Z_2. ρ is the smallest great circle representing the Procrustes distance and d_p is the partial Procrustes distance. Figure adapted from [35]

The partial Procrustes distance d_p is obtained by matching the pre-shapes Z_1 and Z_2 of X_1 and X_2 as closely as possible over rotations but not scale. The following expression define the partial Procrustes distance:

$$d_p(X_1, X_2) = \sqrt{2}\sqrt{1 - \sum_{i=1}^{m} \lambda_i} = \sqrt{2}\sqrt{1 - \hat{\beta}} \tag{E.4}$$

$$\rho(X_1, X_2) = \arccos \sum_{i=1}^{m} \lambda_i = \arccos \hat{\beta} \tag{E.5}$$

A location transformation is not needed in the Procrustes analysis; it will become zero.

E.1.2 General Procrustes Analysis

Suppose we have several objects of the same type, but varying shape $X_1 \dots X_n$.

The full procrustes mean is the shape X_0 that minimizes the sum of Procrustes distances to all the objects:

$$X_0 = \arg\min_{X_0} \sum_{k=1}^{n} d_f(X_0, X_k) \tag{E.6}$$

this shape is called the full Procrustes mean. The full Procrustes mean can be calculated by eigen vector analysis. For the case of two dimensions, [35] use complex numbers to derive compact expressions for the distances. In higher dimensions (such as the common 3D case) an explicit methods is needed.

Computing the Procrustes Transformation

Let USV^T be the singular value decomposition of $Z_1^T Z_2$, with singular values $\lambda_1 \geqslant \dots \geqslant \lambda_m$

If we allow reflections as well as rotations, the minimizing rotation is given by

$$\hat{\Gamma} = UV^T \tag{E.7}$$

and the minimizing scale is given by:

$$\hat{\beta} = \sum_{i=1}^{m} \lambda_i \tag{E.8}$$

(for pure rotations, appropriate sign changes may be required)

The Procrustes aligned pre-shapes are denoted by $Z_k^P = \hat{\beta} Z_k \hat{\Gamma}$

E.1.3 Full Procrustes Mean Algorithm

Algorithm for finding the full Procrustes mean shape:

1. Start by letting Z_0 equal to the pre-shape of one of the given shapes, Z_1, say.
2. Compute the Procrustes-aligned pre-shapes Z_k^p of Z_k onto Z_0, for all $k = 1 \dots n$
3. Set Z_0 equal to the average of the Procrustes -aligned shapes, and normalise: $Z_0^* = \frac{1}{n} \sum_{k=1}^{n} Z_k^p$, and $Z_0 = Z_0^* / \parallel Z_0^* \parallel$
4. Repeat steps 2 and 3 until Z_0 has stabilised.

An icon of the mean shape estimate is given by $\hat{X}_0 = H^T Z_0$, if Helmertised pre-shapes were used

E.1.4 Summary: Shape Comparison using Procrustes Analysis

The full Procrustes alignment of a pre-shape Z_1, to another pre-shape Z_2 , is the shape $Z_1^p = Z_1\ \Gamma\beta$ that minimizes $\parallel Z_2 - \beta Z_1 \Gamma \parallel$,

overall rotation (or all orthogonal) matrices Γ and non-negative scaling factors β.

The full Procrustes distance is $d_f(Z_1, Z_2) = \sqrt{1 - \beta^2}$

The partial Procrustes distance is $d_p(Z_1, Z_2) = \sqrt{2}\sqrt{1 - \beta}$

The Procrustes distance is $\rho(Z_1, Z_2) = \arccos \hat{\beta}$

Note that $d_f < d_p < \rho$ with equality only when $Z_1 = Z_2$

The full Procrustes mean is the shape that minimises the sum of squared shape distances for a set of objects:

$$Z_0 = \arg\min_{Z_0} \sum_{k=1}^{n} d_f(Z_0, Z_k) \tag{E.9}$$

an example of the analysis presented in this section for the 2-dimensional case can be shown in figure E.2:

E.1.5 Shape Variability

Since the tangent space is linear, ordinary multivariate modelling techniques can be used to capture the variability in a set of shapes. It is necessary to construct probability models for the eigenstructure of sample covariance matrix S_v ($v_k s$). The resulting shapes can be illustrated by transforming back to ordinary pre-shapes, and then computing icons.

Definition 1 *An icon is a particular member of the shape space* $[X]$ *which is taken as being representative of the shape.*

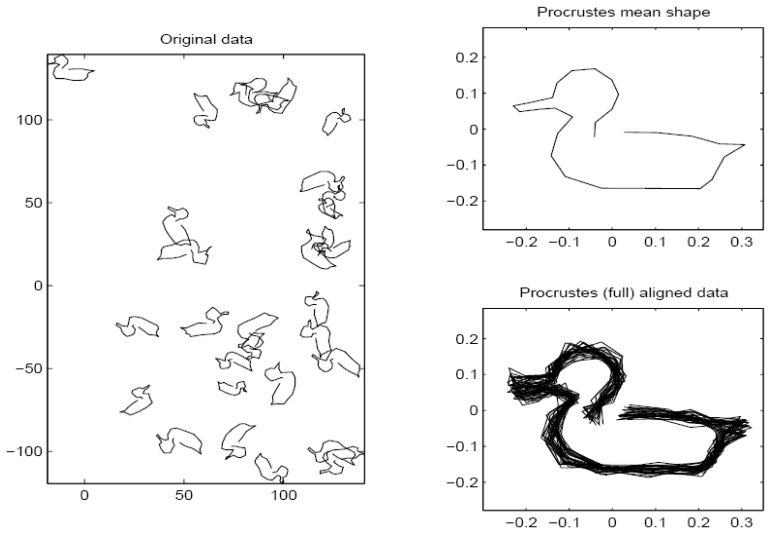

Figure E.2: Procrustes analysis performed in a set of land-marked figures of a duck. The figure on the left shows the different shapes in their original positions. Then a mean shape and the aligned shapes using the Procrustes analysis is presented in the right diagrams.

One potential problem: High-dimensional space.

Reduce the dimensionality by principal component analysis (PCA). At this time, the principal component axes themselves are of interest, in addition to the PC-coordinates.

E.1.6 Euclidean Distance Matrix Analysis

The basis of the Euclidean Matrix Distance Analysis ($EDMA$) applications is the form matrix (FM). Suppose we have the mean coordinates of a surface A, measured by K landmarks. The form matrix $FM(A)$ is defined as:

$$FM(A) = \begin{bmatrix} 0 & d(1,2) & \cdots & d(1,K) \\ d(2,1) & \ddots & & \vdots \\ \vdots & & \ddots & d(K-1,K) \\ d(K,1) & \cdots & d(K,1-K) & 0 \end{bmatrix} \tag{E.10}$$

where $d(i,j)$ is the Euclidean distances between landmarks i and j. This representation is coordinate-system invariant because the elements of $FM(A)$ are always the same, no matter how A is positioned. Suppose that we have a new surface patch B, with its own form matrix $FM(B)$ and we want to compare the forms. We can define a from-difference matrix, called $FDM(A,B)$ as follows:

$$FDM(A,B)_{ij} = \frac{FM(A)_{ij}}{FM(B)_{ij}} \tag{E.11}$$

where $i,j = 1..K$ and with the convention $\frac{0}{0} = 0$. Each element of the FDM is the ratio of like distances in A and B. If A and B are identical in form, all of the off-diagonal elements in FDM will be one. If a given distance is greater in A than in B, the corresponding element in FDM will be greater than one:

$$if\ FM(A)_{i,j} > FM(B)_{i,j} \rightarrow FDM(A,B)_{i,j} > 1 \tag{E.12}$$

Similarly, an instance where an element of B is greater will be indicated by an element that is less than one. If all the elements of the off-diagonal in matrix FDM are equal an greater than one, then surface patches A and B will have the same shape, but it will differ in scale. And finally if the off-diagonal elements in FDM are heterogeneous, A and B will differ in shape. It is important to notice that the elements of $FM(A)$ and $FM(B)$ are always the same, no matter how either A and B are translated, rotated or reflected.

The form-difference matrix can be used as the basis of a dissimilarity measure, called F_Ω, between two sampled surface patches [57]. Given $FDM(A,B)$, we can calculate:

$$F_\Omega(A,B) = \sqrt{\sum \left[\ln(FDM(A,B))\right]^2} \tag{E.13}$$

where the summation is over all of the below-diagonal elements of $FDM(A,B)$. $F_\Omega(A,B)$ is a metric and it is equivalent to the $Q-mode$ Euclidean distance between A and B [87]. If A and B are identical then F_Ω will equal zero; otherwise F will become increasingly positive as A and B become more different in form.

Appendix F

Robust Point Matching Algorithm

An example in 2D will be used for explaining the Robust Point Algorithm. Consider two point-sets V and X (in $\Re^2$) consisting of points $\{v_a,\, a = 1, 2, ...K\}$ and $\{x_i,\, i = 1, 2, ...N\}$ respectively. Where f is a non-rigid tranformation. A point v_a is mapped to a new location $u_a = f(v_a)$. The whole transformed point set V is then U or $\{u_a\}$. A smoothness measure is used to place constraints on the mapping. The operator L is defined to control the smoothness measure. The expression controlling the global smothness measure is defined by $\parallel Lf \parallel^2$. The function f is defined by a Thin-Plate Spline [8].

The objective is to minimise a binary linear alignment least square energy function [19]:

$$\min_{z,f} E(Z, f) = \min_{z,f} \sum_{i=1}^{N} \sum_{a=1}^{K} z_{ai} \parallel x_i - f(v_a) \parallel^2 + \lambda \parallel Lf \parallel^2 - \zeta \sum_{i=1}^{N} \sum_{a=1}^{K} z_{ai}$$

subject to $\sum_{i=1}^{N+1} z_{ai} = 1$ for $i \in \{1, 2, ...N\}$, $\sum_{i=1}^{K+1} z_{ai} = 1$ for $i \in \{1, 2, ...K\}$ and $z_{ai} \in \{0, 1\}$. Z is called the correspondence matrix [19] and consists of two parts: the inner $N \times K$ part of Z defines the correspondence between points. The extra $N + 1^{th}$ rows and $K + 1^{th}$ columns of Z are introduced to handle the outliers. If a point v_a coresonds to a point x_i, $z_{ai} = 1$, otherwise $z_{ai} = 0$. The row and column summation constraints guarantee that the correspondence is one-to-one. Once a point is rejected as an outlier the extra entries will start taking non-zero values to satisfy the constraints. An example of a correspondence matrix is given in table F.1.

z_{ai}	x_1	x_2	x_3	x_4	*outlier*
v_1	1	0	0	0	0
v_2	0	1	0	0	0
v_3	0	0	0	0	1
outlier	0	0	1	1	0

Table F.1: Matrix of correspondences

The parameters λ and ζ are the weight parameters used to balance the terms. The point matching algorithm function consists of a linear assignment of discrete points problem on the correspondence and a least-squares continuous problem on the transformation

[20]. The robust point matching algorithm involves a dual update process combined with an annealing scheme.

Step 1: Updating the correspondence

For the points $a = 1, 2, ..., K$ and $i = 1, 2, ..., N$

$$m_{ai} = \frac{1}{T} e^{-\frac{(x_i - f(v_a))^T (x_i - f(v_a)}{2T}}$$

and for the outlier entries $a = K + 1$ and $i = 1, 2, ..., N$

$$m_{K+1,i} = \frac{1}{T_0} e^{-\frac{(x_i - v_{K+1})^T (x_i - v_{K+1})}{2T_0}}$$

and for the outlier entries $a = 1, 2, ..K$ and $i = N + 1$,

$$m_{a,N+1} = \frac{1}{T_0} e^{-\frac{(x_N - f(v_a))^T (x_{N+1} - f(v_a))}{2T_0}}$$

where v_{K+1} and x_{N+1} are the outlier cluster centers as explained above.

Then, the row and column normalization algorithm is run to satisfy the constraints until convergence is reached,

$$m_{ai} = \frac{m_{ai}}{\sum_{b=1}^{K+1} m_{bi}}, i = 1, 2, ..., N$$

$$m_{ai} = \frac{m_{ai}}{\sum_{j=1}^{N+1} m_{aj}}, a = 1, 2, ..., K$$

As the correspondence matrix does not change much, the number of iterations in rows and column normalization are fixed and independent of the number of points. Previous value can be used as an initial condition.

Step 2: Update the Transformation:

$$\min_f E(f) = \min \sum_{i=1}^{N} \sum_{a=1}^{K} m_{ai} \parallel x_i - f(v_a) \parallel^2 + \lambda T \parallel Lf \parallel^2$$

The implementation used in this thesis use the simplified version of the expresion:

$$\min_f E(f) = \min \sum_{a=1}^{K} \parallel y_a - f(v_a) \parallel^2 + \lambda T \parallel Lf \parallel^2$$

where

$$y_a = \sum_{i=1}^{N} m_{ai} x_i$$

The variable y_a is the estimated positions of the pointset (with the set $\{x_i\}$) that corresponds to $\{v_a\}$. If the outliers are too small (i.e. $\sum_{i=1}^{N} m_{ai} << \epsilon$) then they are removed. The solution for this least-squares problem depends on the non-rigid transformation.

Annealing: The updating mechanism is controlled by an annealing strategy. Starting at $T_{init} = T_0$ the temperature T is gradually reduced according to a linear annealing

schedule, $T_{new} = T_{old} \cdot r$ where r is called the annealing rate. The dual updates are repeated until convergence at each temperature. Then t is lowered and the process is repeated until some final temperature T_{final} is reached. T_0 is set to the largest square distance of all point pairs (in our implementation r is set to be 0.93).

For the outlier cluster, the temperature is always kept at T_0.

Matching one-to-one correspondences exactly only works with clean data. As the data usually contains noise, T final is chosen to be the average of the squared distance between the nearest neighbors within the set of points being deformed.

Appendix G

UOS database forms

The University *of* Sheffield

Facial Reconstruction Research Project

Consent Form

CONFIDENTIAL

Family Name:

First Name:

Date of Birth: d d m m y y

Please read the statement and tick ✓ in the boxes that apply to you:-

I have read and understood the above information. I consent to the collection, long term storage and retention and use of my image and biographic information for scientific and technical research in the UK and elsewhere. I certify that the information disclosed by me is true and accurate to the best of my knowledge. ☐

I would like to be kept informed about this study. I agree for my email address to be kept on computer by the University of Sheffield in order to facilitate their disclosure of periodic updates, time and resources permitting. I understand that this e-mail information will be stored separately and will be controlled and accessed only by the organizers of this project, and will not be distributed to any other party. ☐

Email:

Signature: _____

Signature of Parent or Guardian if under 18: _____

Date: _____

Thank you for participating in this study!

For project use only

Protocol: ☐ 1-3 **Location:** ☐ 1 RHH (A)

Key: 0

Date: d d m m y y

Operator:

You are being asked to participate in a research study. Before you decide, it is important you understand why the research is being done and what it will involve. Take time to read the following information carefully and discuss it with others if you wish. Ask us if there is anything that is not clear or if you would like more information. Take time to decide whether or not you wish to take part.

What is the purpose of this study?

The purpose of this study is to help recreate facial appearance from the skull by computer. Facial reconstruction is used as a last resort in cases of missing persons, suspicious death or serious crime where an individual cannot be identified.

You may have seen facial reconstructions on television on the evening news or *BBC Crimewatch UK*. Little scientific work has been done that takes advantage of modern medical imaging techniques to collect measurements of the facial soft tissues that can be used in computerized facial reconstruction.

This research project will develop a means doing so by collecting a database of magnetic resonance imaging (MRI) scans of the head and neck of volunteers. Tissue depth measurements will be collected from the database and used to undertake facial reconstructions in “virtual reality” in the computer. The database will also be used to test the methods used by comparing “virtual” reconstructions with real faces.

Who is organizing and funding the research?

The University of Sheffield is organizing the project, which is funded by the Royal Society of London.

Why have I been chosen?

We are gathering information from volunteers who are willing to participate in our project.

Do I have to take part?

Participation in the project is purely voluntary. It is up to you whether or not you take part. Not everyone is suited to the MRI procedure, especially people who have metallic implants or have worked in occupations such as welding. MRI can be uncomfortable, claustrophobic and noisy for some.

An experienced radiographer, who will explain the procedure to you, will undertake the MRI scan. The radiographer will discuss the procedure with you before you decide whether or not to take part.

If you do decide to take part you will be given this information sheet to keep and be asked to sign a consent form.

You are free to withdraw at any stage without giving a reason.

What will happen to me if I take part?

We will take an MRI scan of your head and neck, and record the following biographical information: your age, sex, ancestral affiliation (ethnicity), and whether any of your relatives are also volunteering. We need to record this information as these factors can affect face shape.

The MRI scan and biographic information will be kept in secure databases. The University of Sheffield will keep this MRI scan and biographical information database after the project is over so that it can continue to be used by researchers interested in craniofacial anatomy. This may include scientists and doctors interested in neuroscience, craniofacial surgery, development of the face or archaeological facial reconstruction, for example. It will not be used for any purpose other than scientific and technical research.

If you initially decide to take part you are still free to withdraw at any time without giving a reason and your database record will be destroyed.

In addition to the biographical information identified above, we will also record your name and date of birth. We need to record your name in case you ask us to remove your data later on. If you want further information about the project we will also record your email address.

Your name and email address (if you provide it) will be stored in a secure database that will be separated from the databases containing your MRI scan and biographical information. The University of Sheffield organizers will maintain control and access to this separate database. A unique key, allocated by the University of Sheffield researchers, will reside in both databases, providing us with the ability to destroy your database record, should you request it.

Except as described above, your MRI scan will not be made public or distributed outside of the scientific, technical or research community and we will not publish any other personal information that will allow you to be specifically identified with your MRI scan.

Your name and email address will not be made public or distributed beyond the Sheffield University researchers engaged in this project.

What will happen to the results of the research study?

The results will be part of a research project due to be completed in Autumn 2005. The scientific results will be published and it is intended that new tools for reconstructing faces which result from this research will be made available to police and forensic scientists.

Contact for further information:

Dr Martin Evison, Research Centre for Human Identification, The University of Sheffield, School of Medicine, Beech Hill Road, Sheffield, S10 2RX, United Kingdom. Tel. +44 114 2713204, Fax. +44 114 2711711, Email. m.p.evison@sheffield.ac.uk.

What if I have complaints or other concerns?

If you are harmed by your participation in this study, there are no special compensation arrangements. If you are harmed due to someone's negligence, then you may have grounds for legal action.

The South Sheffield Research Ethics Committee has reviewed this study.

Complaints Contact for Research Projects

Chris Welsh
Medical Director STH
STH
8 Beech Hill Road
Sheffield
S10 2SB
Tel. +44 114 271 2178
Fax. +44 114 271 3765
Email. Elaine.Buxton@sth.nhs.uk

The University *of* Sheffield

Facial Reconstruction Research Project

Biographical Information

CONFIDENTIAL

Please provide the following information:-

Age: ☐☐ Sex: ☐ (m / f)

How would you describe your ancestry / ethnicity?

Please tick ✓ in the box that applies to you.

White		
British	☐	01
Any other White background (Please describe)	☐	02
Mixed		
White and Black Caribbean	☐	03
White and Black African	☐	04
White and Asian	☐	05
Any other Mixed background (Please describe)	☐	06
Asian or Asian British		
Indian	☐	07
Pakistani	☐	08
Bangladeshi	☐	09
Any other Asian background (Please describe)	☐	10
Black or Black British		
Caribbean	☐	11
African	☐	12
Any other Black background (Please describe)	☐	13
Chinese or other ethnic group		
Chinese	☐	14
Any other (Please describe)	☐	15

Please describe ☐☐☐☐☐☐☐☐☐☐☐☐☐☐

Are any of your relatives participating in this study? Please give details:

Name	Date of Birth (d d m m y y)	They are your? (e.g. mother, brother)

Bibliography

[1] R. Acharya and R.P. Menon. A review of medical image segmentation techniques. In Computer Society Press, editor, *Deformable models in medical image analysis*, pages 140–161. IEEE, 1998.

[2] R. Acharya, R. Wasserman, J. Stevens, and C. Hinojosa. Biomedical imaging modalitieas: an overview. In Computer Society Press, editor, *Deformable models in medical image analysis*, pages 20–44. IEEE, 1998.

[3] R. Acharya, R. Wasserman, Jeffrey Stevens, and Carlos Hinojosa. Biomedical Imaging Modalities: An Overview. In Computer Society Press, editor, *Deformable models in medical image analysis*, pages 140–161. IEEE, 1998.

[4] M.J. Ackerman. The Visible Human Project. *Proceddings of the IEEE*, 86(3):504–511, 1998.

[5] K. Anderson and P.W. McOwan. A real-time automated system for the recognition of human facial expressions. *IEEE Transactions on Systems, Man, and Cybernetics Part B*, 36(1):96–105, 2006.

[6] K.M. Archer. Craniofacial Reconstruction using hierarchical B-Spline Interpolation. Master's thesis, University of British Columbia, 1997.

[7] S.R. Arridge, J.P. Moss, A.D. Linney, and D.R. James. Three Dimensional Digitisation of the Face and Skull. *Journal of Maxillofacial Surgery*, 3(13):136–143, 1985.

[8] R.H. Bartels, J.C. Beatty, and B.A. Barsky. *An introduction to splines for use in computer graphics and geometric design*. Morgan Kauffman, 1987.

[9] R.E. Bellman. *Dynamic Programming*. Princeton University Press, Princeton New Jersey, 1957.

[10] R.E. Bellman. *Dynamic Programming*. Dover Publications, Incorporated, 2003.

[11] A. Blake and M. Isard. *Active Contours*. Springer, London, 1998.

[12] S. Bramble, D. Compton, and L. Klasen. Forensic image analysis. *The 13th INTERPOL Forensic Simposium, Lyon France*, 2001.

[13] H. Bulu and A. Alpkocak. Comparison of 3d segmentation algorithms for medical imaging. In *Computer-Based Medical Systems, 2007. CBMS '07. Twentieth IEEE International Symposium on Computer-Based Medical Systems*, pages 269–274, June 2007.

[14] J.C. Carr, R.K. Beatson, J.B. Cherrie, T.J. Mitchelland W.R. Fright, B.C. McCallum, and T.R. Evans. Reconstruction and representation of 3D objects with radial basis functions. In *Proceedings of ACM SIGGRAPH 2001*, pages 67–76, 2001.

[15] V. Caselles, F. Catte, T. Coll, and F. Dibos. A geometric model for active contours. *Numerische Mathematik*, 66:1–31, 1993.

[16] V. Caselles, R. Kimmel, and G. Sapiro. Geodesic Active Contours. *International Journal of Computer Vision*, 22(1):61–79, 1997.

[17] G. Celniker and D. Gossard. Deformable curve and surface finite elements for free-form shape design. *Computer Graphics SIGGRAPH 91 Proceedings*, 25:257–266, July 1991.

[18] E. Chernyaev. Marching Cubes 33: Construction of Topologically Correct Isosurfaces. Technical report, CERN CN 95-17, 1995.

[19] H. Chui and A. Rangarajan. A New Algorithm for Non-Rigid Point Matching. In *Proceedings of CVPR*, volume 2, pages 40–51, June 2000.

[20] H. Chui and A. Rangarajan. A new point matching algorithm for non-rigid registration. *Computer Vision and Image Understanding (CVIU)*, 89:114–141, 2003.

[21] P. Cignoni, C. Rocchini, and R. Scopigno. Metro: measuring error on simplified surfaces. *Computer Graphics Forum*, 17(2):167–174, 1998.

[22] P. Claes, D. Vandermeulen, S. De Greef, G. Willems, and P. Suetens. Craniofacial reconstruction using a combined statistical model of face shape and soft tissue depths: Methodology and validation. *Forensic Science International*, 159 (Suppl1):147–158, 2006.

[23] L.P. Clarke, R.P. Velthuizen, M.A. Camacho, J.J. Heine, M. Vaidyanathan, L.O. Hail, R.W. Thatcher, and M.L. Silbiger. MRI segmentation: methods and applications. *Magnetic Resonance Imaging*, 13(3), 1995.

[24] J.D. Clayden, A.J. Storkey, and M.E. Bastin. A probabilistic model-based approach to consistent white matter tract segmentation. *Medical Imaging*, 26(11):1555–1561, November 2007.

[25] D. Cremers, M. Rousson, and R. Deriche. A review of statistical approaches to level set segmentation: Integrating color, texture, motion and shape. *International Journal of Computer Vision*, 72(2):195–215, April 2007.

[26] D. Cremers, C. Schnorr, J. Weickert, and C. Schellewald. Diffusion-Snakes Using Statistical Shape Knowledge. In *Lecture Notes in Computer Science*, volume 1888, pages 164–174, 2000.

[27] D. Cremers, F. Tsichhauser, J. Weickert, and C. Schnorr. Diffusion-Snakes: Introducing Statistical Shape Knowledge into the Mumford-shah functional. In *International Journal of Computer Vision*, volume 50-3, pages 295–313, 2002.

[28] S. Davy. Personal communication, November 2005.

[29] S. Davy. *Forensic Facial Reconstruction using Three-Dimensional Computer Modelling Techniques*. PhD thesis, University of Sheffield, 2007.

[30] S. Davy, T. Gilbert, D. Schofield, and M.P. Evison. Forensic Facial Reconstruction Using Computer Modeling Software. In John G. Clement and Murray K. Marks, editors, *Computer Graphic Facial Reconstruction*, pages 183–196. Elsevier LTD., 2005.

[31] S. de Sousa. PolyMeCo: A Polygonal Mesh Analysis and Comparison Tool. Master's thesis, Universidad de Aveiro, ETI department, 2007.

[32] C. Ding and X. He. K-means clustering via principal component analysis. *Proceedings of the 21st International Conference on Machine Learning*, pages 225–232, 2004.

[33] B. Dogdas, D.W. Shattuck, and R.M. Leahy. *Human Brain Mapping*, volume 26-4, chapter Segmentation of skull and scalp in 3-D human MRI using mathematical morphology, pages 273–285. Wiley-Liss, 2005.

[34] M. Domaracki and C.N. Stephan. Facial soft tissue thicknesses in australian adult cadavers. *Journal of forensic sciences*, (51):5–10, 2006.

[35] I.L. Dryden and K.V. Mardia. *Statistical Shape Analysis*. John Wiley, July 1998.

[36] M.P. Evison. Modeling Age, Obesity, and Etnicity in a Computerized 3-D Facial Reconstruction. In *9th Biennial Meeting of the International Association for Craniofacial Identificaction*, FBI, Washington DC, July 2000.

[37] G. Farin. *Curves and Surfaces for Computer-Aided Geometric Design*. Academic Press, San Diego, 1997.

[38] B.A. Fedosyutkin93 and J.V. Nainys. *Forensic Analysis of the Skull: The relationship of skull morphology to facial features*, pages 199–213. Wiley-Liss, 1993.

[39] S. Ghadimi, H. Abrishami-Moghaddam, K. Kazemi, R. Grebe, C. Goundry-Jouet, and F. Wallois. Segmentation of scalp and skull in neonatal MR images using probabilistic atlas and level set method. *Engineering in Medicine and Biology Society, 2008. EMBS 2008. 30th Annual International Conference of the IEEE*, pages 3060–3063, Aug 2008.

[40] C. Goodall. Procrustes methods in the statistical analysis of shape. *Journal of the Royal Statistical Society. Series B (Methodological)*, 53(2):285–339, 1991.

[41] T. Heinoen, H. Eskola, P. Dastidar, P. Laarne, and J. Malmivuo. Segmentation of T1 MR scans for reconstruction of resistive head models. *Computer Methods and Programs in Biomedicine*, 54:173–181, 1997.

[42] K. Han Horst and Heinz-Otto Peitgen. The Skull Stripping Problem in MRI Solved by a Single 3D Watershed Transform. In *Proceedings of MICCAI*, pages 134–143. Lecture Notes in Computer Science, October 2000.

[43] A. Jere, J. Tasic, and F. Permus. Izlocanje lobanje iz mr slik:segmentation of the skull in MRI volumes, October 2001. University of Ljubljana, Slovenia.

[44] I.T. Jolliffe. *Principal Component Analysis*. Springer, New York, NY, USA, 2002.

[45] M.W. Jones. Facial Reconstruction Using Volumetric Data. In H.P. Seidel T.Ertl B.Girod G.Greiner H.Niemann, editor, *Vision, Modeling and Visualization*, pages 135–142. IOS Press, 2001.

[46] M. Kass, A. Witkin, and D. Terzopoulos. Snakes: Active contour methods. *International Journal of Computer Vision*, pages 321–331, 1988.

[47] D.G. Kendall, D. Barden, T.K. Carne, and H. Le. *Shape and Shape Theory*. John Wiley and Sons, 1999.

[48] R. Koch, M. Gross, F. Carls, V. Buren, G. Fankhauser, and Y. Parish. Simulating facial surgery using finite element models. In *Computer Graphics*, volume 30 of *Annual Conference Series*, pages 421–428, 1996.

[49] J. Kollman and W. Buchli. Die persistenz der rassen und die reconstruction der physiognomie prahistorischer schadel. *Archives fur Anthropologie*, (25):329–359, 1898.

[50] K. Kähler. *A Head Model with Anatomical Structure for Facial Modeling and Animation*. PhD thesis, Universitat des Saarlandes, 2003.

[51] K. Kähler, J. Haber, and H.P. Seidel. Reanimating the Dead: Reconstruction of Expressive Faces from Skull Data. In Proceedings of ACM SIGGRAPH 2003, editor, *ACM Transactions on Graphics*, pages 27–31, San Diego, USA, July 2003.

[52] K. Kähler, J. Haber, H. Yamauchi, and H.P. Seidel. Head shop:Generating animated head models with anatomical structure. *Proceedings of the 2002 ACM SIGGRAPH Symposium on Computer Animation*, pages 55–64, 2002.

[53] D.H. Laidlaw, K.W. Fleischer, and A.H. Barr. Partial-volume bayesian classification of material mixtures in mr volume data using voxel histograms. *IEEE Transactions on Medical Imaging*, 17, 1998.

[54] G.V. Lebedinskaya, T.S. Balueva, and E.V. Veselovskaya. *Forensic Analysis of the Skull: Craniofacial Analysis, Reconstructions, and Identification*, chapter Principles of Facial Reconstruction, pages 183–198. Wiley-Liss, 1993.

[55] K.V. Leemput, F. Maes, D. Vandermeulen, and P. Suetens. A statistical framework for partial volume segmentation. Technical Report KUL/ESAT/PSI/0102, Catholic University of Leuven, 2001.

[56] K.V. Leemput, F. Maes, D. Vandermeulen, and P. Suetens. A Unifying Framework for Partial Volume Segmentation of Brain MR Images. *IEEE Transactions on Medical Imaging*, 22(1):105–119, 2003.

[57] S. Lele and J.T. Richstmeier. Euclidean matrix analysis:confidence intervals for form and growth comparison. *American Journal of Physical Anthropology*, 98(1):73–86, 1995.

[58] W.E. Lorensen and H.E. Cline. Marching Cubes: a high resolution 3D surface reconstruction algorithm. In *Computer Graphics*, volume 21-4, pages 163–169. Proceedings of SIGGRAPH, 1987.

[59] M. Lüthi, A. Lerch, T. Albrecht, Z. Krol, and T. Vetter. A hierarchical multi-resolution approach for model-based skull-segmentation in mri volumes. *Conference Proceedings 3D-Physiological Human*, December 2008.

[60] Z. Majid, H. Setan, and A. Chong. Integration of stereophotogrammetry and triangulation-based laser scanning system for precise mapping of craniofacial morphology. Number B5, pages 805–812, 2008.

[61] R. Malladi, J. A. Sethian, and B.C. Vemuri. Shape modeling with front propagation: A level set approach. *IEEE Transactions on Pattern Analysis and Machine Intelligence*, 17(2):158–175, 1995.

[62] A. Mang, J. Müller, and T. M. Buzug. A multi-modality computer-aided framework towards postmortem identification. *Journal of Computing and Information Technology (CIT)*, 14(1):7–19, 2006.

[63] T. McInerney and D. Terzopoulos. Deformable models in medical image analysis: a survey. *Medical Image Analysis*, 1:91–108, 1996.

[64] S.D. Michael and M. Chen. The 3D Reconstruction of Facial Features Using Volume Distortion. In *Proceedings 14th Eurographics UK Conference*, pages 297–305, March 1996.

[65] C.S. Milner, R. Neave, and C.M. Wilkinson. Predicting growth in the aging craniofacial skeleton. *9th Biennial Meeting of the International Association for Craniofacial Identification, FBI*, 3(3), July 2001.

[66] C. Montani, R. Scateni, and R. Scopigno. Discretized marching cubes. In R.D. Bergeron and Kauffman A.E., editors, *Visualization '94 Proceedings*, pages 281–287, Washington D.C., USA, 1994. IEEE Computer Society Press.

[67] K.L. Moore and A.F. Dalley. *Clinically oriented anatomy.* Lippincott Williams @ Wilkins, 4th edition, 1999.

[68] L.A. Nelson and S.D. Michael. The application of volume deformation to three-dimensional facial reconstruction: A comparison with previous techniques. *Forensic Science International*, 94:167–181, 1998.

[69] D.T. O'Mara. *Automated Facial Metrology.* PhD thesis, University of Western Australia, February 2002.

[70] P. Paysan, M. Luthi, T. Albrecht, A. Lerch, B Amberg, F. Santini, and T. Vetter. Face reconstruction from skull shapes and physical attributes. *Proceedings DAGM'09: 31st Pattern Recognition Symposium*, 2009. Jena.

[71] M. Petrick. Volumetric facial reconstruction for forensic identification. In *Seminar Computergraphik*. Universitat Koblenz Landau (Germany), October 2000.

[72] A. Pitiot, A. Toga, and P.M. Thompson. Adaptive elastic segmentation of brain mri via shape-model-guided evolutionary programming. *IEEE Transactions on Medical Imaging*, 21(8):910–923, 2009.

[73] J. Prag and R. Neave. *Making Faces: Using Forensic and Archeological Evidence.* British Museum Press, 1997.

[74] G. Quatrehomme, S. Cotin, G. Subsol, H Delingette, Y. Garidel, G. Grevin, M. Fidrich, P. Bailet, and A. Ollier. A fully three-dimensional method for facial reconstruction based on deformale models. *Journal of Forensic Science*, 42(4):649–652, July 1997.

[75] G. Quatrehomme and G. Subsol. Classical non-computer assisted craniofacial reconstructions. In John G. Clement and Murray K. Marks, editors, *Computer Graphic Facial Reconstruction*, pages 15–32. Elsevier LTD., 2005.

[76] H. Rifai, I. Bloch, S. Hutchinson, J.W., and L. Garnero. Segmentation of the skull in mri volumes using deformable model and taking the partial volume effect into account. *Medical Image Analysis*, 4(3):219 – 233, 2000.

[77] H. Rifai, I. Bloch, S. Hutchinson, J. Wiart, and L. Garnero. Segmentation of the skull in MRI Volumes Using Deformable Model and Taking the Partial Volume Effect into Account. In *SPIE Medical Imaging*, volume 3661, pages 288–299, San Diego, California, 1999.

[78] M. Roy, S. Foufou, and F. Truchetet. Mesh comparison using attribute deviation metric. *International Journal of Image and Graphics*, 4(1):1–14, 2004.

[79] L. Sabin and B.S. Everitt. *A Handbook of Statistical Analysis using SPSS*. Chapman and Hall, 2004.

[80] M. Salas. Reconstruccion craniofacial humana utilizando morfologia matematica y graficas computacionales. Master's thesis, I.T.E.S.M. Campus-Morelos, Mexico, August 1998.

[81] M. Salas and S. Maddock. Segmenting the external surface of a human skull in MRI data by adding shape information to gradient vector flow snakes. Technical Report CS-07-13, University of Sheffield, 2007.

[82] M. Salas and S. Maddock. Segmenting the external surface of a human skull in MRI data. *TPCG'08 The sixth Theory and Practice of Computer Graphics 2008 Conference*, 9-11th June 2008. University of Manchester,UK.

[83] M. Salas and S. Maddock. A 3D Skull Segmentation Method Based on Deformable Models. Technical Report CS-09-10, University of Sheffield, 2009.

[84] M. Salas and S. Maddock. Extracting skull-face models from MRI data for use in craniofacial reconstructions. *Workshop on Face Behaviour and Interaction (FBI 2009) Proceedings*, August 25th 2009.

[85] Z.Y. Shan, C.H. Hua, Q. Ji, C. Parra, X. Ying, M.J. Krasin, T.E. Merchant, L.E. Kun, and W.E. Reddick. A Knowledge-guided Active Model of Skull Segmentation on T1-weighted MR images. In *SPIE Medical Imaging*, volume 6512, March 2007.

[86] G.C. Small. *The Statistical Theory of Shape*. Springer Series in Statistics, 1996.

[87] Sneath and Sokal. *Numerical Taxonomy*. W.H. Freeman, San Francisco, 1973.

[88] J. Sobotta. *Atlas of Human Anatomy: Volume 1 Head, Neck, Upper Limb*, volume 1. Lippincott Williams @ Wilkins, 13th edition, 2001.

[89] V. Spitzer, M.J. Ackerman, A.L. Scherzinger, and D. Whitlock. The Visible Human Male: A Technical Report. *JAMIA*, 3(2):118–130, 1996.

[90] C.N. Stephan. Anthropological facial [']reconstruction' - recognizing the fallacies, [']unembracing' the errors, and realizing method limits. *Science and Justice*, 43(4):193 – 200, 2003.

[91] C.N. Stephan. Beyond the Sphere of the English Facial Approximation Literature: Ramifications of German Papers on Western Method Concepts. *Forensic Sciences*, 51(4):736–739, 2006.

[92] C.N. Stephan, M. Hennenberg, and W. Sampson. Predicting Nose Projection and Pronasale Position in Facial Approximation: A Test of Published Methods and Proposal of New Guidelines. *American Journal of Physical Anthropology*, 122(240-250), 2003.

[93] C.N. Stephan and E.K. Simpson. Facial Soft Tissue Depths in Craniofacial Identification (part i): An Analytical Review of the Published Adult Data. *Forensic Sciences*, 53(6):1257–1272, 2008.

[94] C.N. Stephan and E.K. Simpson. Facial Soft Tissue Depths in Craniofacial Identification (part ii): An Analytical Review of the Published Adult Sub-Data. *Forensic Sciences*, 53(6):1273–1279, 2008.

[95] G. Subsol and G. Quatrehomme. Automatic 3D Facial Reconstruction by Feature-Based Registration of a Reference Head. In John G. Clement and Murray K. Marks, editors, *Computer Graphic Facial Reconstruction*, pages 79–102. Elsevier LTD., 2005.

[96] K. Suzuki. On the thickness of the soft parts of the Japanese face. *Journal of the Anthropological Society of Nippon*, (60):70–11, 1948.

[97] D. Terzopoulos, A. Witkin, and M. Kass. Constraints on deformable models: Recovering 3d shape and nonrigid motion. *Artificial Intelligence*, 36(1):91–123, 1988.

[98] P. Tu, R.I. Hartley, W.E. Lorensen, A. Alyassin, and R. Gupta. Face reconstruction using flesh deformation modes. In John G. Clement and Murray K. Marks, editors, *Computer Graphic Facial Reconstruction*, pages 145–162. Elsevier LTD., 2005.

[99] A.J. Tyrell, M.P. Evison, A.T. Chamberlain, and M.J. Green. Forensic three-dimensional facial reconstruction: historical review and contemporary developments. *Journal of Forensic Science*, 42:651–659, 1997.

[100] D. Vandermeulen, P. Claes, D. Loeckx, S. De Greef, G. Willems, and P. Suetens. Computerized craniofacial reconstruction using ct-derived implicit surface representations. *Forensic Science International*, 259 (Suppl):164–174, 2006.

[101] D. Vandermeulen, P. Claes, and P. Suetens. Volumetric Deformable Face Models for Cranio-facial Reconstructions. *Proceedings of the 4th Symposium on Image and Signal Processing Analysis*, pages 353–358, 2005.

[102] J. VanderPluym, W.W. Shan, Z. Taher, C. Beaulieau, C. Plewes, A.E. Peterson, O.B. Beattie, and J.S. Bamforth. Use of magnetic resonance imaging to measure facial soft tissue depth. *Cleft palate-craniofacial journal*, 44(1):52–57, 2007.

[103] M. Vanezis. *Forensic facial reconstruction using 3-D computer graphics:evaluation and improvement of its reliability in identification*. PhD thesis, University of Glasgow, 2008.

[104] P. Vanezis, M. Vanezis, G. McCombe, and T. Niblett. Facial reconstruction using 3-D computer graphics. *Forensic Science International*, 108(2):81–95, February 2000.

[105] L. Verze. History of facial reconstruction. *Acta Biomed*, (80):5–12, 2009.

[106] Y. Wang, T. Adali, S.Y. Kung, and Z. Szabo. Quantification and segmentation of brain tissues from MR-images: A probabilistic neural network approach. *IP*, 7(8):1165–1181, August 1998.

[107] A. Watt. *3D Computer Graphics*. Addison Wesley, 3rd edition, 2000.

[108] P. Wen, X. Wu, T. Gao, and C. Wu. Kd-tree based ols in implicit surface reconstruction with radial basis function. In *ICAT*, pages 861–870, 2006.

[109] C. Wilkinson. *Forensic Facial Reconstruction*. Cambridge University Press, United Kingdom, 1st edition, 2004.

[110] C. Wilkinson. Review Facial reconstruction - anatomical art or artistic anatomy. *Journal of Anatomy*, (216):235–250, 2010.

[111] M.A. Wirth. *A nonrigid approach to medical image registration: matching images of the breast*. PhD thesis, RMIT University, Melbourne, Austrialia, June 1999.

[112] C. Xu and J. L. Prince. Snakes, shapes, and gradient vector flow. Technical report, The Johns Hopkins University, October 1996.

[113] C. Xu and J. L. Prince. Gradient Vector Flow: A New External Force for Snakes. *IEEE Proceedings Conference on Computer Vision and Pattern Recognition*, pages 66–71, 1997.

[114] C. Xu and J.L. Prince. *Handbook of Medical Imaging*. Academic Press, September 2000.